Measuring Spectrocopy of Andreev Bound States in One Dimensional Superconducting Nanowires

Master's Thesis

Written by

Magnus Rønne Lykkegaard

Supervised by

Prof. Charles M. Marcus

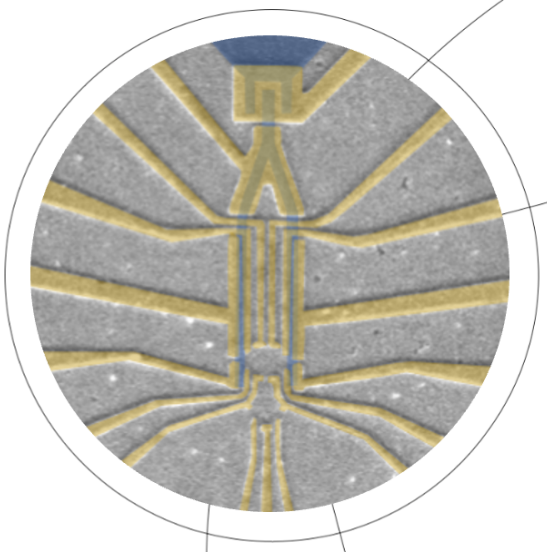

University of Copenhagen

UNIVERSITY OF
COPENHAGEN

Faculty:	Science	
Institute:	Niels Bohr Institute	
Authors:	Magnus Rønne Lykkegaard	KU-ID: CXW938
Title:	Measuring Spectrocopy of Andreev Bound States in One Dimensional Superconducting Nanowires	
Supervisor:	Prof. Charles M. Marcus	marcus@nbi.ku.dk
Handed in:	31st of October	
Defended:	WRITE THE DATE	

Abstract

Achieving quantum supremacy has the potential to drastically increase the speed at which we can solve problems, and opens the possibility of solving problems which are impossible to solve in classical computation. In this thesis, we measure a hybrid device, which is proposed to be able to achieve an effective 1D p-wave superconductor, hosting Majorana zero modes. These quasiparticles can be employed in the construction of topological quantum computers, though the realization of these zero energy modes has long been a challenge for experimental physicists, and one that has not been solved definitively yet.

This thesis is based on a device architecture proposed to measure the parity of Majorana zero modes in a parity-to-charge scheme, in which the inherent parity degeneracy is lifted by the introduction of a quantum dot, which couples the two parallel superconducting nanowires. The two lithographically defined nanowires, are connected to each other at one end, and through a semiconducting cavity in the other end. This forms a loop in which we can thread a magnetic flux.

We focus on the challenges of coupling two superconducting wires through a quantum dot. We discuss and show results of the regime of a spinful Josephson junction. We see evidence that the quasiparticles in the superconducting wires can screen the spinful Josephson junction, a phenomenon called an Andreev dot. A special emphasis is then put on the cotunneling regime. Here we show that we can couple a mesoscopic quantum dot to the Andreev bound states that two superconducting wires host, at low parallel magnetic fields ($B_{\parallel} < 1$ T). We demonstrate that we are fully able to control the trivial Andreev bound states using a magnetic field parallel to the superconducting nanowires and electrostatic gates. We show that the energy levels of the quantum dot can hybridize with the Andreev bound state energy levels, and also observe phase dependence in this regime indicating coherent transport of the electrons/quasiparticles through both arms of the loop. For future measurements, by the application of a larger magnetic field, can drive the system into its topological phase. It would be interesting to compare the hybridization effect of non trivial states in the superconducting nanowires, to that of the trivial case measured in this thesis.

Lastly, we introduce the concept of quantum chaos in an Andreev billiard geometry. We show preliminary experimental result where we can resolve the statistics of the level spacings in a chaotic billiard with particle-hole symmetry. This project is at the moment still in the start-up phase and the measurements are done in devices that are optimized for a parity-to-charge scheme. A comprehensive discussion on future considerations, will follow the presentation of the preliminary measurements

Acknowledgements

Working in the Topological 2DEG group of QDev at University of Copenhagen, has truly been one of the best academic choices I have made. I am grateful for introduction to this team by Charles M. Marcus, whose supervision during the project has guided me to be a better experimentalist. I cannot imagine having done this project without the day-to-day supervision of Felix Passmann, who is also responsible for teaching me to be an experimentalist in a modern quantum laboratory. In conjunction with this, working on the project together with Frederik Wolff Knudsen and Serwan Asaad have made the work of the project extremely enjoyable. It would be hard to measure anything without the brilliant Sangeeth Kallatt fabricating perfect devices time and time again. I am thankful, not just for this, but also our discussions on how to fabricate nanodevices and introducing me to the clean room laboratory with hands-on guidance. In general, I also wish to thank the entire TOPO2DEG research group. I've enjoyed the academic tutoring, discussions, journal clubs and group meeting that have enabled me to better understand the physics at play and convey myself in a proper academic tone. The camaraderie of the group truly is one of a kind and have made long days measuring in the lab felt like short one. For this I also extend my gratitude to the entirety of QDev, both the academic and administrative staff, that makes it possible for students like me, to effortlessly begin their journey working in a quantum laboratory. Personally, I have also enjoyed a great support and interest from friends and family which have worked to spur me on and for this support I am grateful.

Having started in the lab and started my work on my thesis during COVID restrictions, has been a struggle, but I could not imagine better place to overcome this hardship. Thank you.

Contents

CHAPTER 0

Outline

This thesis concerns spectroscopic measurements of a system designed to achieve a *parity-to-charge* readout of non-local fermionic states, called Majorana Zero Modes. We will evaluate the technique in which a quantum dot hybridizes with fermionic modes at zero energy in two superconducting nanowires. We will explain the interplay between spin and superconductivity that such a system hosts, and probe its dependence on the magnetic field applied and the superconducting phase difference between two coupled superconducting nanowires, seperated by a Josephson junction hosting a quantum dot. This thesis will present experimental result of such a system and compare them to theoretical results in literature. The interested reader should feel free to pursue the theoretical derivation using the references given throughout the text.

- **Chapter 1** discusses the theory of the materials we use. A breakdown of superconductivity, the spin-orbit interaction, Andreev reflections and quantum dots are outlined. Furthermore we will explain the concept of a topological superconductor, Majorana zero modes and the parity-to-charge scheme.

- **Chapter 2** is a rundown of techniques of material science used to achieve pristine heterostructures and fabricate nanodevices. The experimental methods used to measure these nanodevices in low temperature (~15mK) cryo-free dilution refrigerators are also explained.

- **Chapter 3** shows some of the experimental results that has been measured during the course of the work on this master thesis. It can be seperated into four subsections: tuning a nanodevice, spectroscopy of a quantum dot, the spectrocopy of superconducting subgap states using a quantum dot, and spectroscopy at zero perpendicular magnetic field vs a magnetic flux quantum away from true zero.

- **Chapter 4** is a discussion of the results found in the previous chapter, concluding remarks, and an outlook to the future of the experiment.

- **Chapter 5** is a digression to another experiment, that - though it is in its infancy - is an extremely interesting subject: Andreev Billiards. Here we discuss how the interplay between superconductivity and quantum chaos, form a new set of universality classes, decribing the ensemble statistics of chaotic systems with particle-hole symmetry.

CHAPTER 1

Introduction

Since the original proposal by Paul Benioff in 1980 [1], quantum computation has drawn a rising level of interest due to the computational power assosciated with it, not just from the academic world, but also from tech companies such as Google, IBM and Microsoft. As opposed to classical computation; which utilizes bits, that are *"on"* or *"off"* - symbolized by logical states $|1\rangle$ and $|0\rangle$ - in a transistor circuit, quantum computers are based on *quantum bits* (qubits): quantum states that can be superpositions of *on* and *off*, $c_0 |0\rangle + c_1 |1\rangle$, and more excitingly they can be in an entagled state with other qubits. Quantum computers (QCs) can be based on several quantum mechanical systems; be it spin qubits in semiconductors, superconducting qubits such as transmons, fluxons and cooper pair boxes, and trapped ion systems. The key similarity of these systems are that they at their essence host a two-level system that represent to be the logical states $|0\rangle$ and $|1\rangle$.

As in classical computers, errors also occur in quantum computers, but the severity in QCs are far more serious. Take, for example, a standard bit flip: In a classical computer, a 1 turns into a 0. This is readily fixed by having copies of the same original state, referred to as redundancy: Initializing identical bits, doing the desired computations, and then evaluating the output. If for example 1 of 5 copies are different, the computer can simply find that an error has happened as only 1 bit came out with a different result. This is not possible in QCs due to the no-cloning theorem[1] [2, 3]. In the text we will refer to quantum errors as the decoherence of the qubit, which is the loss of stored information of a quantum system. This thesis

[1] A theorem which was proven independently by W. Wooters and W. Zurek, and D. Dieks in 1982

will investigate systems that are proposed hosts of toplogical excitations that are the building blocks of topological quantum computers (TQCs). As opposed to other QC schemes TQC tackles the inherent problem of the decoherence of information, by the virtue of storing information non-locally, and quantuminformation is described as *fault-tolerant* [4]. In this scheme the act of measuring the topological charge is enough to achieve a TQC, which is exactly what our device architecture in Sec. 1.4, is built to achieve. The basics of a measurement based topological quantum computer (MBTQC) is described App. 1.1.3. Naturally, other QC also mitigate errors, through different error correction protocols, though the overhead on these are generally high compared to TQC.

1.1 Superconductors - Trivial and Topological

Superconductors (SCs) are arguably one of the most seminal discoveries in condensed matter physics (CMP) of the 20^{th} century. Some of the greatest physicists and mathematicians have tackled the problem of realizing and describing different superconductors, and several aspects of superconductivity are still unknown and their research ongoing. Two principles define a superconductor: The resistance of the material goes to zero as the temperature approaches zero and it expels magnetic flux via the Meissner effect. Starting with its discovery by H. K. Onnes in 1911 [5], the constitutive relations describing the penetration of magnetic fields in SCs by brothers H. and F. London in 1935 [6], led to the phenomenological description of superconductors characterised by the Ginzburg-Landau theory in 1950 [7]. These were in turn supported, as shown by L. Gor'kov in 1959 [8], by the microscopic Bardeen-Cooper-Schrieffer (BCS) theory derived in 1957 [9–11]. The first part of this theory section describes conventional superconductors in general, i.e. SCs that can be described by BCS theory.

1.1.1 The Theory of Superconductors

As a preview to topological superconductors (TS), a brief discussion on the physics of the superconducting properties of s-wave superconductivity is needed [12]. The microscopics of a conventional superconductor is described by three groundbreaking papers, published by Bardeen, Cooper and Schrieffer (BCS) in 1957 [9–11]. BCS

theory's core principle is to describe an attractive interaction between electrons. The attraction, they realized, was due to a retarded relaxation or equilibration of the lattice as electrons in a metal pass by lattice sites. That is, electrons that distort a crystal will have travelled far from the site before the crystal excitation has relaxed, however the distorted potential can still influence and attract another passing electron. To describe this they introduced the Hamiltonian, now known as the BCS Hamiltonian,

$$H_{BCS} = \sum_{k,\sigma} \epsilon_k \hat{c}^\dagger_{k\sigma} \hat{c}_{k\sigma} - \frac{u}{L^d} \sum_{k,k',q} \hat{c}^\dagger_{k+q\uparrow} \hat{c}^\dagger_{-k\downarrow} \hat{c}_{-k'+q\downarrow} \hat{c}_{k'\uparrow}. \tag{1.1.1}$$

The first term, with ϵ_k, described the kinetic energy of electrons with momentum k and spin σ. The second term is an electron-electron interaction with strength u, normalized with respect to the dimensions of the SC, L^d. The interaction describes the creation and annihilation of a Cooper pair, which is a bosonic excitation, formed, at least in conventional SCs, by pairs of electrons with opposite spin and momentum. The fermionic many-body annihilation and creation operators $\hat{c}_{k,\sigma}$ and $\hat{c}^\dagger_{k,\sigma}$ obey the commutation relation laid out in Fermi-Dirac statistics,

$$\{\hat{c}_{k,\sigma}, \hat{c}_{k',\sigma'}\} = \{\hat{c}^\dagger_{k,\sigma}, \hat{c}^\dagger_{k',\sigma'}\} = 0 \quad \{\hat{c}_{k,\sigma}, \hat{c}^\dagger_{k',\sigma'}\} = \delta_{k,k'}\delta_{\sigma,\sigma'}. \tag{1.1.2}$$

SCs that can be explained using this microscopic theory are denoted as a conventional SC. Decoupling the interaction in the Cooper channel with a bosonic-like field, Δ, the Bogoliubov-de Gennes (BdG) mean field Hamiltonian is derived. Using diagonalization, the Hamiltonian of the quasiparticles that describe excitations, γ defined via a Bogoliubov transformation, in a SC is given by,

$$H = \sum_k E_k(\gamma^\dagger_{\uparrow k}\gamma_{\uparrow k} + \gamma^\dagger_{\downarrow k}\gamma_{\downarrow k}) \quad , \quad E_k = \sqrt{\epsilon_k^2 + |\Delta|^2} \quad , \quad \gamma_{\sigma,k} = v c^\dagger_{-k,-\sigma} + u c_{k,\sigma}, \tag{1.1.3}$$

where ϵ_k is the original electron dispersion $\epsilon_{k,\pm} \propto k^2 - \mu$, and the electron-like and hole-like coefficients that squared sums to one, $|v|^2 + |u|^2 = 1$. Whether quasiparticles are more hole- or electron-like is dependent on the energy,

$$|u|^2 = \frac{1}{2}\left(1 + \frac{\sqrt{E^2 - \Delta^2}}{E}\right). \tag{1.1.4}$$

These above relations are plotted in Fig. 1.1. Here we can see that with no barrier, within the gap $E < \Delta$, all transport is mediated via AR. For a larger barrier we would see that there is a peak at $E = \Delta$, and AR is suppressed within the gap by the barrier

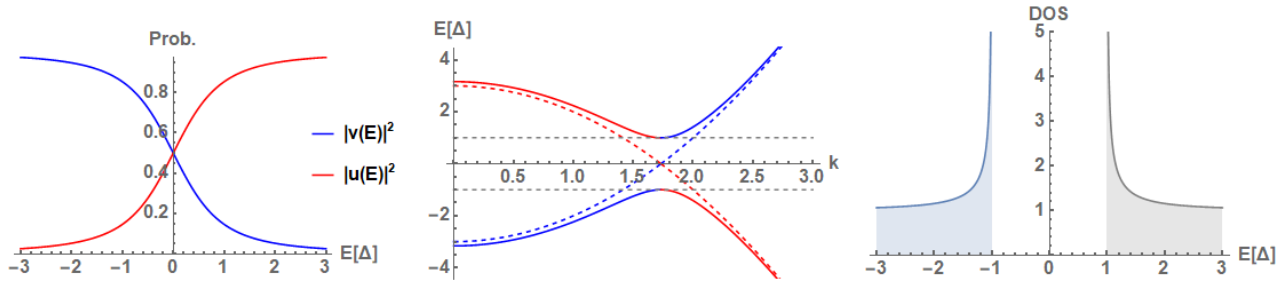

(a) *(b)* *(c)*

Figure 1.1: *Properties of a conventional superconductor's quasiparticles.* ***a)*** *the probabilities of having the quasiparticles be hole- or electron-like.* ***b)*** *The dispersion of a normal material (dashed) vs that of a superconductor (solid). Blue corresponds to particles and red corresponds to holes. The gray dashed lines marks* $\pm|\Delta|$*. Here the chemical potential is set to* $\mu = 3$ *which can be seen from the fact that crossing/avoided crossing is at the fermi wavevector,* $k_F = \sqrt{3}$*.* ***c)*** *The superconducting density of states of the Bogoliubov quasiparticles. At zero energy the Cooper pairs condense, and are protected by the superconducting gap,* Δ*. At* $E = \Delta$ *we see the superconducting gap which has a very characteristic van Hove singularity. All energies are in units of the superconducting gap* Δ*.*

strength, H. At temperatures below the critical temperature, T_C, the quasiparticles have an instability towards Bose condensation, $k_B T_C \lesssim \Delta$. This condensate is located at zero energy and consists of bosonic Cooper pairs. Two other critical parameters, that are important for most condensed matter experiments dealing with superconducting materials are; the critical magnetic field, B_C, the field at which the SC can no longer sustain the Meissner effect, and the critical current, I_C, which arises due to the fact that moving charges create a magnetic field, and this field can in turn reach the critical field value B_C.

1.1.2 Theory of Topological Superconductors

At present, a great deal of research interest is given to realizing a p-wave SC, since it was found by L. Fu and C. L. Kane [13] that hybrid devices employing conventional s-wave superconductors and topological insulators could host this new phase of matter. In this field, promising candidates for realizing the desired electron pairing are Bismuth Selenide topological insulators doped with either Copper, Strontium or Niobium (Cu_xBi_2Se, Sr_xBi_2Se and Nb_xBi_2Se [14]). However, as of now, no bulk

p-wave superconductor has been discovered. Compared to s-wave superconductors, which is a singlet pairing of electrons (That is, a spin-down electron is paired with a spin-up electron, and the total spin is $|\mathbf{S}| = 0$) the electron-electron pairing in p-wave SCs is mediated via a triplet pairing channel where the total spin of the Cooper pairs are $|\mathbf{S}| = 1$. Fermionic statistics dictates that the total wave function is anti-symmetric, and as such the symmetric spin part of the wave function, results in an anti-symmetric momentum, meaning that electrons pair-up with total non-zero momentum. The pairing symmetry of electrons is what yields the names s-wave, p-wave, etc. The pairing appears from the correlation function of the two paired up electrons $\Delta_{\sigma,\sigma'}(k) = \langle c_\sigma(k) c_{\sigma'}(-k)\rangle$. From this equation we can read of how the pairing of electrons behave. We can split the pairing field in its spin and momentum part, $\Delta_{\sigma,\sigma'}(k) = \delta(k)\psi_{\sigma,\sigma'}$ [15]. Due to the Pauli exclusion principle we know that $\Delta_{\sigma,\sigma'}(k) = -\Delta_{\sigma',\sigma}(-k)$

$$\begin{aligned} &\delta(k) = \delta(-k), \qquad \psi_{\sigma,\sigma'} \quad = -\psi_{\sigma',\sigma}, \qquad \text{Spin singlet pairing,} \\ &\delta(k) = -\delta(-k), \qquad \psi_{\sigma,\sigma'} \quad = \psi_{\sigma',\sigma}, \qquad \text{Spin triplet pairing,} \end{aligned} \tag{1.1.5}$$

where the anti-symmetry of the wave function (whether it resides in the momentum or spin space) is clearly seen. The p-wave SC is host to interesting features not observed in conventional SCs. This topological state of matter, hosts edge modes known as *Majorana Bound State* (MBS)[2], a fermionic zero energy mode which is protected by the *toplogical gap*. The emergence of these zero bias states (ZBSs) in one dimensional (1D) systems is most easily understood from the perspective of the Kitaev chain.

The Kitaev Toy Model, by A. Kitaev in 2001 is a proposal on how to visualize p-wave superconductivity in a spin polarized 1D wire [16, 17]. The model starts from a tight-binding (TB) model,

$$\mathcal{H}_{TB} = \sum_{i=0}^{L} -w(\hat{c}_i^\dagger \hat{c}_{i+1} + \hat{c}_{i+1}^\dagger \hat{c}_i) + \Delta_p \hat{c}_i \hat{c}_{i+1} + \Delta_p^* \hat{c}_i^\dagger \hat{c}_{i+1}^\dagger - \mu\left(\hat{c}_i \hat{c}_i^\dagger + \frac{1}{2}\right), \tag{1.1.6}$$

where the hopping term strength is w, the p-wave superconducting pairing potential is Δ_p, and the chemical potential of the system is μ. We can break up the electrons into the Majorana basis by explicitly writing the complex and real part of the fermionic

[2]Majorana Bound States and Majorana Zero Modes (MZM), is used interchangeably through literature.

creation/annihilation operators into separate Majorana operators,

$$\hat{c}_i = \frac{1}{2}(\gamma_{2i} + i\gamma_{2i-1}) \quad \hat{c}_i^\dagger = \frac{1}{2}(\gamma_{2i} - i\gamma_{2i-1}), \tag{1.1.7}$$

where γ_{2i} and γ_{2i-1} sits on the same fermionic lattice site. Rewriting Eq. 1.1.6 in the Majorana basis, we can examine to limiting cases.

1) $\Delta_p = w = 0$ **and** $\mu < 0$. This is the trivial regime, where we have removed superconductivity. Setting the hopping term to zero simply gives us a system where all Majorana operators pair up with the Majorana operator on its respective electron site,

$$\mathcal{H}_{M,1} = -\frac{\mu}{2}\sum_{i=0}^{2L}\gamma_{2i-1}\gamma_{2i}. \tag{1.1.8}$$

2) $\Delta_p = w > 0$ **and** $\mu = 0$. In this case, superconductivity has been turned on, and the strength of the hopping term is equal to the strength of the superconducting pairing term. Majorana operators will pair up with Majorana operators from neighbouring electron sites,

$$\mathcal{H}_{M,2} = -iw\sum_{i=1}^{2L-1}\gamma_{2i}\gamma_{2i+1}. \tag{1.1.9}$$

The difference between the two regimes are highly interesting and is illustrated in Fig 1.2. Changing back to the Dirac fermionic basis, we find that,

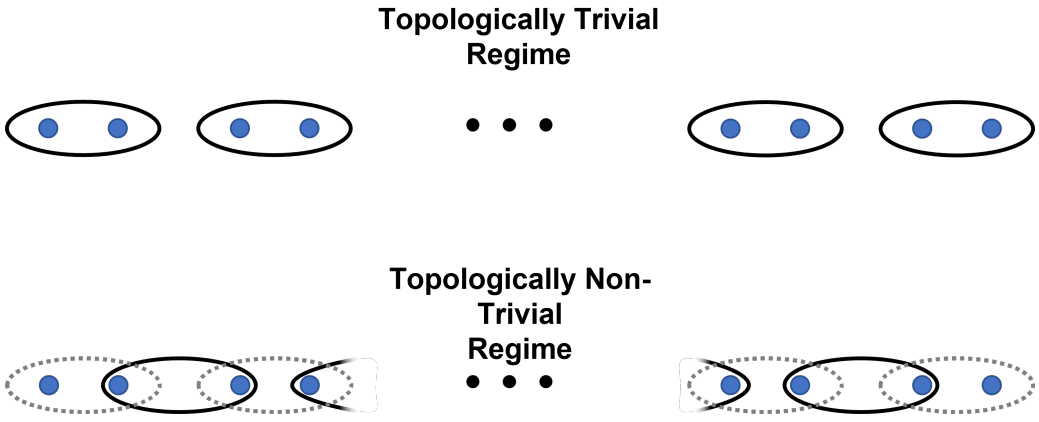

Figure 1.2: *The two regimes of a TSC nanowire. Circles indicate fermionic lattice sites and illustrates how Majoranas couple to each other, blue dots indicate Majorana lattice sites and doted lines of the bottom panel indicate the difference of Majorana fermions pairing in the trivial regime versus the non-trivial regime. We clearly see that there are unpaired Majoranas in the ends of the non-trivial regime.*

$$\mathcal{H}_{M,2} = 2w \sum_{i=1}^{L-1} \left(\hat{c}_i^\dagger \hat{c}_i + \frac{1}{2} \right). \tag{1.1.10}$$

Note that, as stated, Majoranas have paired with a neighbouring site Majoranas and therefore,

$$\hat{c}_i = \frac{1}{2}(\gamma_{2i} + i\gamma_{2i+1}) \quad \hat{c}_i^\dagger = \frac{1}{2}(\gamma_{2i} - i\gamma_{2i+1}). \tag{1.1.11}$$

The two Majoranas at either end of the chain pair up in a non-local state $\hat{c}_{MZM} = \frac{1}{2}(\gamma_1 + i\gamma_{2L})$. If we move back to the BdG Hamiltonian we would see that all of the fermionic lattice sites would pair up in Cooper pairs. One of the most interesting properties of this system is that the non-local state $\hat{c}_{MZM}$ does not have a partner, and for no additional energy cost we can occupy the state. In contrast to a trivial SC, which always have an even number of fermions at zero energy, the Cooper pair condensate, the TSC, can either have an even or odd number of fermions, dependent on the occupation of the non-local state $\hat{c}_{MZM}$. A small caveat is that the zero energy mode in small wires are lifted to a finite energy if there is a wave function overlap of (γ_1, γ_{2L}); this lifting is exponentially suppressed by the length, L, of the 1D wire $\sim \mathrm{e}^{-L/\xi}$, in proportion to the coherence length, ξ. The two states are related via the fermionic creation/annihilation operator $\hat{c}_{MZM} \left|\phi^{(e)}\right\rangle = \left|\phi^{(o)}\right\rangle$, and we find the occupation via the number operator, $\hat{n}_{MZM} = \hat{c}_{MZM}^\dagger \hat{c}_{MZM}$ the eigenvalue being 1 (0) for the odd (even) state. In literature we mostly describe this even-oddness with the parity operator,

$$\hat{P} = 1 - 2\hat{c}_{MZM}^\dagger \hat{c}_{MZM} = i\gamma_{2L}\gamma_1. \tag{1.1.12}$$

Which has eigenvalues $(1, -1)$. To find the spectrum of the system, Eq. 1.1.6 can be rewritten in k-space via a Fourier transform and diagonalized:

$$E(k) = \pm\sqrt{(2 \cdot w\cos(k) + \mu)^2 + 4|\Delta|^2 \sin^2(k)} \tag{1.1.13}$$

This more general equation where we also permit $\mu \neq 0$, shows a phase transition at,

$$\mu \geq -2w, \tag{1.1.14}$$

where the spectrum becomes gap-less at $k = \pm\pi$, which we attribute to a phase transition.

1.1.3 Majorana Zero Modes - Properties that Enable Topological Quantum Computation

A key feature of MBSs are the exchange statistics that describe them. As opposed to fermions (bosons), where exchange the of identical particles multiplies the total wave function by - (+), MBSs are non-abelian anyons. Anyons are quasiparticles, which can only exist in spatial dimensions $d \leq 2$, where exchange leaves the wave function with a complex phase. For non-abelian anyons the exchange is dependent on the order at which particles are exchanged [18].

$$\begin{aligned} \text{Bosons :} \quad & |\Phi(x_1, x_2)\rangle = |\Phi(x_2, x_1)\rangle \\ \text{Fermions :} \quad & |\Psi(x_1, x_2)\rangle = -|\Psi(x_2, x_1)\rangle \\ \text{Anyons :} \quad & |\Theta(x_1, x_2)\rangle = e^{i\varphi}|\Theta(x_2, x_1)\rangle \end{aligned} \tag{1.1.15}$$

where for non-abelian anyons the phase is a unitary operator, $\varphi \rightarrow \varphi\hat{U}$, that changes the state non-trivially based on the order of exchange of particles in the system. This additional symmetry of the wave function is rooted in the concept of the topology of the exchange of particles in 2+1D space-time and knot mathematics. The emergence of this new exchange symmetry readily follows from the fact that exchanging two particles two times has to return the same wave function. And while the world lines in 3+1D space time can be unknotted, in 2+1D this is generally not true. This is a reason why exchanging two particles once in $d > 2$ only has the symmetry (+) and (-). As such, even if an experimentalist knows everything about the spin, charge, position or energy, etc. of a non-abelian anyon, there is additional information encoded in the particles' space-time history. This information can be manipulated by moving particles around each other (a braiding operation) as can be seen in Fig. 1.3. This highly non-local information is intuitively well protected from small and local perturbation. For this thesis we will not digress further into the problem of braiding, but a excellent review on the topic is given in [18]. Two systems with four non-abelian anyons, that look identical at one points in space-time (the discs in Fig. 1.3), can constitute a two level system, from the fact that their space-time history is different. It is this non-local information, stored in the space-time history of the particles, that can be used in quantum computations [19]. The control of these quasiparticles, and as such the braiding operation, if they are realized in a material system, would most probably prove extremely difficult to control in real space, thereby hindering

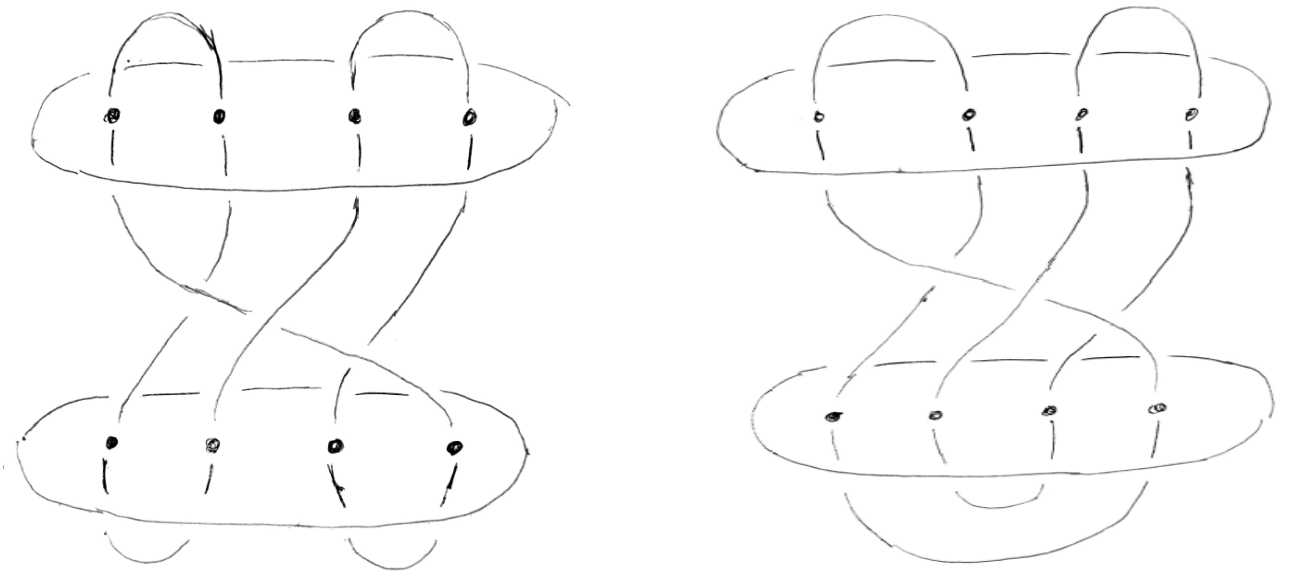

(a) ***(b)***

Figure 1.3: *The state* $|0\rangle$ *is created by the annihilation of two sets of two neighbouring Majorana particles to vacuum, while the state* $|1\rangle$ *is the annihilation of the two middle Majorana particles and the two Majorana particles furthest away from each other. Time passes vertically and the planes drawn are snapshots in time.* ***a)*** *This is the expectation value* $\langle 0|\,\mathrm{BRAID}\,|0\rangle$. *It is topologically equivalent to a circle.* ***b)*** *This is the expectation value* $\langle 0|\,\mathrm{BRAID}\,|1\rangle$. *It is topologically equivalent to two circles that are intertwined. Figures inspired by [18]*

braiding and as a result computation. This thesis instead takes hold in a scheme where the states are manipulated by using measurement based topological quantum computation [4, 20].

To circumvent the real-space braiding of non-abelian anyons in topological quantum computation, which was the original suggestion be A. Y. Kitaev in 1997 [74], an alternative propose emerged in 2008 [20], where the act of measuring the states, acts as an implementation of computational gates, this is known as a one-way computer (we collapse the wave function onto the parity as we measure, and as such destroy any previous information [4]). This is based on the already proposed scheme of achieving a quantum computer: measurement based quantum computer (MBQC). The act of measuring the topological charge is enough to achieve a QC. However, the measurement logic gates only form a Clifford set. For universal computation [4], an introduction of a non-Clifford gate has to be introduced. In the MBTQC, there exist no topologically protected non-Clifford gate.

1.2 Physics of Mesoscopic Structures

A proposed method to effectively achieve a p-wave superconductor in 1D nanowires is to combine the properties of a semiconductor with spin-orbit interaction to split the spin bands, a superconductor to introduce proximitized superconductivity, with particle-hole (PH) symmetry, and a magnetic field to open a helical gap at $|\mathbf{k}| = 0$ [21, 22]. In the following section, we'll explain the mechanisms that facilitate the spin-orbit interactions in semiconductors (SMs) and the transfer of superconductivity to the SM. We'll also touch upon a integral part of our specific experiment; *quantum dots*.

1.2.1 Spin-Orbit Coupling in Semiconductors

For the purpose of explaining spin-orbit (SO) coupling [23, Ch. 9.6, Ch. 3.3], we imagine a crystalline semiconductor, from the crystal structure follows a band structure with electrons occupying valance and conduction band. In heavy elements SO interaction arises. SO interaction is a relativistic effect when electrons travel in an electric field and experience a Lorentz force due to the electrostatic potential of the lattice moving, relative to the electron's rest frame. The magnetic dipole moment of the electron's spin is coupled to the effective magnetic field ($\mathrm{B_{eff}}$ or $\mathrm{B_{S-0}}$), which the electron experiences in its rest frame. $\mathrm{B_{eff}}$ originates from the potential, $V(\mathbf{r})$, inherent to the lattice of the crystal that the electron travels, with velocity $\mathbf{v}$, through the following relation,

$$\mathbf{E}(\mathbf{r}) = -\nabla(V(\mathbf{r})) \quad \Rightarrow \quad \mathrm{B_{eff}} = -\frac{1}{c^2}(\mathbf{v}\times\mathbf{E}). \tag{1.2.1}$$

The energy of the interaction is found via a Zeeman Hamiltonian of magnetic field, $\mathrm{B_{eff}}$. The direction of the electric field and therefore also the direction of the effective magnetic field the electron experiences is important: In 2D zinc-blende crystals the result is a *Dresselhaus* contribution, originating from the bulk inversion asymmetry, while the confinement of the two dimensional electron gas (2DEG), in a quantum well, can lead to the *Rashba* contribution, if the confinement has a structural inversion asymmetry [23, Ch .9.6]:

$$H_{S-O} = -\frac{g\mu_B}{2c^2}(\mathbf{v}\times\mathbf{E})\cdot\mathbf{S} \quad \overset{2D}{\Longrightarrow} \quad H_{S-O,2D} = \alpha_R(k_y\sigma_x - k_x\sigma_y) + \beta_D(k_x\sigma_x - k_y\sigma_y). \tag{1.2.2}$$

Here g is the Landé g-factor, α_R denotes the Rashba contribution, β_D denotes the Dresselhaus contribution, and μ_B is the Bohr magneton. For InAs quantum wells (QWs), that we investigate, the Rashba terms dominates. One can rewrite the factors of Eq. 1.2.2: $\alpha_R = \alpha \langle E_z \rangle$ and $\beta_D = \beta \langle k_z \rangle$ which is dependent on the material specific coefficient, α, β. In bulk InAs, these compares as: $\alpha = 117.1\text{eÅ}^2$ and $\beta = 27.18\text{eVÅ}^3$ [23, Ch. 9.3], as such the contribution due to Rashba spin orbit coupling dominates. The SO coupling results in the two spin degenerate bands splitting for crystal momenta $k \neq 0$ as depicted in Fig. 1.4.

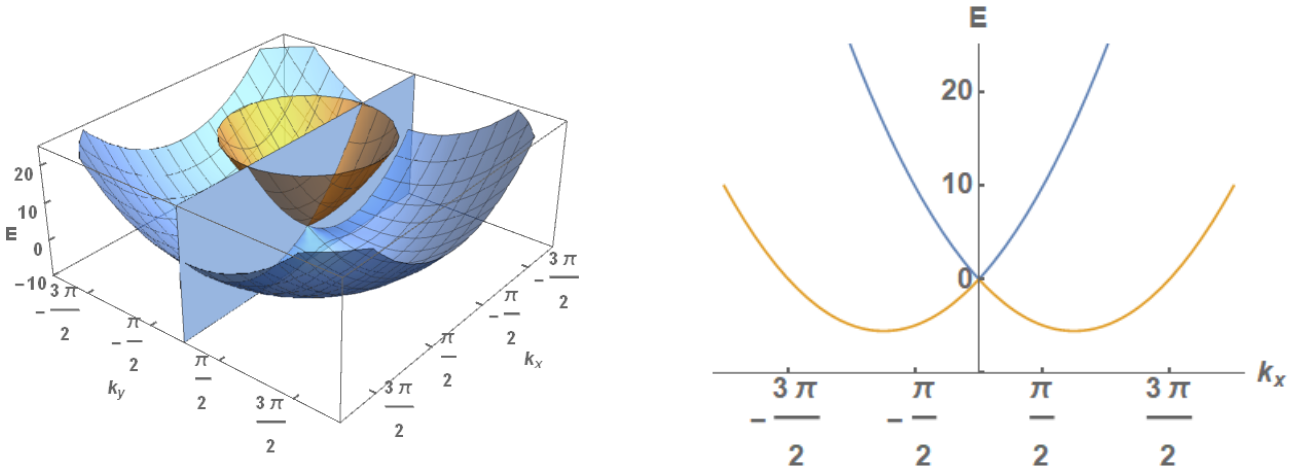

(a) *(b)*

Figure 1.4: *Band dispersion when Rashba S-O dominates.* ***a)*** *2D band dispersion of Rashba S-O, the plane indicates the line cut of b).* ***b)*** *Line cut for 1D systems. The energies are in arbitrary units, here we use* $\alpha_R = 4.3$. *The dispersion are calculated using the fact that Eq. 1.2.2 simplifies to* $E_\pm = \frac{\hbar^2 k_{||}^2}{2m^*} \pm \alpha_R k_{||}$, *with* $k_{||} = \sqrt{k_x^2 + k_y^2}$, *see [23, Ch. 9.6]. As such we can see that we can create spin split bands using crystals with Rashba SOI*

The Helical Gap: A physical realization in 1D nanowires (NWs), where Rashba SOI dominates, is that by applying a field perpendicular to the SOI effective B-field, we can create a helical liquid [24], where the transport of the wire has a spin texture; i.e. spin and velocity are correlated. 2D and 3D Majorana systems are proposed to exist in Topological Insulators[3] doped with superconductivity, as mentioned in Sec. 1.1.2. Opening a helical gap is *roughly speaking* the 1D correspondence of the three or two dimensional electron systems. The application of a magnetic field, perpendicular to the B_{SO}, in a nanowire, will open a helical gap at $k = 0$, which in turn mixes the spin

[3]Also named Quantum Spin Hall Insulators (as it's a precursor to Integer Quantum Hall Effect) in literature

up and spin down states. If the Fermi level is tuned within the helical gap spin up electrons travel right and spin down electrons travel left [24].

1.2.2 Superconducting Proximity Effect

To realize p-wave superconductivity, a requirement is that the electrons of the system coherently pair up as Cooper pairs. Conventional s-wave SCs can be utilized to achieve this. The transfer of the superconducting PH symmetry are facilitated by the superconducting proximity effect. By the virtue of having an electron gas close to a superconductor, we can achieve the desired coherence of the charge carriers in the SM. This effect was first observed in SC-normal metal-SC (SNS) junctions by R. Holm and W. Meissner in 1932 [25]. However, in a seminal paper from G. E. Blonder, M. Tinkham, and T. Klapwijk [26, 27] they explained the effect from the point of view of Andreev reflections (AR) on the interface between a normal metal and an SC.

Andreev reflections: An electron ($k\uparrow$) in a normal metal impinging on the boundary of a SC has no possibility of transmission into that SC, if the energy is less than the superconducting gap, $|E| < \Delta$, as there are no quasiparticle states available in this energy window. However, a second-order process can happen, where the SC accepts two electrons with opposite momentum and spin, and they transmit into the SC as a Cooper pair ($k\uparrow, -k\downarrow$), see Fig. 1.5c. Phenomenologically, the incident electron coherently pairs up with an opposite moving (opposite moving in the non-translational invariant direction) electron ($-k\downarrow$) and they are injected into the SC [28]. This leave a hole in the SM with ($k\uparrow$), and as the group velocity is found from the dispersion relation, $\mathbf{v} = \frac{1}{\hbar}\nabla_{\mathbf{k}} E_{\mathbf{k}}$, the hole traverses exactly the incident electrons path back, see Fig. 1.5a. In realistic heterojunctions the electron can also normal reflect, see Fig. 1.5b. This is because degradation of the interface (i.e disorder and fermi level mismatch) introduces a place where the electron can expend its momentum $k \rightarrow k'$, and as such $e^{ikx} \rightarrow e^{ik'x}$. As such a specular reflection (SR) can take place[4].

The BTK model is an intuitive model of the SC - SM interface that introduces an

[4]In most cases ARs are retro-reflective and the normal reflection is specular, due to the fact that hole's band curvature have the opposite sign of electrons. In graphene, holes and electrons have the same curvature. This means that graphene can exhibit specular AR [29]. This is a fascinating interplay between the quantum mechanics of superconductivity and the relativistic nature of electrons in Dirac cones. In contrast to retro-reflective AR that can be suppressed by strong SOI, specular AR are enhanced by strong SOI, under the correct conditions[30]

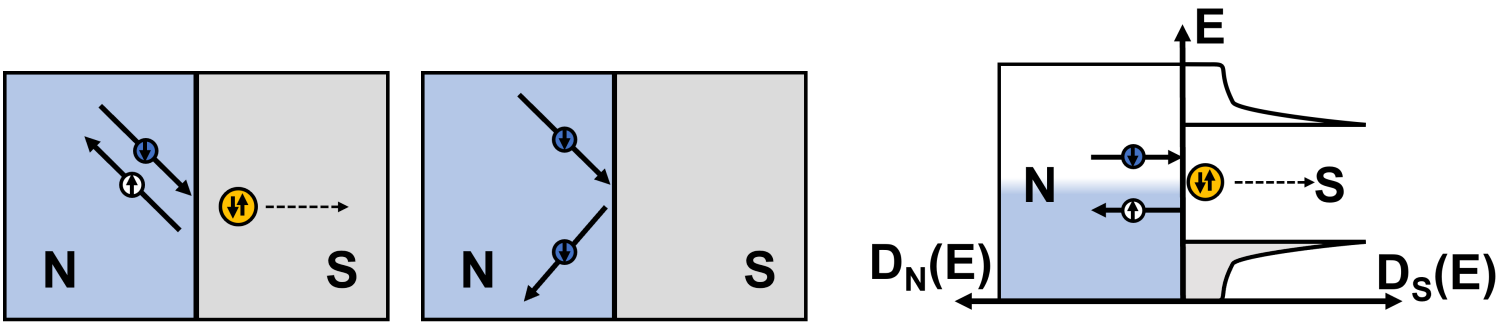

(a) *(b)* *(c)*

Figure 1.5: *The AR reflection process shown as opposed to SR.* ***a)*** *Andreev reflection: An electron retroreflects as a hole and a Cooper pair is injected into the SC.* ***b)*** *Specular reflection: An electron undergoes a specular reflection. No charge will flow into the SC.* ***c)*** *AR as seen in the DOS space. $D_S(E)$ and $D_N(E)$ are the DOS of a SC and the normal metal respectively. A hole is left with opposite momentum in D_N.*

interface parameter, into the calculation. The interface is modelled as a repulsive delta barrier, $H\delta(x)$, and this potential barrier is used in the BdG equations. The BTK model also uses the fact that the potential of the normal region[5] and the pairing potential are step-like, $U(x) = V(x)\Theta(-x) + H\delta(x)$ and $\Delta(x) = \Delta\Theta(x)$. We will return to comment on this approximation after laying out the BTK model. The wave function of an electron impinging/reflecting/transmitting in an NS junction can be written as,

$$\begin{aligned}
\psi_{\text{inc}} &= \begin{pmatrix} 1 \\ 0 \end{pmatrix} \mathrm{e}^{\mathrm{ik_e x}}, \\
\psi_{\text{r}} &= a \begin{pmatrix} 0 \\ 1 \end{pmatrix} \mathrm{e}^{\mathrm{ik_h x}} + \mathrm{b} \begin{pmatrix} 1 \\ 0 \end{pmatrix} \mathrm{e}^{-\mathrm{ik_e x}}, \\
\psi_{\text{t}} &= c \begin{pmatrix} u_0 \\ v_0 \end{pmatrix} \mathrm{e}^{\mathrm{iq_e x}} + \mathrm{d} \begin{pmatrix} v_0 \\ u_0 \end{pmatrix} \mathrm{e}^{-\mathrm{iq_h x}}.
\end{aligned} \tag{1.2.3}$$

The coefficients of the wave functions can be solved using the Schrödinger equation and appropriate boundary conditions. For different barrier parameters, Z, the results are seen in Fig. 1.6.

The BTK model can also be derived using a Green's formalism [31, Ch. 1]. This is

[5]Due to the fermi velocity mismatch between metals and SMs (due to the very different carrier densities) the potential $V(x)\Theta(-x)$ is always step-like.

	A	B
Normal state	0	$\frac{Z^2}{1+Z^2}$
General form		
$E<\Delta$	$\frac{\Delta^2}{E^2+(\Delta^2-E^2)(1+2Z^2)^2}$	$1-A$
$E>\Delta$	$\frac{u_0^2 v_0^2}{\gamma^2}$	$\frac{(u_0^2-v_0^2)^2 Z^2(1+Z^2)}{\gamma^2}$
No barrier ($Z=0$)		
$E<\Delta$	1	0
$E>\Delta$	v_0^2/u_0^2	0
Strong barrier [$Z^2(u^2-v^2)>>1$]		
$E<\Delta$	$\frac{\Delta^2}{4Z^2(\Delta^2-E^2)}$	$1-A$
$E>\Delta$	$\frac{u_0^2 v_0^2}{Z^4(u_0^2-v_0^2)^2}$	$1-\frac{1}{Z^2(u_0^2-v_0^2)}$

Figure 1.6: *Coefficients for the two different scattering events specular ($B = b \cdot b^*$) or Andreev ($A = a \cdot a^*$). The figure is the result of extensive calculations in [26]. For brevity [26] has used $\gamma = [u_0^2 + Z^2(u_0^2 - v_0^2)]^2$, $u_0^2 = 1 - v_0^2$ is Bogoliubov quasiparticles coefficients defined in Eq. 1.1.4, and $Z = H/(\hbar k_F)$ is the barrier.*

a more theoretically rigorous treatment of the system and considers the degradation at the interface. A direct result of the Green's formalism is a description of the single particle spectrum, the pairing potential, and the coherence in real space. The result predicts that the phase coherence from the superconductor leaks into the normal conductor, and the Cooper pair density decreases monotonically in a distance away from the interface. Vice versa, the model also predicts that the Cooper pair density decreases moving closer to the interface from the SC side. This introduces a correction to the step-like behavior in the BTK model.

Andreev Bound States: To this extent, we did not include the phase of the superconductor in the description of AR. When there is one SC in play, this does not matter. However, as we will see later in Sec. 1.4, the device measured in this work has two channels into the SC, which are seperated by a semiconducting region, and the SC is loop shaped. The phase of the SC in each channel, is dependent on the flux threaded through the loop, and as such the phase of the SC becomes an important parameter.

We can write the pairing potential as $\Delta = |\Delta|e^{i\phi}$, where ϕ is the phase of the SC. If electrons coherently retro-reflect on each of the SCs we can view it as pictured in Fig. 1.7a. As discussed in [32], the phase dependent energy of the Andreev bound states (ABS), $E_{ABS}(\phi)$, is found by keeping track of the phase accumulated in the cycle of an electron undergoing AR at one SC surface, traversing a semiconducting region as hole, undergoing another AR, and traversing the semiconducting region to its initial position. The phase acquired by the hole/electron travelling in a semiconducting cavity of length L is,

$$\phi_h = -k_h L \quad , \quad \phi_e = k_e L. \tag{1.2.4}$$

Additionally there is the phase associated with an Andreev reflection on a SC with phase ϕ_S,

$$\phi_{AR,e} = -\arccos\left(\frac{E}{\Delta}\right) + \phi_S \quad , \quad \phi_{AR,h} = -\arccos\left(\frac{E}{\Delta}\right) - \phi_S, \tag{1.2.5}$$

where e and h denote the outgoing particle from the AR. The momentum difference between hole and electron are readily given as $\delta k_{e,h} = E/(\hbar v_F)$, where v_F is the Fermi velocity, owing to the fact that they have exactly opposite energy. The total phase acquired is then,

$$\phi_{tot} = \phi_{1,2} - 2\frac{E \cdot L}{\hbar v_F} - 2\arccos\left(\frac{E}{\Delta}\right), \tag{1.2.6}$$

where $\phi_{1,2}$ is the phase difference of the SCs. Bound states require that $\phi_{tot} = 2\pi n$. Using a modified superconducting coherence length of the junction $\xi_J = \hbar v_F/(\pi\Delta)$ in the cavity (this is the short junction limit) [32], we find that

$$E(\phi_{1,2}) = \pm\Delta\sqrt{1 - \tau\sin^2(\phi_{1,2}/2)}, \tag{1.2.7}$$

Where τ is the transmission of both barrier (taken to be symmetric) coefficient of the barrier between N and SC. The spectrum is plotted in Fig. 1.7c. What is apparent in this spectrum, is that the introduction of an imperfect barrier $\tau < 1$, opens an avoided crossing at $E = 0$

1.2.3 Quantum Dots

In many branches of solid state physics the Coulomb interaction between electrons is either ignored or only play a perturbative role. This crude, but generally good,

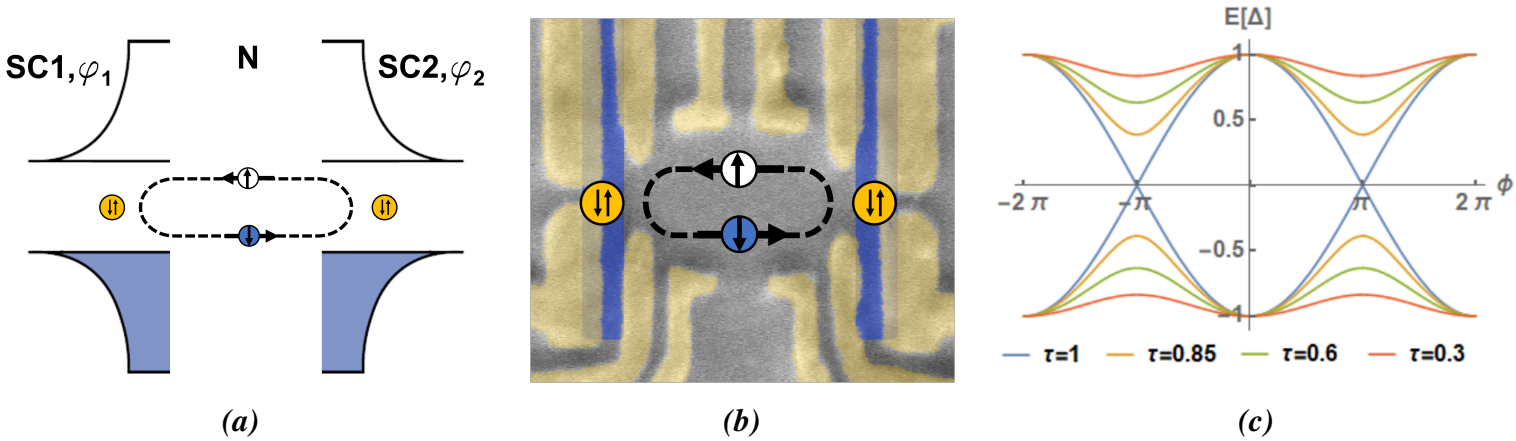

(a) *(b)* *(c)*

Figure 1.7: *Andreev bound states:* ***a)*** *Sketch of Andreev bound states, where two SCs couple via an ABS through a normal conducting region.* ***b)*** *False colour SEM shows the Andreev bound state in the QD cavity of our device. Gates are coloured golden, SM is coloured grey and the SC wires (which are connected to form a loop) are coloured blue.* ***c)*** *Andreev bound state energy spectrum as a function of phase difference between SCs. Energy is in units of the SC gap* Δ

approximation, and is deeply grounded in the Fermi liquid theory, which explains why interacting fermions in normal metals behave like an ideal Fermi gas at low temperatures[6]. Quantum dots are one phenomenon where this description fails. Laterally confined quantum dots (QDs), in 2DEG semiconductor physics, can be created by electrostatically gating the 2DEG[7] to confine the electron density in small patches, as illustrated in Fig. 1.8b. QDs have several interesting properties: The Coulomb Blockade (CB) transport phenomena (Fig. 1.9), that they are in general decoupled from the environment, and that their quantum mechanical level spacing - due to the particle-in-a-box-like nature of a QD - is observable.

Coulomb Blockade phenomena: A qualitative description of the CB phenomena is best obtained using a model as pictured in Fig. 1.8a and laid out in detail in [23, Ch. 18]. We describe the system using two normal leads, which are separated from the quantum dot via a tunnelling barrier. We can apply a source-drain bias V_{SD}, so that the two reservoirs are out of equilibrium, and we can change the potential on the

[6]Lev Landua proposed the idea of quasiparticles, a key principle in modern day physics, and correctly suggested that at low temperatures electrons become "dressed", which can alter e.g. their effective mass.

[7]In bottom-up produced nanowires QDs can be made much smaller than in 2DEGs, due to the fact that NWs already are small in the radial direction. Confinement can then be achieved either by changing the crystal structure, alternating i.e. between a cubic zinc-blende material and hexagonal wurtzite material, to create physical barrier, or a gate, e.g. by using a shadow evaporation technique if for example superconductivity has to be introduced.

QD, using a nearby gate V_{pg}. The QD is described by an occupational energy, the number, N, of electrons on the QD. To explain the Coulomb oscillations/resonances, in Fig. 1.9a, we can set $V_{\text{SD}} = 0$ (or $eV_{\text{SD}} \equiv E_F$). As the tunnel barriers to the leads are significant (the wave function is only located within the QD cavity), electrons cannot traverse the QD as is, as there are no available states. However, if we change the chemical potential of the dot, (dubbed *plunge the dot*), V_{pg}, we can change the energy of the occupational levels. If we apply a more positive voltage E_{N+1} can drop to E_F, and an electron can fill the state. This is CB transport; only at specific value of V_{pg} will current be able to traverse the QD, as seen in Fig. 1.9a.

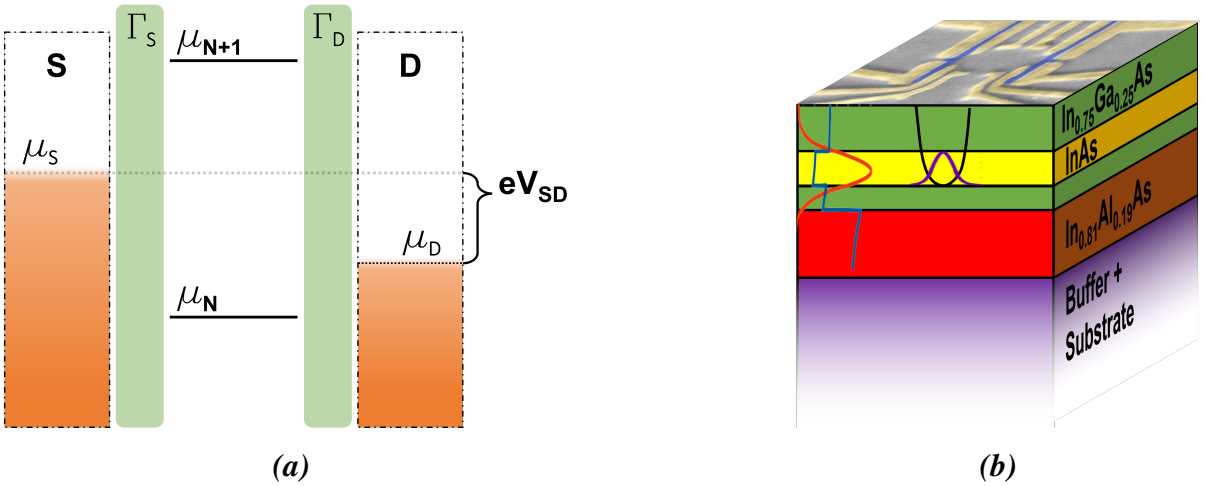

Figure 1.8: *The QD phenomena:* ***a)*** *The QDs occupational levels in relation to the source and drain leads (in this with N-leads). Here is drawn the blockaded regime, where no transport occurs.* ***b)*** *The wave function in the 2DEG can, via the gates drawn in gold on top, be confined to constitute a QD. The blue line is the band edge, and the red shows the vertical 2DEG density distribution. If we apply a negative voltage to the gates of the system (coloured gold on top), we can create a potential, black parabola, and laterally define a QD wave function, pictured by the purple line.*

This terminology can be used in the exact same way to describe the emergence of Coulomb diamonds in tunnelling spectroscopy (see Fig. 1.9b). For this description we should employ *charging energy* and the *lever arm*. In this situation, we allow for the tunning of the chemical potential difference of the reservoirs, as illustrated in Fig. 1.8a. The chemical potential of the quantum dot is given by the voltage applied to the plunger of the dot

$$\mu_N(V_{pg}) = \mu_N(V_{pg,0}) - e\alpha_{pg}\Delta V_{pg} \tag{1.2.8}$$

Charge can flow by plunging the dot within the window $\mu_S \geq \mu_N \geq \mu_D$. What follows from this is that when $\mu_S = \mu_N$ and $\mu_D = \mu_{N+1}$, we have that $eV_{SD} = \mu_N - \mu_{N+1}$, which is the *charging energy*, E_C, of the dot: The energy required to go from the energy level of $|N\rangle$ to $|N+1\rangle$.

This model only describes a Coulomb diamond where the tilt of the edges are identical. In Fig. 1.9b the edges clearly have asymmetric tilts. To describe this we would have to introduce a capacitive model. In this, the reservoirs are also capacitively coupled to the QD. As such when applying a bias, V_{SD}, it will plunger the dot. The two reservoirs can have different capacitive coupling which introduces the asymmetric tilt, $\alpha_S(\Gamma_S) \neq \alpha_D(\Gamma_D)$.

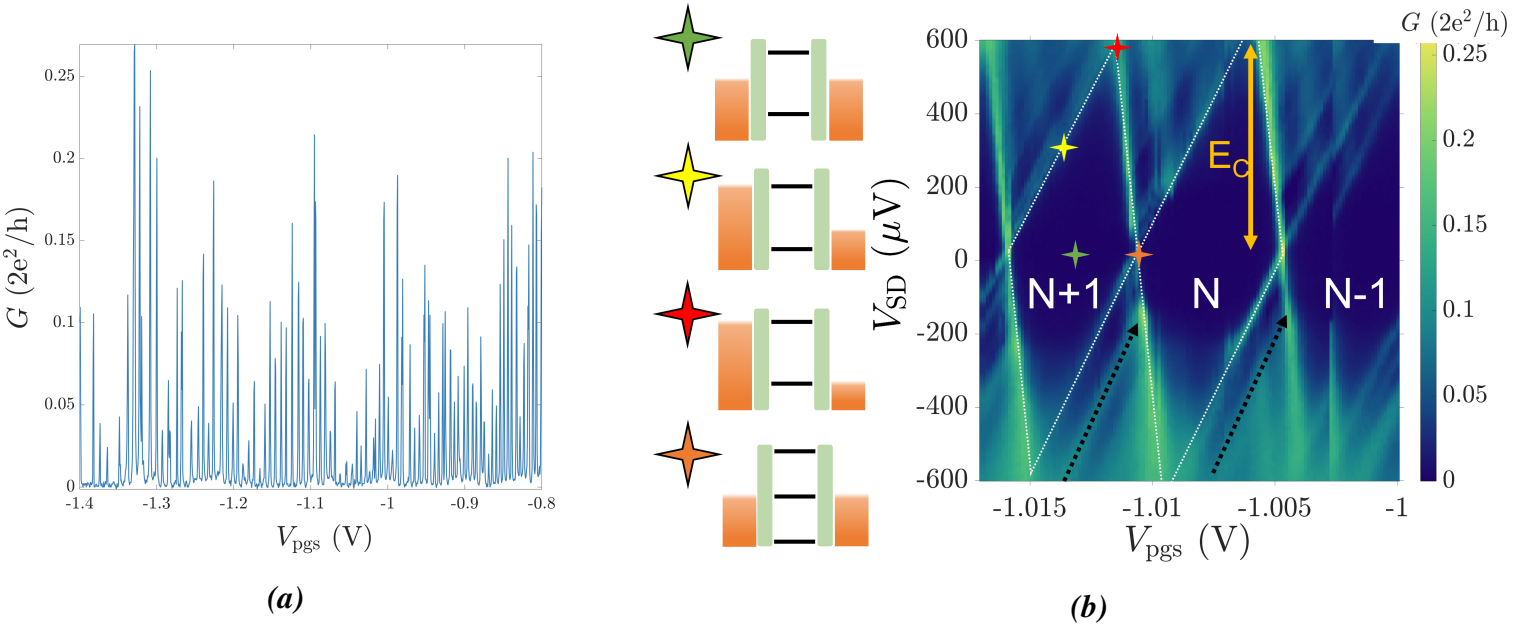

Figure 1.9: *Coulomb resonances and Coulomb Blockade:* ***a)*** *Shows Coulomb blockade resonances as we sweep the plunger gates of the QD. Applying zero bias voltage, the two reservoirs are in resonance and only by bringing the QD in resonance do the system allow for transport.* ***b)*** *If we also apply a bias voltage, we observe so-called Coulomb diamonds where bringing the QD in resonance with either source (S) or drain (D) allows for transport a transport channel across the system. The coloured stars indicate four different regimes in which we bring the QD's chemical potential in and out of resonance with the S/D lead. Black lines indicate some of the excited states visible in spectroscopy*

1.3 The Lutchyn-Oreg Hamiltonian

By combining properties of an s-wave superconductor and a semiconductor in a hybrid-device geometry, R. Lutchyn, J. Sau, and S. Das Sarma [21] and subsequently Y. Oreg, G. Refael, and F. von Oppen [22] showed in 2010 that it is possible to effectively achieve 1D p-wave superconductivity; via the Oreg-Lutchyn model, a SM wire with Rashba spin-orbit coupling to an s-wave SC via the superconducting proximity effect, of the form:

$$\mathcal{H}_{BdG} = \underbrace{\left(\frac{\hat{p}_x}{2m} - \mu\right)\sigma_0 \otimes \tau_z}_{\text{Kinetic}} + \underbrace{\frac{\alpha_R}{\hbar}\hat{p}_x\sigma_y \otimes \tau_z}_{\text{Rashba SO}} + \underbrace{g\mu_B B_x \sigma_z \otimes \tau_0}_{\text{Zeeman}} + \underbrace{\Delta\sigma_0 \otimes \tau_x}_{\text{s-wave}} \equiv H_{O-L}, \tag{1.3.1}$$

where σ_i and τ_i refers respectively to the spin space and particle-hole space. It yields the spectrum,

$$E_\pm^2 = E_z^2 + \epsilon_p^2 + \Delta^2 + \left(\frac{\alpha_R p}{\hbar}\right)^2 \pm 2\sqrt{(E_z\Delta)^2 + (E_z\epsilon_p)^2 + \left(\frac{\alpha_R p}{\hbar}\epsilon_p\right)^2}, \tag{1.3.2}$$

where ϵ_p is the kinetic energy of the system from Sec 1.1.1 and adopting $p_x \to p$ (the direction parallel to the nanowire), as it is the only momentum, and E_z is the Zeeman energy $E_z = g\mu_B B_x$. The system undergoes a phase transition at,

$$E_{Z,c} = \sqrt{\mu^2 + \Delta^2} \tag{1.3.3}$$

Because of this condition it is important that the system is driven topological before the superconducting phase is broken at B_c, and therefore materials with an optimal Landé g-factor have to be selected for experiments hoping to measure the TSC phase.

Introducing disorder, Sec. 2.1.3, into the system, can have a dramatic effect, depending on the origin of the disorder (See especially Fig. 1 of [33]). This can be seen in Fig. 1.10, where the smooth phase boundary of a clean system becomes asymmetric and jagged by the introduction of strong disorder [34] in a short wire. It is worth noting that many types of disorder do not destroy the topological MZM phenomena, if such a regime can be reached, but disorder can produce trivial zero energy modes which can be observed in both local measurements, and by coincidence also appear in non-local measurements [33].

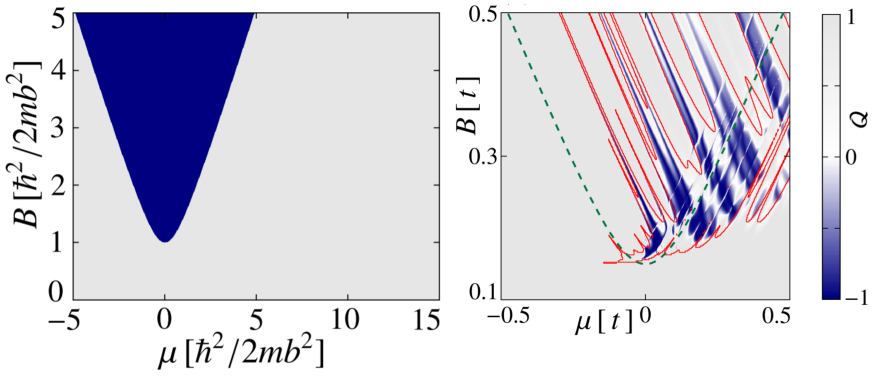

Figure 1.10: *The Phase diagram in μ and E_z phase space of a s-wave proximity coupled Rashba nanowire.* ***Left graph:*** *Analytical calculation of the phase diagram in a clean system with p-wave superconductivity.* ***Right graph:*** *An example of the introduction of disorder to the Rashba nanowire system in a short wire limit. This is a TB model, with hopping strength t. The green dashed line is the clean system's phase boundary, and the red line is the phase boundary in a disordered system. Figures adapted from [34], where the "measure" of topology is a topological charge, Q, which is explained in detail in [34].*

1.4 Parity-to-Charge conversion - The Loop-Qubit

The motivation of the experiment is to perform parity readout of a pair of MZMs. Several options to observe and verify MZMs has been proposed in the last decade. In the LoopQubit experiment, see Fig. 1.11, which is the device we have measured, this is achieved via the *charge-to-parity* scheme [4, 35, 36]. In this work we operate at much lower field (<1T) and do not expect to find MZMs, instead we will see we can coalesce an ABS to a zero-energy state. However, in the same way as there exists topological fermionic parities, trivial fermionic parities is also highly relevant to study, and the theory on the subject is scarce [37]. For now, we will turn to the topological case.

The two parities, $\hat{P}\left|\phi^{e(o)}\right\rangle = (-)1$, of an MZM is generically degenerate, as it does not enter in the Hamiltonian of Eq. 1.1.10, and so we would presume an experimental signature of distinguishing the two would be hard to detect. We can change this by

[8]By ensuring that there is no path to ground except through tunnel barriers, we *float* the wire. The wire can then be thought to be a mesoscopic island, the same way a QD is. In Fig. 1.11b this is done by applying a negative voltage to the top electrostatic gate - electrostatics gates are discussed in Sec. 2.1.2

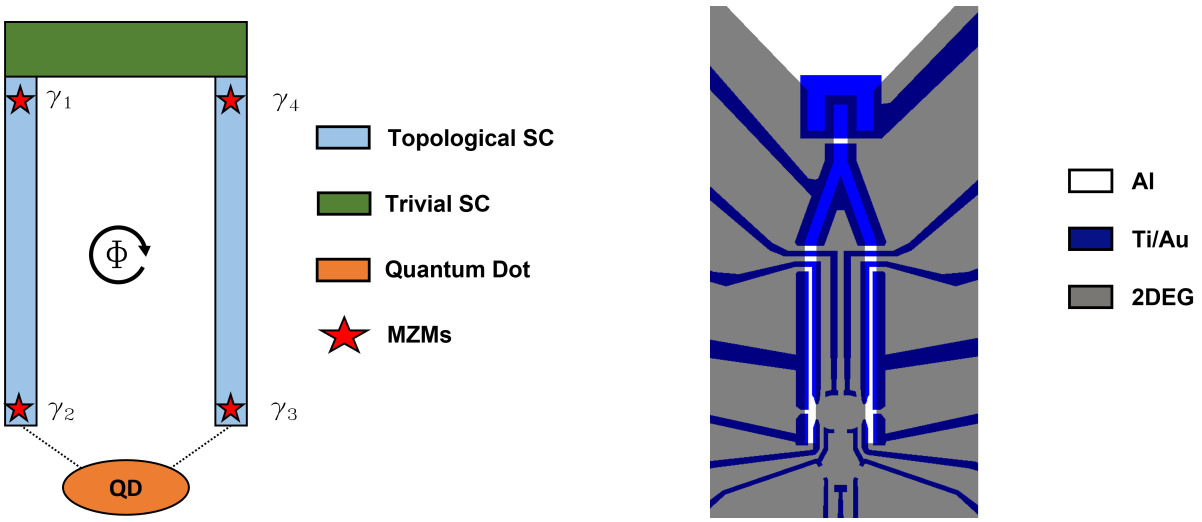

Figure 1.11: *This figures shows the basic schematics constituting the LoopQubit experiment [38]:* ***a)*** *The system is described hosting 4 MZMs where the ends couple to the QD. The coupling is tunable, as is the phase difference of the two SC wires.* ***b)*** *To achieve this scheme, the system needs to be heavily gated, seen in blue. The tuning fork design is introduced. If we designed the trivial backbone as in a) the trivial SC would go normal, long before the wires went topological, thereby introducing QPP.*

adding an additional physical mechanism: *charging energy*. As discussed in Sec. 1.2.3, by *floating*[8] the wire, we effectively fix the charge of the system, for a given electrostatic potential. Literature refers to such a system as a *Cooper pair box* [4]. As in the case of a QD, the energy required to change the charge is given by the charging energy. In this system, adding or subtracting electrons (by filling or emptying the zero mode) has an associated energy cost which splits the degeneracy. Note that as we fill an electron into an already filled zero mode, the two quasiparticles can pair up and enter the condensate, and effectively we have a empty fermionic state available. A side note is that if there is no fermionic inter-gap states available, and $\Delta > E_c$, we can only inject an even number of electrons into the superconductor. J. Shen et al describes the regimes and the transitions between an even and odd phase [39] at zero energy, as a indication whether an topological zero mode has been achieved. Another way to add charging energy to the system is via dot hybridization[9]. Let's first consider the case of a grounded SC described by the Oreg-Lutchyn Hamiltonian

[9]Note that the LoopQubit of Fig. 1.11b can achieve both regimes, by either not forming a dot or by not energizing its FET gate

Eq. 1.3.1. We model the interaction with a quantum dot with a Hamiltonian [4, 40],

$$\begin{aligned} H_{tot} &= H_{O-L} + H_{QD} + H_{tun.} \\ H_{QD} &= \epsilon d^\dagger d + E_c (d^\dagger d + n_g)^2 \\ H_{tun.} &= -i\frac{e^{-i\phi/2}}{2}(t_2 d^\dagger \gamma_2 + t_3 d^\dagger \gamma_3) + h.c. \end{aligned} \tag{1.4.1}$$

where ϵ is the energy level of the QD, E_c is the charging energy of the QD, t_1, t_2 are the coupling between zero modes and QD, and ϕ is the phase difference of the two SC wires. To emphasize that electrons inhabit the QD, electron creation (annihilation) operators are denoted with a "d"; $c^{(\dagger)} \rightarrow d^{(\dagger)}$. The spectrum of this Hamiltonian is,

$$E = -\frac{\varepsilon}{2} \pm \sqrt{\left(\frac{\varepsilon}{2}\right)^2 + t_2^2 + t_3^2 + 2p_{2,3}|t_3 t_2| \sin(\phi/2)} \tag{1.4.2}$$

where ε is the detuning of the quantum dot. We can then calculate the occupation/charge on the quantum dot (ignoring the offset charge), as it hybridizes with the ground state of the system.

$$\begin{aligned} q_d &= e(n_g - \langle \phi_{GS}| \, d^\dagger d \, |\phi_{GS}\rangle) \\ \langle \phi_{GS}| \, d^\dagger d \, |\phi_{GS}\rangle &= \frac{1}{2E_c} \langle \phi_{GS}| \, \frac{\partial H}{\partial n_g} \, |\phi_{GS}\rangle \\ q_d &= e\left(n_g - \frac{1}{2E_c}\frac{\partial E_{GS}}{\partial n_g}\right) \end{aligned} \tag{1.4.3}$$

Here we use the Feynman-Hellmann theorem. Here we see that the charge of the quantum dot is dependent on the ground-state energy, which in turn is parity dependent. For read-out techniques, observing this parity dependent energy splitting is not something we can do with a simple spectroscopic method. A key principle of spectroscopy is the transfer of charge onto and off of the device we measure. As mentioned, if charge tunnels onto the device we can fill sup-gap states (e.g. the MZM) which in turn changes the parity of the system, and therefore, an eventual qubit would lose its information. Charge events that fills the states in the sup-gap spectrum are called *quasiparticle poisoning* (QPP). Instead one should use another system, in our case a sensor dot (SD), to detect charge of the dot; this is refereed to as *charge sensing*. The charge of the hybridized QD, can capacitively affect a charge sensor (e.g. a single electron transistor (SET) or a QPC) as illustrated in Fig. 1.12.

QPP can be seperated into two contributions: Internal and external QPP. Internal QPP refers to the QPs at higher energies filling the groundstates of the system. The

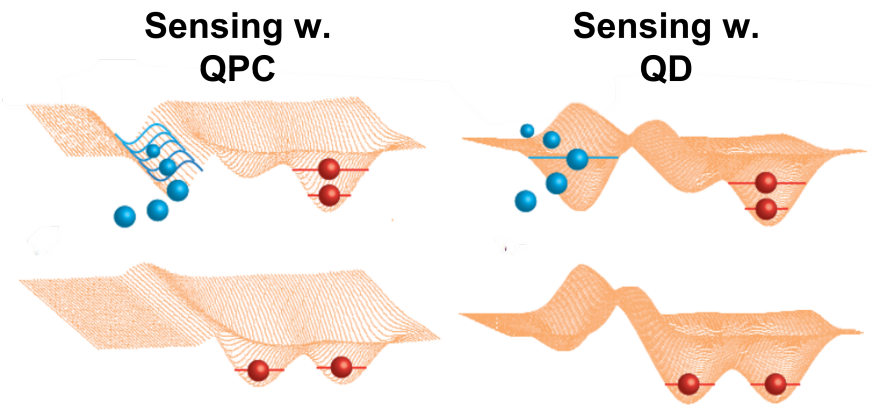

Figure 1.12: *Potential landscape in charge sensing schemes, which is highly dependent on the charge configuration, in this case a double dot:* ***Left picture:*** *Depending on the charge distribution of the capacitively coupled dot (here in red is shown a double dot here) the QPC (shown in blue) can either conduct or not.* ***Right picture:*** *Depending of the charge distribution of the capacitively coupled system the sensor QD (shown in blue) is on resonance or not. Figures from ref. [41].*

ideal way to combat this kind of poisoning is to ensure that the SC is hard gapped, that is zero density of states within the gap, with no subgap states, other than the states probed in the experiment. Discrete subgap states can normally be driven away from the gap and into the BCS continuum by applying a gate potential to the wire. However, experimentally it is difficult to ensure a hard gap SC at higher magnetic fields. A simple way to lessen external QPP is by adding a finite charging energy to the SC island. If we instead consider a floating SC loop, as in a Majorana Box Qubit experiment [42] or [4], we also need to consider the charging energy of the SC as well as that of the QD. This inturn modifies the spectrum of Eq. 1.4.2, though the groundstate is still parity-dependent.

ABSs vs MZMs: The scope of this thesis will not be to show charge fluctuating between a dot and a NW with MZM at the ends using a sensor dot. Instead, we have focused on achieving a cotunneling scheme in a system with controllable ABSs in the wires, as a precursor to these more advanced experiments. In SM/SC heterostructures, an important notion to bare in mind is that, MZMs originate from trivial ABS; experimentally it has been shown, that by applying the parallel magnetic field, ABSs coalesce to zero bias states that are proposed to be MZMs [43, 44]. The nature of trivial ABS zero bias states are therefore highly interesting to probe in our system, before turning our attention to the more exotic topological case, where the

zero energy states are MBSs.

CHAPTER 2

Methods

2.1 Nanofabrication

The theoretical discussions outlined in Chap. 1 has parameters highly dependent on the material used. A great deal of effort and research is therefore put into to making pristine heterostructures and selecting proper materials used to fabricate devices such as the LoopQubit mentioned in Sec. 1.4.

2.1.1 Molecular Beam Epitaxy Growth

In the lab of Topological 2DEG (TOPO2DEG) at the center of Quantum Devices, much of the *raw* materials are created out-of-house in the Microsoft Quantum Group in the Manfra lab at Purdue University. The stack of heterostructures that we use, is referred to as a *wafer stack*, which is grown bottom-up using a Molecular Beam Epitaxy system (MBE). The MBE has an atomic layer resolution; it is able to deposit monolayers of alloys or pure elements, the resulting schematic of the wafer on which we measure is seen in Fig. 2.1. The wafer itself has been produced by Tyler Lindemann of the Manfra Group. By repeating the process, it is able to build a stack of heterojunctions, shifting between the elements that it deposits. This sounds straight forward, but the process needs to be highly optimized to reduce defects in deposition steps: deposition rates and substrate temperatures for each layer are optimized; and a close to perfect vacuum is formed so to avoid that the elements deposit diffusively onto the wafer. There is no introduction of organic material to the wafer, and importantly to have no native oxide formation inside the material

stack. This plethora of knobs are optimized to ensure a high mobility 2DEG, with pristine interfaces at the heterojunctions. A MBE system is a formidable piece of machinery, however, for more information on the subject we refer to textbooks such as [45, Chap. 14.11] One of the many expertise of the Manfra Group, is that they can

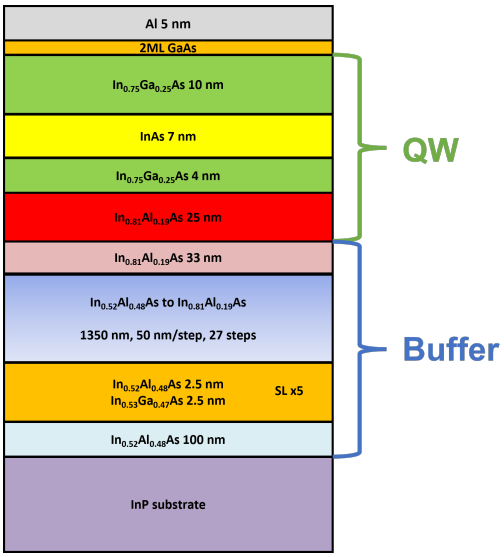

Figure 2.1: *Schematic of the wafer [46] stack grown by Purdue, where the constituents of each layer is noted.*

grow extremely pure and pristine wafers, that we in the TOPO2DEG research group can then use for fabricating nanodevices. The layers of the wafer stack is shown in Fig. 2.1. The make-up of the wafer stack can be split into four categories:

- **The Al top layer**: This layer of 7nm Al introduces superconductivity to our QW. It's epitaxially matched to the III/V and has the added benefit that it protects the III/V underneath from oxidization[1]. Aluminium oxidizes quickly to a depth 3 nm, after which the oxidization becomes quasi-innate [47]

- **The QW**: The active region is the InAs layer with a bulk bandgap of 0.415eV at low temperature, which sits between the two $In_{0.75}Ga_{0.25}As$ barrier materials with a bandgap of 0.691eV[2] again at low temperatures.

- **The substrate**: The iron-doped InP has a bandgap of approximately 1.3eV. There is a substantial lattice mismatch between the InP and our QW (5.87Å

[1]III/V is the SM, called III/V as it is composed of Indium from the III group of the periodic table (group 13) and As which is from the V group (group 15)

[2]This is found using the heuristic Vegard's law $E_{g,In_{0.75}Ga_{0.25}As} = 0.75 \cdot E_{g,InAs} + 0.25 \cdot E_{g,GaAs} = 0.75 \cdot 0.415\text{eV} + 0.25 \cdot 1.519\text{eV} = 0.691\text{eV}$. The equation does not account for bandbending.

in InP and 6.06Å in InAs - 3.13% mismatch) than e.g. GaSb. However, the quality factor of resonators produced on InP is superior [48], which is used in cQED experiments.

- **The buffer**: Due to the aforementioned lattice mismatch between the QW and the insulating InP substrate, a buffer region is employed, to lessen the substrate and QW lattice mismatch. In this wafer stack the largest portion of layers is this buffer region, of which the main part is a graded buffer (blue layer in Fig. 2.1), which gradually changes from a ratio of 0.52-to-0.48 In-Al to a ratio of 0.81-to-0.19 In-Al.

This QW structure is referred to as a shallow 2DEG, due to the proximity to the surface of the wafer: the wave function of the 2DEG has a finite overlap with the heterojunction at the Al layer. This is needed; as explained in Sec. 1.2.2, the proximity effect quickly lessens over greater distances and for high barriers. A shallow 2DEG has the drawback that surface modes (due to defects), after the Al layer is removed, can have a significant effect on the charge carriers of the 2DEG, as we will touch upon in Sec. 2.1.3.

2.1.2 Nanofabrication of Quantum Devices

After having received the wafer stack, we can begin to design and fabricate the devices to be measured in the dilution refrigerator. This method is referred to as the top-down part of the fabrication, as opposed to the bottom up in the MBE done at Purdue. The devices to be measured, are defined using lithographical steps[3], etches, atomic layer deposition (ALD), and metal evaporation. The wafer, which arrives as a 2-inch disc, is cut into chips with desired size (ca. 3x5 mm in most cases), using a diamond scriber, and then the fabrication procedure can begin. The chip itself is prepared by depositing *alignments marks* on the edge of the chips, and are used as markers for the e-beam lithography system, so that the lithographer's software can identify the edges of the sample, such that the pattern does not shift between overlapping lithographical steps. These are deposited using the same lithographic procedure for gates outlined

[3]The etymology of the word comes from the Greek word lithos meaning *"stone"* and graphei meaning *"to write"*. As opposed to the patterning of the 18th and 19th century where stones or metal plates were used to print works of art or text on paper, the electron beam takes the role of the lithographic stone and the paper is substituted with our microchip. The basic principle however is the same; we transfer a pattern (in the computer/e-beam system) to a canvas (the wafer stack)

below. A typical chip in our experiment will hold 9 devices. These devices are isolated from each other, where each device sits on top of its own *"island"* or mesa, separated from other devices by etching away the conducting material between them. The basic steps to fabricate nanodevices (here the recipe for the LoopQubit) is as follows and illustrated in Fig. 2.2:

1. A single drop of diluted (in most cases 4 percent - denoted A4) polymethyl methacrylate (PMMA) e-beam resist is deposited using a micropipette and spread out using a spinner, which evenly distributes the PMMA, after which it is hardened by baking it at 180C.

2. The desired Al design is patterned in an e-beam lithographic step. When PMMA is exposed to the back-scattered electrons from the substrate the molecule breaks up, and its chemical properties change

3. PMMA is a positive resist, which means that exposed regions can be dissolved and removed using a developer. The exposed chip is dipped in a 1:3 Methyl Isobutyl Ketone (MIBK):IPA solution that removes exposed regions, washed with Isopropyl Alcohol (IPA) and blow-dried with nitrogen.

4. The Al is removed in a wet etching step using the branded Transene D etch. It is warmed up to 50°C, whereafter the chip is submerged for 5 s. Immediately after, this is followed by a 20 s rinse in warm water and a 40 s rinse in cold water, after which it is blow-dried using nitrogen

5. A layer of dielectric is deposited. In our fabrication this is done with 15nm of Hafnium Oxide (HfOx), with a dielectric constant $k = \frac{\epsilon}{\epsilon_0} = 16.68$. The dielectric ensures that there is no current flow between the gates deposited after this step and the device's Al/QW.

6. The next step is patterning of the gates. The role of the gates are explained later in this section. The gate design is lithographically patterned, and developed. After this the chip is loaded into a low pressure evaporation chamber. The gates are split into two steps: an inner gate deposition first on top of the mesa, and a outer gate deposition to crawl over the mesa edge[4].

[4]The outer step uses a tri-layer technique. Here two thicker layer of EL9 resist (a copolymer, where Ethyl Lactate has 9% polymers) is used, which is topped by a PMMA A4 layer. When developed this creates a overhang, which facilitates lift-off of the much larger outer gates.

7. The evaporation of gold is done across the entirety of the chip, with a step of titanium evaporation beforehand, that works as a mechanical bonder between chip and gold. The inner gates are ~ 2 nm thick, with a ~ 5 nm thick Ti layer, while the outer gates (to climb the mesa edge) are ~ 400 nm thick, with a ~ 10 nm thick layer of Ti. After this, it is submerged in di-oxalene. The di-oxalene will dissolve the unexposed resist, and after a squirt of Acetone/IPA the gold is only left where the resist was exposed and developed

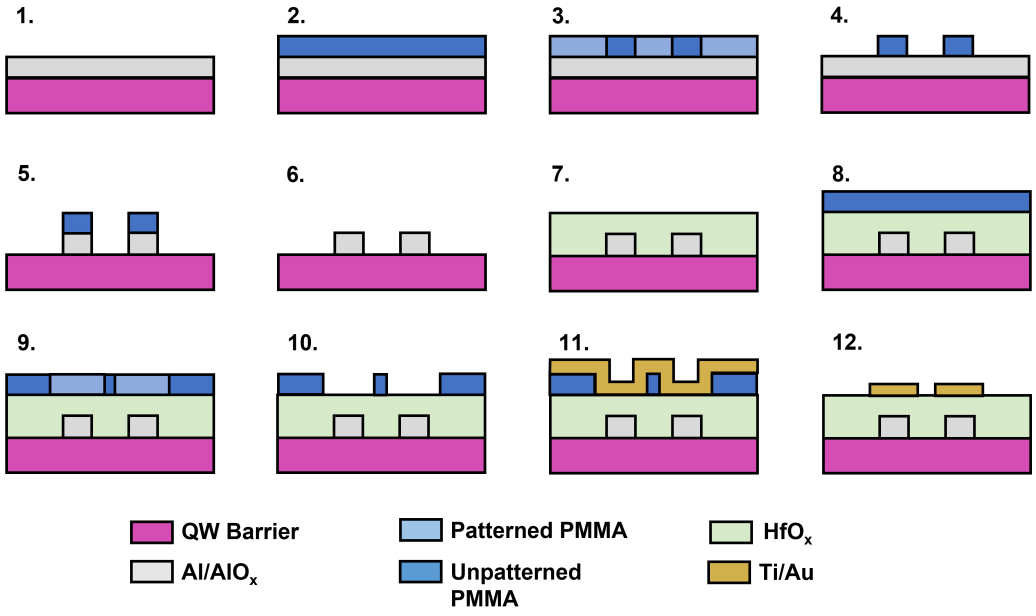

Figure 2.2: *Here we see a side view of the basic steps needed to define a nanodevice in our heterostructure wafer. 1) The bare chip. 2) A layer of PMMA is added. 3) The e-beam patterns the PMMA. 4) The exposed PMMA is developed. 5) Al is removed, but not where PMMA remains. 6) The rest of the PMMA is stripped and the patterned Al. 7) A layer of dielectric is added globally to the chip. 8) PMMA is added on top of the dielectric. 9) The PMMA is patterned with the e-beam. 10) Exposed PMMA is developed. 11) Ti/Au is added globally to the chip. 12) During the lift-off Ti/Au only sticks to places with no PMMA prior to the evaporation step.*

Electrostatically defined nanostructures:

After having loaded the chip into the dilution refrigerator (Sec. 2.2), the gates can be energized, by applying a negative voltage on them, via the DC scheme outlined in Sec. 2.3. We rely on the same mechanism that all SM transistors also use the physics of a Metal-Oxide-Substrate Field-Effect-Transistor (MOSFET). In contrast to FETs,

which either conducts or not (on or off in SM transistors), the systems we fabricate are more controllable, in terms of controlling the amount of conductance through our device. In particular we use them to confine electrons in quasi-1D wires and to obtain tunnelling barriers, where less than a conductance quantum flows. We call these barriers Quantum Point Contacts (QPCs)

The electric fields of a gate (seen in Fig. 1.11b) penetrates the dielectric of the chip. To screen the negative charge on one side of this capacitor (gate-dielectric-device), there is a buildup of positive charge on the chip, directly in the vicinity of the gate, due to Coulomb's law. In the vicinity of the gate, we are therefore able to *deplete* the 2DEG's electron carriers, and we can then constrict the 2DEG into quasi-1D or -0D structures. The same is true for metals; they will also want to screen the electric field of the gate. But while the screening length of semiconductors (Debye length) can be (depending on the carrier density) in the tenths of nanometers, the screening length of a metals (Thomas-Fermi length) is sub-nanometer. Applying a negative charge on the gate on top of a metal will therefore leave the QW underneath the metal unperturbed. As such quasi-1D wires can be defined by lithographically patterning strips of Al and evaporating a gate on top of this: by applying a negative voltage to the gate, the 2DEG is depleted except under the strip of epitaxial Al.

2.1.3 Sources of Disorder

In general, all steps in the fabrication will introduce disorder into the system. Disorder induced scattering is a major cause for concern in most 2DEG systems, which will have an impact on the mobilities of the electrons. Shallow 2DEGs in particular are very sensitive to surface disorders [49].

1. The growth: As pristine a growth might be, stochastic misgrowth is possible, both inside the crystal but also mismatch in the heterojunction of the wafer stack. As material science techniques are optimized this is brought down, and for SMs such as GaAs, that are well established in the SM transistor industry, these misgrowths are close to non-existent. Crystalline defect can introduce carrier into the 2DEG and bring down the mobility of the carriers. However, in shallow 2DEGs, we mostly assume that most of our conduction band filling comes from band bending near heterojunctions, and the surface [50]. Band bending is a phenomenon in heterojunctions where the conduction and valence band of one material needs to align to the conduction and

valence band of another material.

2. The nanofabrication: Etching away Al from the surface of the wafer to expose the QW underneath, is key to electrostatically gate the device. However, in this step we also expose the semiconductor to a diffusive/random dilute Al etch. This roughens the otherwise pristine barrier on the QW, introducing scattering modes. Even if we were to completely etch the Al homogeneously, the surface of any crystal still undergo surface reconstruction, as the vacuum workfunction, Φ, will reconstruct the lattice at the boundary of a crystal to minimize the free energy [51]. This also happens to some degree in heterojunction, where atoms from each alloy/metal will leak into the other crystal and reconstruct the lattice at the junctions. In the growths used in this thesis this is highly minimized, which is the reason we describe the junctions as *pristine*. Furthermore, the stripping of Al also oxidizes the barrier, thereby introducing oxygen molecules into the barrier, which in general also changes the crystal structure.

2.2 Dilution Refrigerators

After having deposited Ti/Au gates on our chip, we can glue the chip with an adhesive to the daughterboard and bond the ohmics and gates to the daughterboard, which in turn is connected to the motherboard of the dilution refrigerator (DR). In this section we will review the working principles of a dilution refrigerator, which is the tool to reach the low temperature (LT) environment ($\sim$ 15mK) needed to explore the physics of our quantum device.

The DR works by the principle of *cooling-by-mixing* [52], which differs from the "normal" way of *cooling-by-evaporation*. In a dilution refrigerator the cooling occurs due to the enthalpy associated with mixing the two liquids, concentrated ^{3}He and the diluted ^{3}He/^{4}He, and is purely quantum mechanical. At its core the cooling is an endothermic reaction as ^{3}He atoms from the concentrated ^{3}He phase into the dilute ^{3}He/^{4}He phase, as the enthalpy of a concentrated ^{3}He liquid, H_{conc}, is different from the enthalpy of a diluted ^{3}He/^{4}He liquid, H_{dil}. As such transport across the phase barrier, characterized by the change of atoms in the concentrated phase, $\dot{n}_{^3\text{He}}$, comes at an enthalpic change, thereby cooling the mixing chamber, which is found by the equation,

$$\dot{Q} = \dot{n}_{^3He}(H_{\text{dil}}(T) - H_{\text{conc}}(T)). \tag{2.2.1}$$

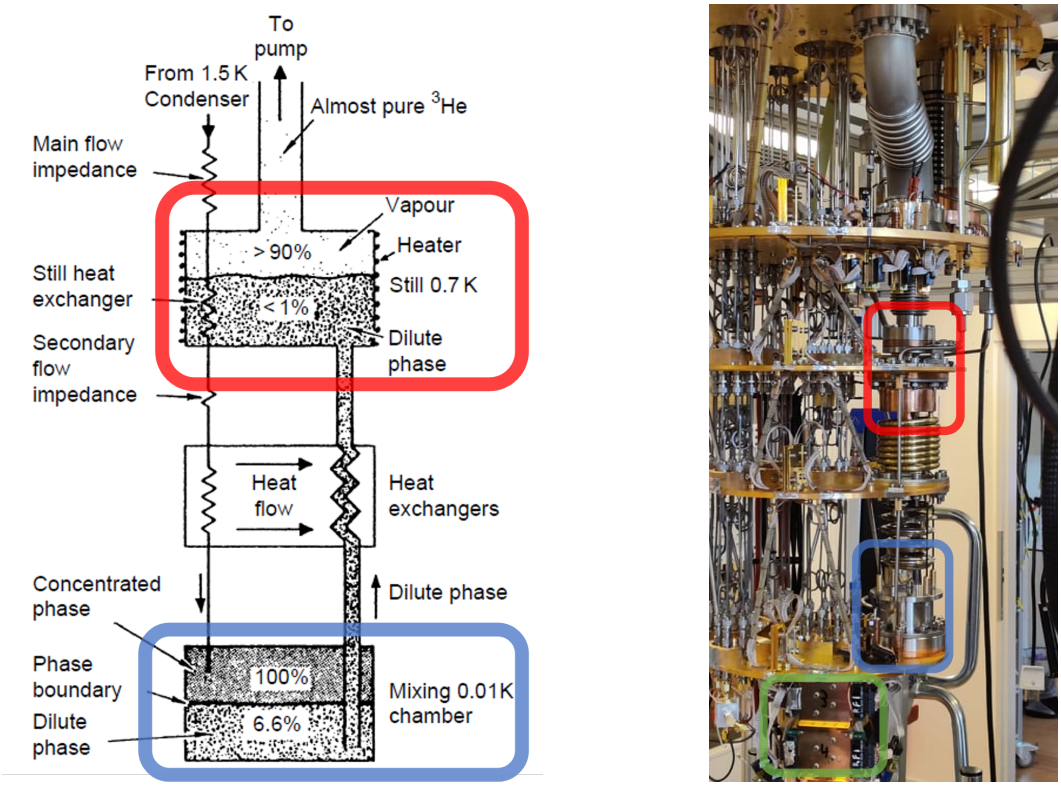

(a) *(b)*

Figure 2.3: *Picture an schematic of a Triton 400 cryogen-free DR.* ***a)*** *Schematic of the basics of a dilution refrigerator [52].* ***b)*** *Picture of a Triton 400 cryogen-free DR, here the mixing chamber is highlighted in blue and the still in red. The RC/RF filters are pictured in the green box.*

The equation describes the cooling power, $\dot{Q}$, which for most modern day DRs are several hundreds of μW's at 100mK. The reason ^{3}He atoms enter the dilute phase is to keep an equilibrium. The ^{3}He/^{4}He liquid continuously leave the dilute phase and enters the still where it is vapourised, leaving only ^{4}He. This in turn creates an osmotic pressure in the mixing chamber that drive transitions into the dilute phase. ^{3}He vapour is then circulated and cooled again, to supply the concentrated phase at the mixing chamber. The DR used in this experiment is a Triton 400 from Oxford Instruments, a so called cryo-free or dry DR. It is called this because the precooling of ^{3}He vapour is done via pulse tube coolers, as opposed to wet DRs that precool ^{3}He-vapour with liquid nitrogen. As is evident from Fig. 2.3b, there are several brass plates. These separate the stages of DR, going from room temperature to $\sim$ 15mK. When leading currents (DC and RF) through such a system, thermalization of the signal and attenuation are key principles, that should be accounted for (see Sec. 2.3).

2.3 Transport measurement scheme

Much of the wiring seen in Fig. 2.3b accommodates RF signal lines; this is attenuated at each stage of the dilution refrigerator, and sent into a directional coupler, which connects to the daughterboard, on which we can bond a inductor chip with a bias tee. The reflected signal comes out of the directional coupler and is amplified at a Weinreb cryo-amplifier at 4 K. In an RF measurements, we would employ an ultra high frequency (UHF) Lock-In amplifier (LIA) to analyse the signal. In the measurements of this thesis, we use a low frequency LIA signal, to measure the conductance of a nanodevice. Though it is an AC signal, we describe it as a DC measurement, the reason we will explain in this section. The DC voltage we use to energize the gates of the device and the low frequency LIA signal is sent via strips of wires loomed together, through the different stages of the DR, into custom RC/RF filterboards (highlighted in green in Fig. 2.3b). From the filterboards the signal is sent to the *puck*; a sample holder which can be retracted from the DR without warming the fridge to room temperature every time a sample needs to be switched. This in turn is connected to the motherboard on which we connect the daughterboard that holds the chip to be measured.

Fig. 2.4 shows a rudimentary scheme, of how we control voltages on the chip. A low frequency AC voltage signal is sent from a Stanford Research SR830 Lock-In amplifier (LIA) [53], through a AC divider with a factor of 10^{-5}, yielding a 3μV excitation. The voltages of the gates are controlled by a QDAC voltage generator. Fridge and voltages are connected via a break-out-box, and as it passes through the cold stages of the fridge the signal becomes thermalized, until it reaches the RC/RF filter which ensures the electronic temperature reaches μeV. The outgoing current from the sample is then passed through an I/V converter, amplifying the signal $10^8 V/A$, before being measured in the LIA. For 4-terminal measurements, where we measure the current through the system and the voltage across it simultaneously, the voltage signal is amplified in a ETH voltage amplifier with a gain of 10^3 at room-temperature before it is measured in a LIA. Additionally the DC bias signal has an DC divider with a factor of 10^{-3}.

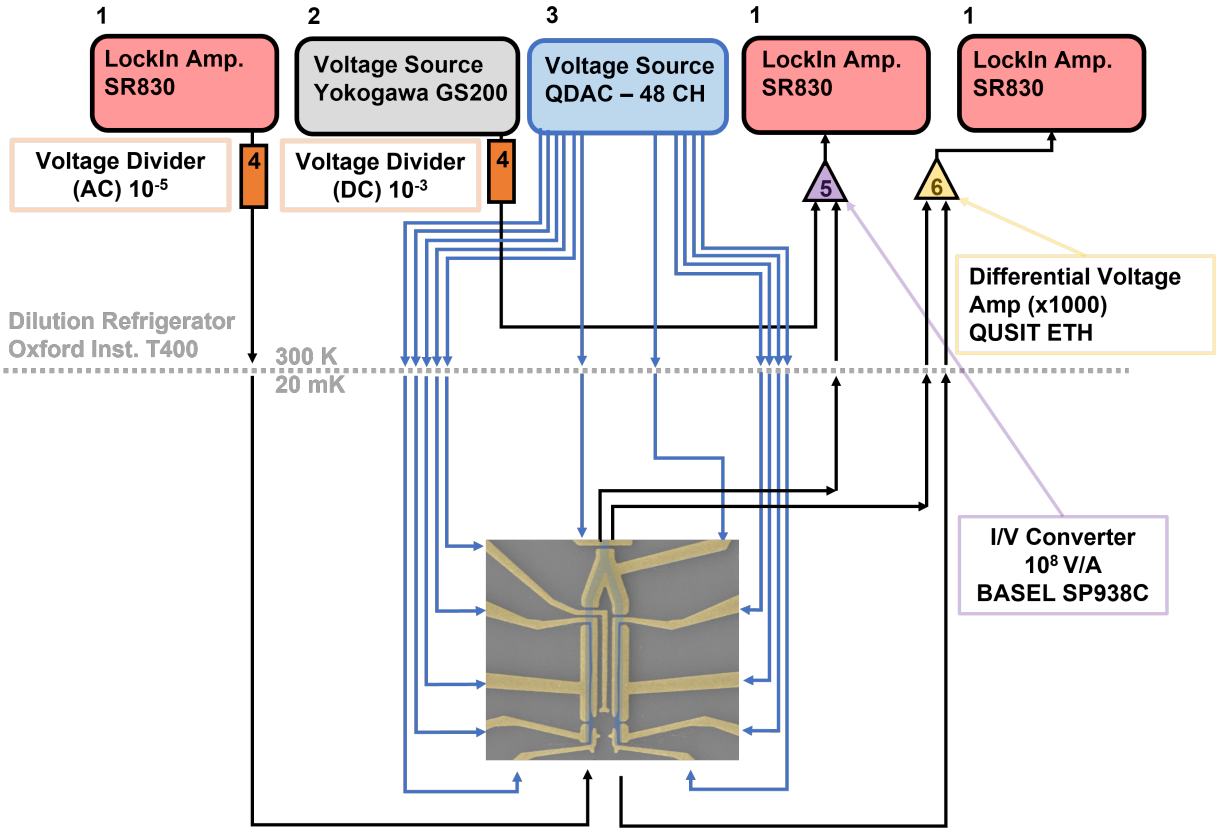

Figure 2.4: *Measurement schematics of the DC setup: Blacklines are used in the 4-terminal measurement, and blue lines energize the gates.* ***1*** *SR830 LockIn amplifiers from Stanford Research. All three are slaved, meaning they measure/source a signal at the same frequency.* ***2*** *The Yokogawa Source Measure Unit (SMU) GS200.* ***3*** *A QDAC Q301 high-precision low-noise voltage generator.* ***4*** *A custom voltage divider.* ***5*** *A voltage/current converter from BASEL model SP983c.* ***6*** *The voltage across the device is amplified in an ETH low-noise differential voltage amplifier from QUSIT, before being measured in an LIA.*

2.3.1 Tunneling Spectroscopy - Resolving Local Density of States

For a condensed matter experimentalist, one of the most seminal technical discoveries was made in 1960 by Ivar Giaever. In [54] he described, how by forming a S-I-N junction[5], the superconducting gap - described by BCS theory four years earlier - could be resolved in the differential conductance. What he found was that with a tunnel barrier between two reservoirs, the current flowing between the two would be proportional to the convolution of the density of states in both [23],

$$I = \frac{G_0}{e} \int_{-\infty}^{\infty} dE_1 dE_2 D_1(E_1) D_2(E_2) [f_1(E_1) - f_2(E_2)], \tag{2.3.1}$$

where the two reservoirs have a DOS $D_i(E_i)$, and $f_i(E_i)$ is the Fermi-Dirac distribution for either reservoir. For simplification we can assume an energy independent transmission, giving the conductance quantum $G_0 \equiv \frac{2e^2}{h}$. If $D_1(E) = D_N$ is an energy independent DOS in a normal lead, and we define $E_1 = E_2 - eV_{SD}$, we can then simplify the expression. It now reads,

$$I = \frac{G_0}{e} \int_{-\infty}^{\infty} dE D_N D_2(E) [f(E - eV_{SD}) - f(E)]. \tag{2.3.2}$$

The differential conductance $G = dI/dV_{SD}$ is for low temperatures given via a linear response [23],

$$G = \frac{dI}{dV_{SD}} = \frac{G_0}{e} D_N D_2(eV_{SD}). \tag{2.3.3}$$

In many modern experiments, the insulating material is replaced by a QPC, that fixes the conductance to less than a conductance quanta. When the low-frequency (30 to 200 Hz) AC voltage of 3 μV from a LIA is applied to the device, and the differential current dI is passed through a I/V converter (a Physics BASEL SP-983c) and can be measured in a LIA. The differential four terminal voltage dV across the device is measured in an additional LIA. Correspondingly, we can define the four terminal differential conductance, $G = dI/dV$, which let us probe the density of states of the reservoir.

[5]The insulator in his experiment was a thin oxide layer between the normal metal and the SC

CHAPTER 3

Results of Transport Measurements

In this chapter we will show many of the results produced during this thesis. The main result is the demonstration of a controlled coupling between a QD and SC leads. It is shown and discussed, that by changing this knob, using electrostatic gates (Sec. 2.1.2) (which generally does not have a monotonic relation to gate voltages applied), a plethora of different phenomena takes place in the same hybrid material system. For the sake of brevity a dictionary on the gate abbreviations can be found in App. A, and the exact gate voltages for each figure can be found in App. B. A false color SEM of the device design on which the following measurements are performed is pictured in Fig. 3.1, and the expected placement (as we apply a negative voltage to the surrounding gates) of the QD is shown in red.

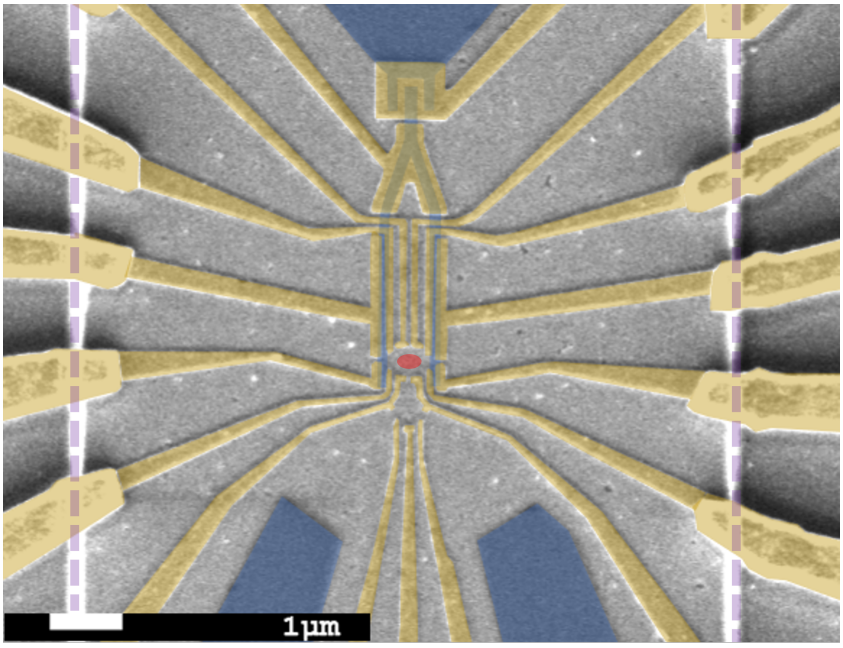

(a)

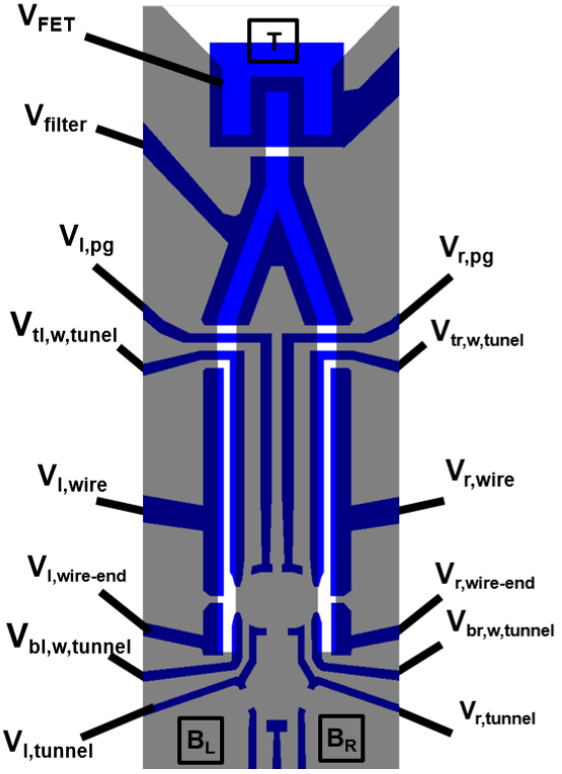

(b)

Figure 3.1: a) *False colour SEM of the LoopQubit device. The scale-bar is 1 µm. The gates are highlighted in yellow, and the aluminium is highlighted in blue. The bright purple line marks the MESA. Within the grey area is the SM/QW, while the grey area outside is InP. The red dot shows where we expect the QD to form.* ***b)*** *The LoopQubit design with gate abbreviations. Gates are coloured blue, aluminium is coloured white, and the SM is coloured grey. Between B_L and T we source a current, by applying a small AC voltage excitation (3 µV for transport measurements and 15 µV for the 3rd harmonic measurements), and between B_R and T we measure the voltage drop across the device: this is referred to as a 4-terminal measurement.*

3.1 Tuning the Device

The devices measured at low temperature in our dilution refrigerator, undergo a series of testing / tuning. Checking if the gates are responsive, the quality of the tunnel barriers, and continuity of the Al wires is key to a well working experiment. As each generation of devices generally adds more gates, to get the desired control, this is quite an undertaking, with a large gate voltage parameter space to explore. For this experiment 13 gates are energized, see Fig. 3.1 and App. A. In this section we describe a series of standardized measurements to test and calibrate the device.

Calibrating the device: As mentioned in Sec. 2.1.2, we laterally define our device using electrostatic gates. By applying a negative bias to the gates, we can deplete the 2DEG, and as electrons are unable to conduct under the gates, the effect is that the resistance rises, $R \rightarrow \infty$. In our 4 terminal measurement scheme (Fig. 3.1) we can measure this as a decrease in conductance. The response of the gates are measured in *depletion curves*, an excerpt of these is shown in Fig. 3.2a and Fig. 3.2b. We can measure at what voltage the gate has depleted the 2DEG directly below it, which is seen as a sharp decrease of conductance, as highlighted with orange arrows in Fig. 3.2a and Fig. 3.2b. After this the gates can also deplete in their immediate vicinity; this is seen as a gradual decrease of conductance. It is also important to check whether there is a leakage current from the gate and onto the MESA. A leakage plot can show this, where we measure the DC component of in the Lock-In signal in a Keysight digital multimeter, as we energize the gate. A lack of leakage is shown in Fig. 3.2c, in our devices we see that leakage is when we measure several nanoamperes of current.

A feature worth noting is that measuring conductance when moving a gate more negative in one range, and then moving the gate more positive in the same range, does not produce the exact same measurement. This effect is known as hysteresis. The effect can mean that the pinch-off voltage (the voltage at which a set of gates cuts off current through the device) is different, depending on the direction we sweep the voltage. Therefore, for all measurements shown in this result section we only measure conductance as we sweep the gates towards more negative voltages.

Corner features: We can pinch-off conductance all together through the device by using gates in parallel with each other (Fig. 3.2b). As an example $V_{bl,w,tunnel}$ and

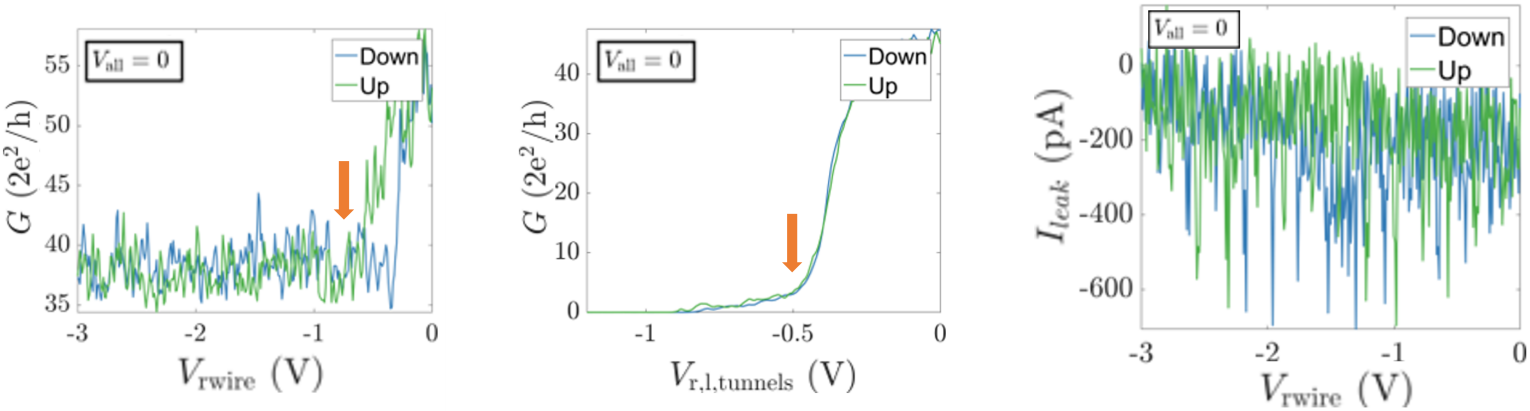

(a) *(b)* *(c)*

Figure 3.2: ***a)*** *Depletion curve of the right wire plunger, $V_{r,wire}$. Below -1 V the gate has depleted the 2DEG underneath (orange arrow).* ***b)*** *Depletion curve of the normal lead tunnel barrier gates, $V_{l,tunnel}$ and $V_{r,tunnel}$. At $V_{r,l,tunnels} = -0.5$ V the gates have depleted directly under them (orange arrow). At $V_{r,l,tunnels} \sim -0.8$ V conductance is pinched off.* ***c)*** *Lack of leakage of the right wire gate, $V_{r,wire}$, to the ohmics as the gate is energized. The colour of the curves (green and blue) corresponds to whether the gate voltage goes towards more negative values (green) or towards 0 voltage (blue).*

$V_{tl,w,tunnel}$ can be energized to control the conductance into the left wire. Tunnel barriers can also be controlled in sequence, that is we can view them as parallel or series resistors. The tunnel-tunnel maps of series and parallel resistors/barriers are shown in respectively Fig. 3.3a and Fig. 3.3b. Generally, we assume that tunnel barrier where gates define an equal potential on either side of the QPC to be optimal. Optimally, this has the effect that a saddle point QPC is formed, which should have the best chance of adiabatically connecting the SC-leads, the N-lead or the QD.

Phase Control: When we have both wire tunnel barrier open, we can check whether charges move coherently in the loop. This is checked by the application of a perpendicular magnetic field, which threads fluxes within the superconducting loop. Here it can be shown that changing the phase difference between the two SC nanowires modulates the ZB states with a phase $2\pi \sim 1.4$mT (Fig. 3.4), corresponding to the loop area, 1.65 μm^2.

Field correction: The placement of the chip onto the daughterboard is done by hand using an adhesive (PMMA A4). This generally introduces a slight rotation of the chip about all three axes. Using the phase coherence of the loop, which is shown in Fig.

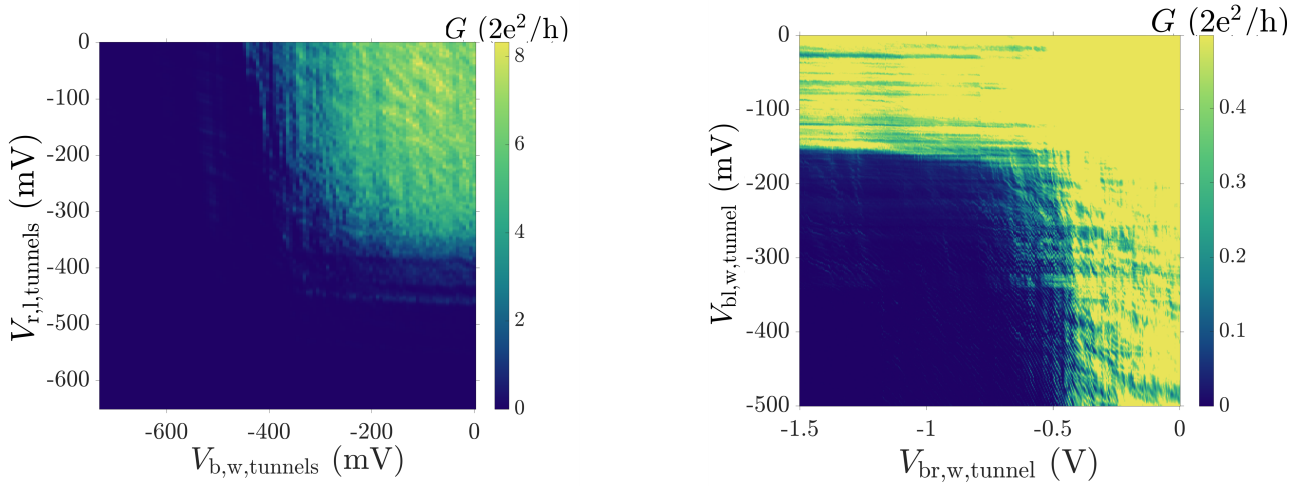

Figure 3.3: a) *2D voltage scan of the normal lead tunnel gates, $V_{l,tunnel}$ and $V_{r,tunnel}$, and the bottom part of the wire tunnel gates, $V_{bl,w,tunnel}$ and $V_{br,w,tunnel}$ are energized simultaneously, and an inverted corner feature is measured. Energizing either, can pinch off conductance through the device. Resonances are also visible, as stripes of higher conductance* ***b)*** *The two bottom wire tunnel gates, $V_{br,w,tunnel}$ and $V_{bl,w,tunnel}$, are parallel resistors as energizing neither gate can pinch off conductance. Here the normal lead tunnels are also energized and therefore in the corner (when a tunnel barrier to the SC leads have formed) we see the emergence of Coulomb resonances (Sec. 1.2.3). In both plots finite gate voltage is applied to the top wire tunnels, $V_{tl,w,tunnel}$ and $V_{tr,w,tunnel}$. Otherwise the $V_{b,w,tunnels}$ cannot pinch off conductance.*

3.4, or driving the SC material normal using the magnet, is the ways to measure the correction needed. As we sweep the field in one direction, we can add an additional component in the orthogonal directions to make sure, that all (or most) of the field truly is in the desired direction. In Fig. 3.4 we do not expect the phase dependence of the loop to depend on $B_{\parallel}$, which means that the uncorrected parallel magnetic field has a component in the direction perpendicular to the plane of the chip. By adding a component in the opposite direction of the plane, we can define a new parallel field, B_{zc}, which only has a direction parallel to the plane of the chip.

The superconducting gap: When initializing the gates that control the coupling between N-SC or QD-SC it is important to find whether a regime with a well-defined superconducting gap we can be resolved, as this is a measure of the quality of the QPC. In the devices we measure, we restrict ourselves to using the $V_{bl(r),w,tunnel}$ gates to open and close the SC wire QPC as this has the least impact on the potential of the

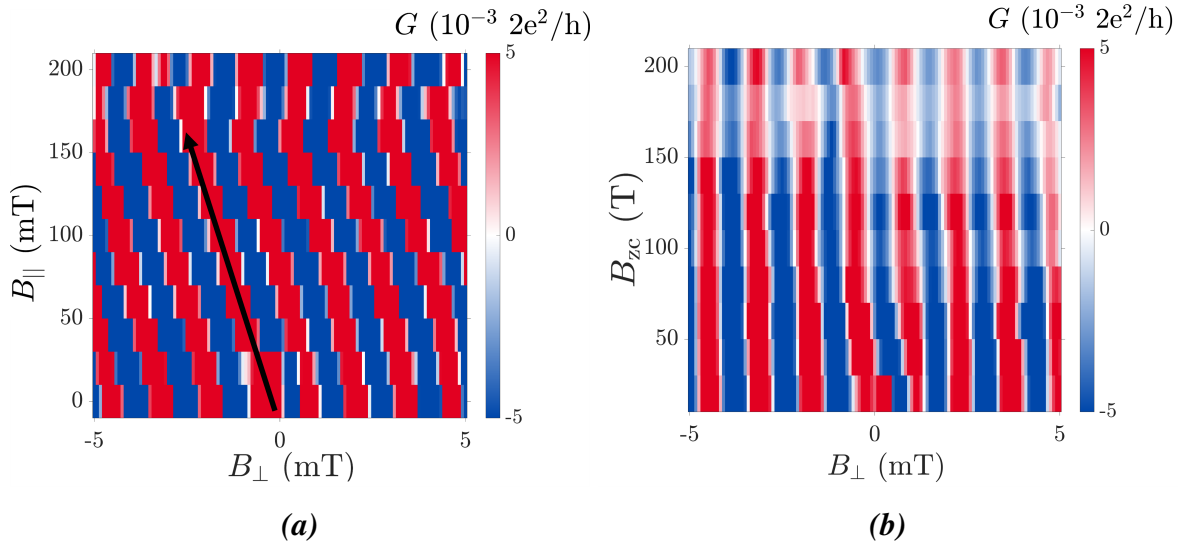

(a) ***(b)***

Figure 3.4: ***a)*** *Phase oscillations (tuned by $B_{\perp}$) has a drift in the $B_{\parallel}$ direction, following the black arrow, due to a misalignment of the chip.* ***b)*** *Adding a $B_{\perp}$ component to $B_{\parallel}$ fixes the drift. Background correction is done using a Savitzky–Golay filter function in Matlab*

wires of the two SCs, see Fig. 3.5. In Fig. 3.5, we see that by forming a QPC with $V_{br,w,tunnel}$ we can probe the LDOS of the right SC wire: a hard superconducting gap of $\sim 200\mu$eV is observed, which is expected for this wafer. It should be noted that the gate voltages where a hard superconducting gap is resolved in spectroscopy, is not by necessity the regime where an Andreev dot is formed (Sec. 3.2.2) or where wire-dot hybridization is optimal (Sec. 3.3). When we have formed the SC-QPC-N, we can check the parallel field dependence, Fig. 3.6. We see that the gap persists for at least 3T of parallel magnetic field, when sweeping the corrected parallel field, B_{zc}.

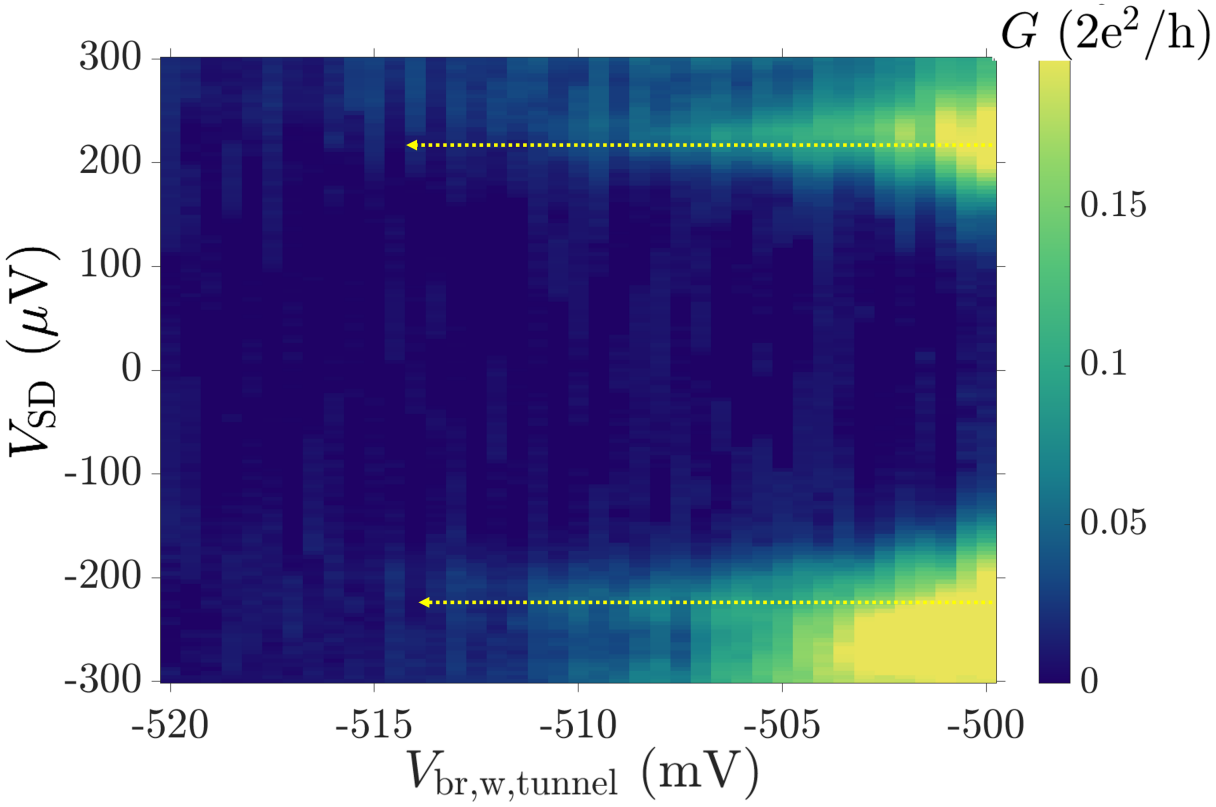

Figure 3.5: *Gap spectroscopy of the right wire as we energize the right tunnel barrier. A 2D plot showing the gap emerging (being resolved) as the tunnel barriers gate voltages is negative enough to transition into the tunnelling regime. The gap is here highlighted by the dotted yellow arrows. To find a hard gap SC DOS we apply a large negative voltage of* -3.15 *V to the right wire to expel any states in the subgap DOS.*

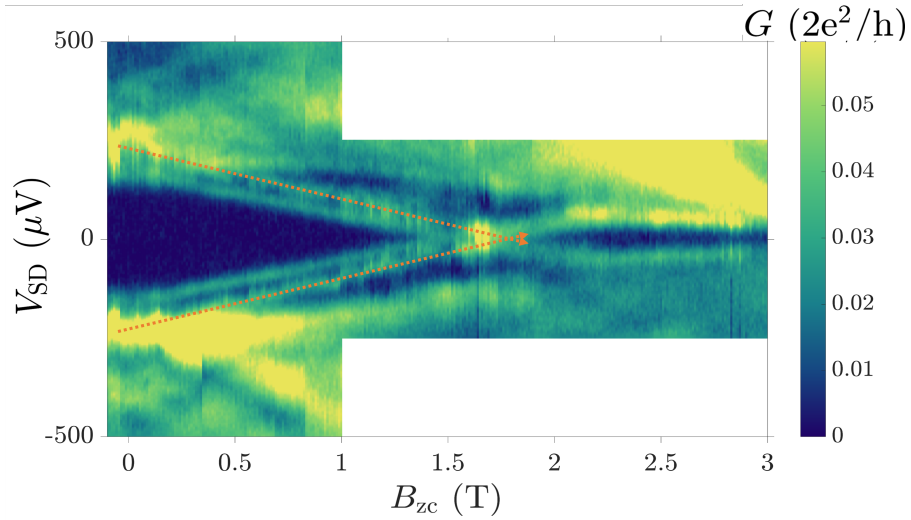

Figure 3.6: *Closing the gap of the right wire with the corrected parallel field, B_{zc}. The wire plunger gates are set to a negative voltage needed to remove subgap states and form a hard gap SC. However, we still see that discrete wire states (dotted orange arrows) are driven to zero energy via the Zeeman energy for high parallel fields.*

3.2 Quantum Dot Spectroscopy

3.2.1 Normal Lead - Quantum Dot - Superconductor System

We have previously discussed the spectroscopy of a QD (Fig. 1.8 in Sec. 1.2.3), and how the Coulomb Blockade phenomena produces the phenomena know as Coulomb diamonds. However, in the LoopQubit a SC is connected to the QD, and so instead of a N-QD-N system, we measure a N-QD-SCs system. For now, we ignore the phase of the two SCs, and instead we can simply imagine that when two SCs are connected instead of one SC, we have twice as many conduction channels. Phase is not important; due to large tunnel barriers there are no coherent transport of quasiparticles across the QD cavity [55]. We will also explore the regime of increased coupling in later sections. This system is well explored in references such as [55, 56]. As we probe the system using spectroscopy, we find that the Coulomb diamonds are shifted in bias, $\Delta V_{SD} = \Delta/e$, and gate, $\Delta V_{pg} = 2\Delta/(\beta_N e)$, see Fig. 3.8a, where β_N is the lever arm of the normal lead. The reason behind this is best seen following the scheme of Fig. 3.7. Firstly, due to the superconducting gap, transport only takes place if we

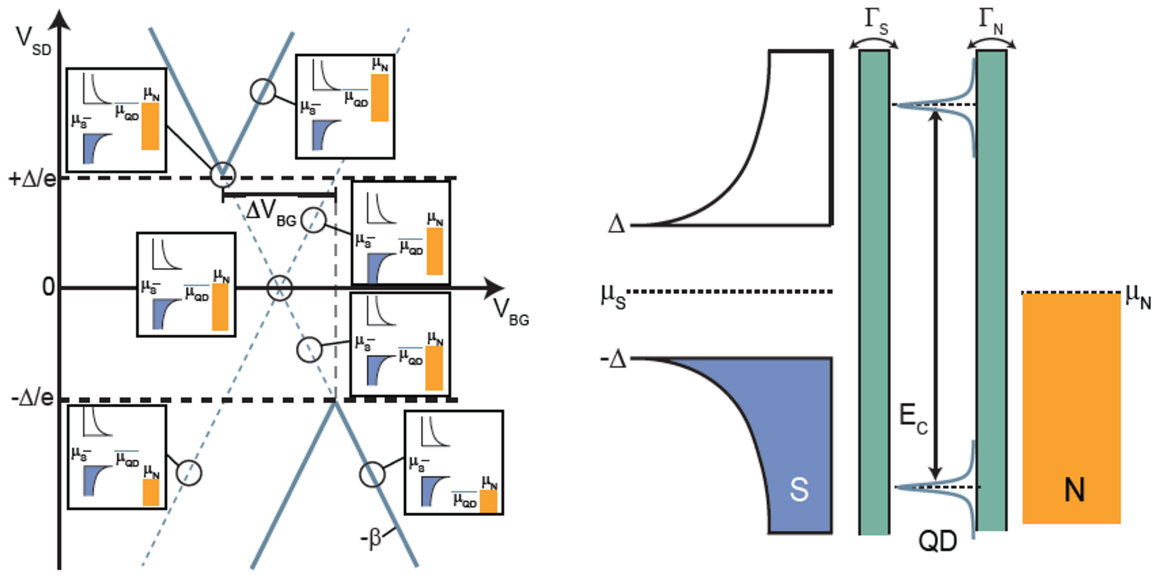

Figure 3.7: *The N-QD-SC system. For different points in gate-bias (the Coulomb diamond scheme), the chemical potentials of the N, SC and QD is shown in relation to each other. Figure from [55]*

apply a bias of Δ/e. However, we also need to align the chemical potential of the dot, so that it is aligned with the coherence peak of the BSC spectrum and the normal

lead. By biasing, due to the lever arm of the source/drain lead, we have already moved the level $e\Delta\beta_{S/N}$. We need to move it an additional $\delta E_+ = \Delta - e\Delta\beta_{S/N}$. The same is true for negative bias where we need to move it $\delta E_- = -\Delta + e\Delta\beta_{S/N}$. This means that the energy needed to move it is $\Delta E = 2\Delta(1 - e\beta_{S/N})$ in energy. In voltage this is $\Delta V_{pg} = 2\Delta(1 - e\beta_{S/N})/(e\beta_{S/N})$. In a decoupled dot with large Γ_N or Γ_S, we take $\beta_{S/N} \ll 1$ and so $\Delta V_{pg} \simeq 2\Delta/(\beta_{S/N}e)$, as previously stated. We also show that softening the superconducting gap, by applying a perpendicular magnetic field. This brings the tips of the diamond down towards zero bias again (Fig. 3.8b). This is due to the fact that at finite magnetic field, the gap becomes less hard (meaning a continuum of states fill the subgap spectrum) as well as the gap itself shrinks in size. This means that conductance at $V_{SD} < \Delta(B = 0)$ becomes possible.

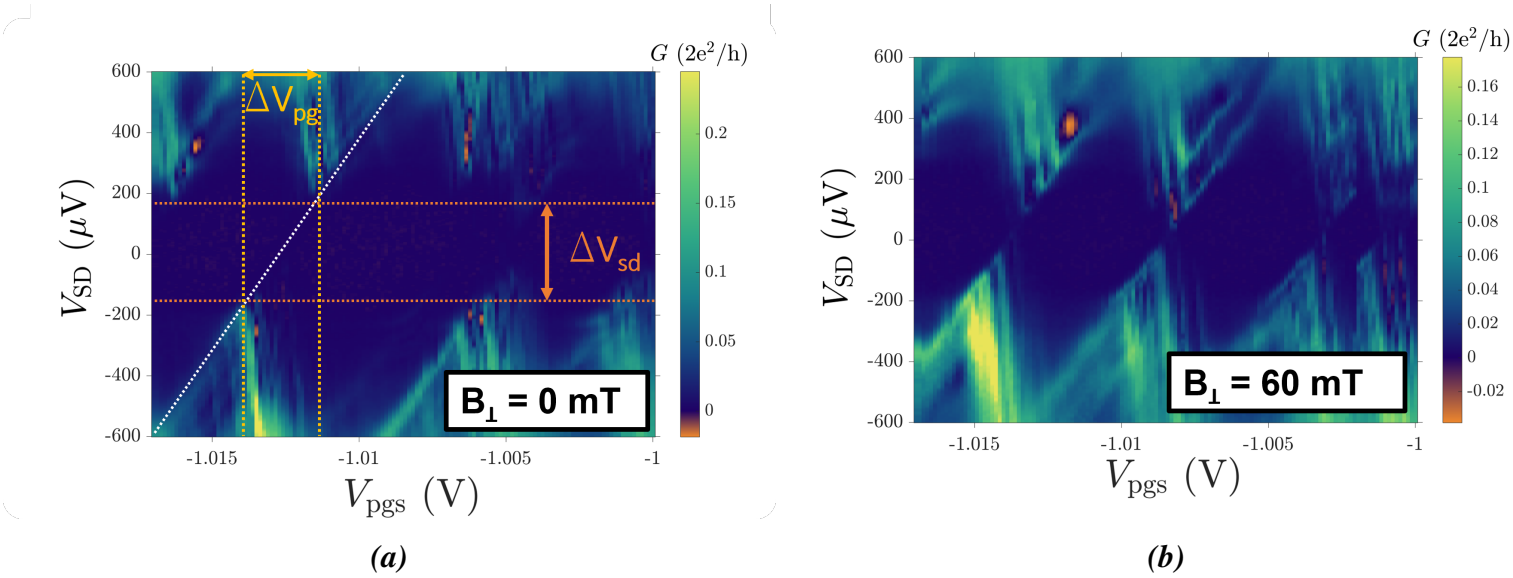

Figure 3.8: *Spectroscopy of a QD-SC system in the decoupled regime at* ***a)*** *0mT and* ***b)*** *60mT perpendicular field. Here we highlight the two shifts in bias, ΔV_{SD}, and gate, ΔV_{pgs}. At finite perpendicular field we begin to close the gap, which in turn also closes the separation between the tips of the diamonds. The perpendicular critical field of Al nanowires is $B_\perp \sim 300mT$, but already at $B_\perp \sim 60mT$ the gap is soft (the SC DOS has a continuum of states below Δ) to a degree that the shift in bias is largely suppressed towards zero bias.*

3.2.2 The Andreev Dot - A Quantum Dot in a Josephson Junction

Having discussed the physics of both quantum dots and Andreev reflections in Sec. 1.2.3 and Sec. 1.2.2, and the results of a N-QD-SC system in Sec. 3.2, we will now turn to the physics and observations of an Andreev Dot (AD)[1], which is a QD embedded in a Josephson Junction (JJ), on the basis of [57]. The physics of an AD is closely related to that of a Yu-Shiba-Rusinov (YSR) state and Kondo physics [58]. These types of systems show an interesting competition between superconductivity, the Kondo effect, and the spin-orientation of the QD. When the QD in the JJ has a total spin, $S_{\text{tot}} > 0$, (generally an odd number of electrons), the quasiparticles of the SC will want to screen this impurity, so the many-body wavefunction has no magnetic moment [59, 60]. An AD has three main components to tune: The detuning of the AD potential, ε, the coupling to the two SC leads, Γ, and the phase difference between the two SC leads, φ. A zoom-in of the schematic that shows the QD and the two superconducting leads, of this device is shown in Fig. 3.9. We also introduce the configurations of the device, below the picture (1, 2, 3, and 4 in Fig. 3.9), which is used from now on to keep track of which regime we are in.

The coupling, Γ, between the SCs and the QD cavity is readily changed in our device using the SC tunnel gates $V_{\text{t/b,r/l,w,tunnel}}$ seen in Fig 3.9[2]. As such, applying a negative voltage on these gates lets us move through the coupling regimes cited in [56]. The weakly coupled regime, $\boldsymbol{\Gamma \gg \Delta}$, was covered in Sec. 3.2.1, which leads us to now discuss the two other regimes.

Strongly Coupled Regime - $\boldsymbol{\Gamma \ll \Delta}$: In this regime the Cooper pairs of the SC can coherently traverse the cavity and so a supercurrent flows across the JJ. This is facilitated by a negligible charging energy of the QD, meaning two electrons can be added to the dot at a time, as opposed to how we would generally think about QDs. Therefore, we are left with a simple Josephson junction (JJ) and the physics accompanying this. In our case, when doing LDOS on the system we see a soft gap

[1] A plethora of names are used for this kind of system, which mostly depends on the physics trying to be explained: Andreev dot, Josephson dot, magnetically induced YSR bound states, and π/0-Josephson Junctions and many others.

[2] One thing to add to this is also that applying more negative bias on the gates does not necessarily mean that the system is more decoupled. In any experiments it is possible that the tunnel gates go through resonances, even as they are moved to more negative values. Resonances can come from many sources, but generally they only persist for a short time, and show up as a peak in conductance superimposed on the generally downward trending conductance

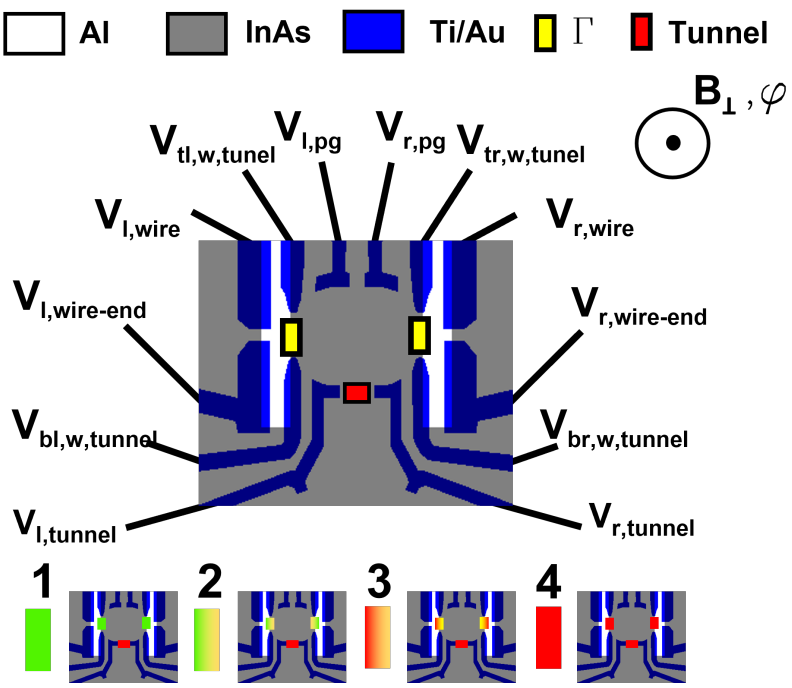

Figure 3.9: *Simplified schematic of the Andreev Stadium part of the LoopQubit with gate name abbreviations, where the yellow blocks symbolize a tunable tunnel barrier of strength* Γ*, the red block is a strong tunnel barrier to ensure that we are measuring the LDOS of the system. Four pictures underneath the picture illustrates what regimes we will demonstrate in this work. From left to right:* ***1)*** *Opening the dot to form a Josephson junction.* ***2)*** *Forming an spinful Josephson junction (an Andreev dot).* ***3)*** *The cotunneling regime with both wire semi-closed.* ***4)*** *A strongly decoupled dot (N-QD-SC system). In the following sections, we will elaborate what the results of the different regimes are.*

proximitized SM (Fig. 3.10), with phase dependence given by the area of the loop.

Intermediate Coupling Regime - $\Gamma \sim \Delta$: This is the regime of the Andreev Dot. Here we should differentiate based on the charging energy, E_C, compared to the superconducting gap, Δ [58]. The two regimes, $E_C > \Delta$ and $E_C < \Delta$, both involves the screening of the local spin of the dot by quasiparticles of the SC lead. Let us imagine 3 occupational levels of the dot: N-1, N and N+1 electrons, where N is odd.

For $E_C < \Delta$; the system has a small charging energy. Due to the small charging energy the odd occupied level N, will also be able to accept or reject an electron. This can be understood from the point of view of Andreev reflections [61]. This leads to an excited subgap state due to hybridization of the $N \pm 1$ levels.

For $E_C > \Delta$; the problem is rooted in a superconducting Kondo or YSR model [58].

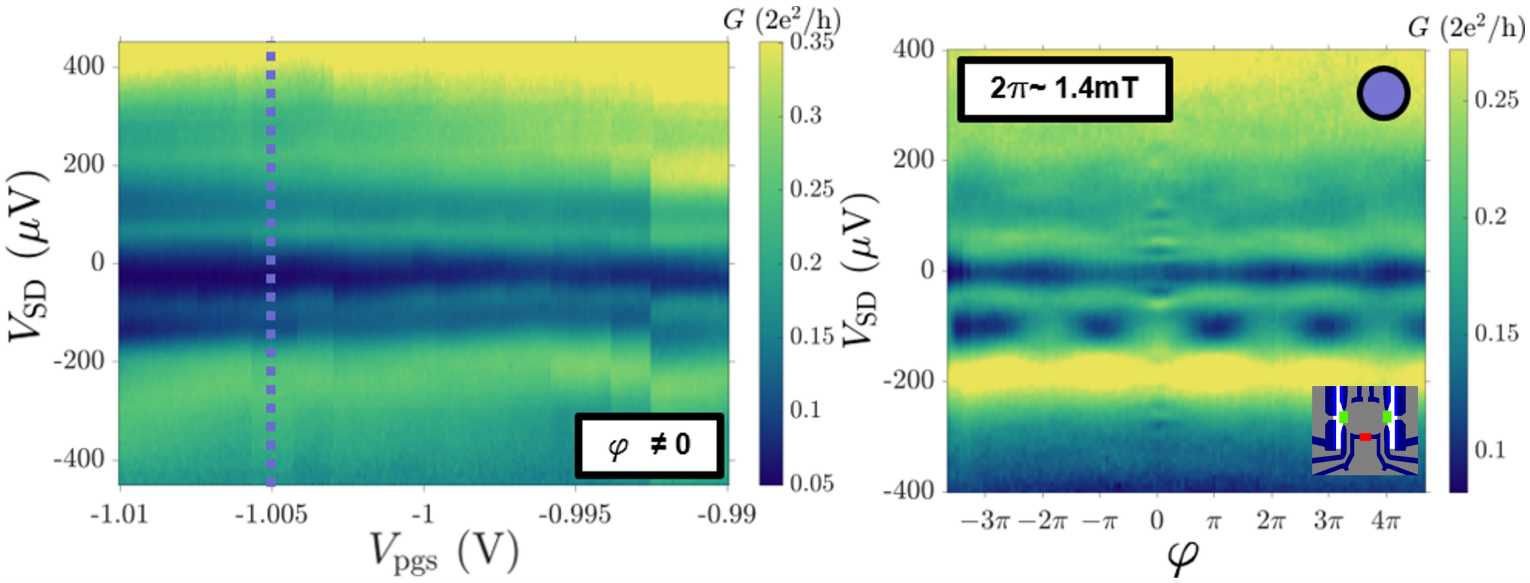

Figure 3.10: ***Right:*** *LDOS shows a soft gap proximitized SM, with broad states within the gap, originating from ABSs.* ***Left:*** *Phase dependence taken at linecut shown in purple. We see that the conduction is strongly phase dependent. One oscillation, 2π, corresponds to the magnetic field needed to thread a flux through the loop, $2\pi \simeq 1.4mT$*

Differentiating the two cases (YSR or Kondo) is whether the Kondo temperature, T_K, is larger or smaller than the gap, Δ. For a large T_K the SC completely screens the spin, and a singlet state is formed. For a weak coupling, where the QD is a doublet ground state, an excited YSR singlet state is formed. Previous measurements, see Fig. 1.9b, let us can estimate a charging energy of $E_C \simeq 600\mu eV$; well within the $E_C > \Delta$ regime.

Phase Dependence of an Andreev Dot: As we apply a perpendicular magnetic field, we thread flux through the loop, thereby changing the energy of the ground state. In the odd occupational lobes, we find in theory that it is a π-JJs, meaning that the ground state has an energetic minimum at $\varphi = \pi$, while the even occupational lobes are 0-JJs, meaning that the ground state has an energetic minimum at $\varphi = 0$. In Fig. 3.11, we see clear phase oscillations of one lobe. However, we only find phase dependence for one lobe. In this measurement we find that the lobe starts to close, but not closing all the way which theory predicts. In other experiments [57], is has been shown that it should close completely and form a single crossing at zero energy in the middle of the lobe.

An important phase diagram to understand the width of the odd occupational lobe in

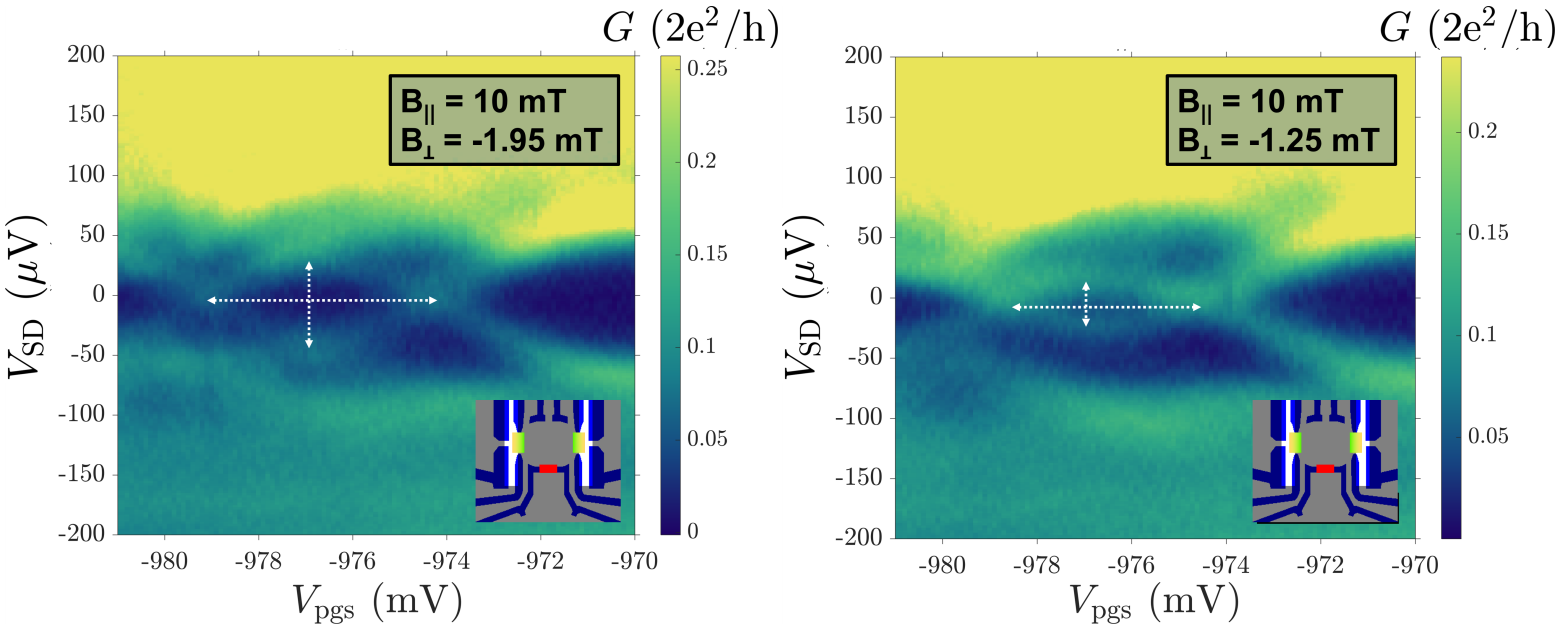

Figure 3.11: *Spectroscopy of what we attribute to be an odd occupational ground state of an Andreev dot for* ***a)*** $\varphi = \pi$ *and* ***b)*** $\varphi = 0$. *Clear phase oscillation is observed (illustrated by the crossed arrows). We do not see phase dependence of the neighboring lobes, though they should also be phase dependent.*

an Andreev dot, is seen in Fig. 3.12, where the boundary of a 0 and π junction is drawn, as we vary the coupling and the chemical potential of the dot we can transition between a singlet or a doublet ground state, for respectively a 0- or π-JJ.

The description of an Andreev Dot is integral to understanding the system thoroughly, and also shows a high degree of tuning capability of the system that we can go from this regime, to the one described in Sec. 3.3. Though the observation of phase dependent states in this device has proven difficult, it should be mentioned that they have been seen in other experiments that have been performed in the course of this thesis

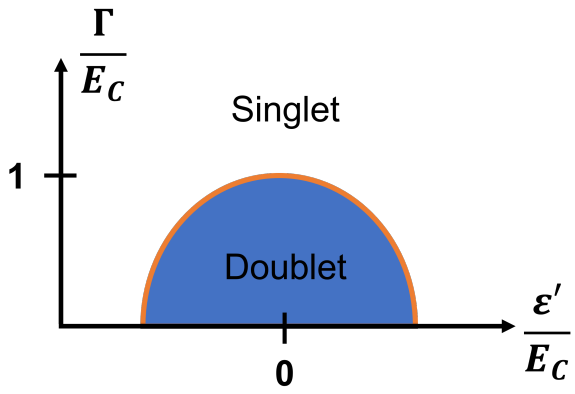

Figure 3.12: *Phase diagram of an Andreev Quantum Dot, where the singlet and doublet ground states phases are pictured, depending on the coupling strength, Γ, and the AD detuning, ε′. The phase boundary is colored orange. Here ε′ is the detuning of the chemical potential, chosen to be zero exactly between the two zero energy crossings.*

3.3 Andreev Bound States of Wires and Cotunneling Spectroscopy

In SCs where we do not apply as negative a voltage to the wire plunger gate, $V_{r,wire}$ and $V_{l,wire}$, the *hardness* of the gap is modified and discrete subgap states can appear in the DOS. The description of these states, which is missing from Sec. 3.2.1 and Sec. 3.2.2, will be covered in this section. For an AD, we generally assume that we have two hard gap superconductors at either end of the cavity, and that the ground state of the system form as the QPs of the SCs screen the spin of the QD. However, introducing discrete subgap state in the SCs we change the picture dramatically. Instead of forming subgap state because of a hybridization effect between quasiparticles of the SC and electrons on the QD, the subgap states already populate the spectrum of the SC, originating from ABSs in the wire[3]. Furthermore, the QD should also be in a regime where it is enough decoupled from the SC lead, such that there is no screening of the spin of the electron on the QD by QPs from the SC leads. However, it should still be coupled enough so that QPs, that populate the subgap states of the SC lead can tunnel coherently between the QD and SC, and as such hybridize with the dot states. The regime where we have both an Andreev dot and subgap states of the SC wire, is for this experiment not explored. Coupling the dot to the SCs wire state enables

[3]We will interchangeably use the term "ABSs in the wire" and "wire states"

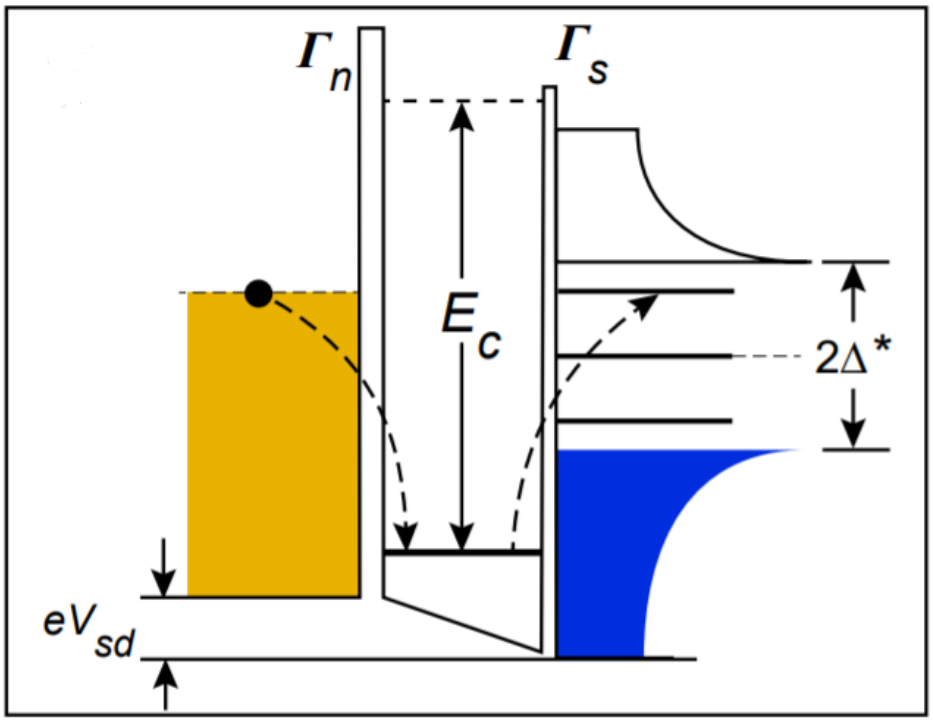

Figure 3.13: *The cotunneling regime in a N-QD-SC system, with a figure from [43]. Bringing the N-lead in resonance, by applying a bias voltage V_{SD}, with the ABS of the SC, leads to an elastic cotunneling process through the dot.*

conductance via virtual processes in the otherwise blockaded Coulomb diamonds. This we refer to as the cotunneling regime, and it is in this regime that we will probe the QD-ABS system (Fig. 3.13). In these more coupled systems (than Sec. 3.2.1) the wave function of the SC ABS leaks into the QD cavity. As the final parts of the LoopQubit experiment, involve hybridizing the two end MZMs of the wire through the QD, to create a system with a sub parity given by the two end MZMs (not by the parity of the individual Majorana nanowires) the cotunneling regime of ABSs and a QD is interesting to explore.

3.3.1 One Superconducting Wire with Andreev Bound States Coupled to a Quantum Dot

Firstly, we turn our attention to a system of one QD and one SC nanowire, by closing the tunnel barrier to the opposite SC nanowire. As in the case of the Andreev dot we highlight the regime, by a small schematic shown in the 2D measurements.

Zero parallel magnetic field: We can first let $B = 0$, and tune the system to be able

to resolve ABS states in the cotunneling regime of the QD. In Fig. 3.14b and Fig. 3.14a, we see that with only one wire open for conductance we are able to hybridize wire states with the levels of the QD. In this regime, we measure that the ABS states of the wire hybridize with the levels of the QD close to the edges of the Coulomb diamond. This verifies that the spectroscopy is not probing sequential tunnelling events; instead, when wire states coincide with the edge of the Coulomb diamond, the energy is perturbed by a change to the chemical potential of the dot, due to energy level hybridization. This is illustrated in the white dotted line of Fig. 3.14b, which is shows strong hybridization.

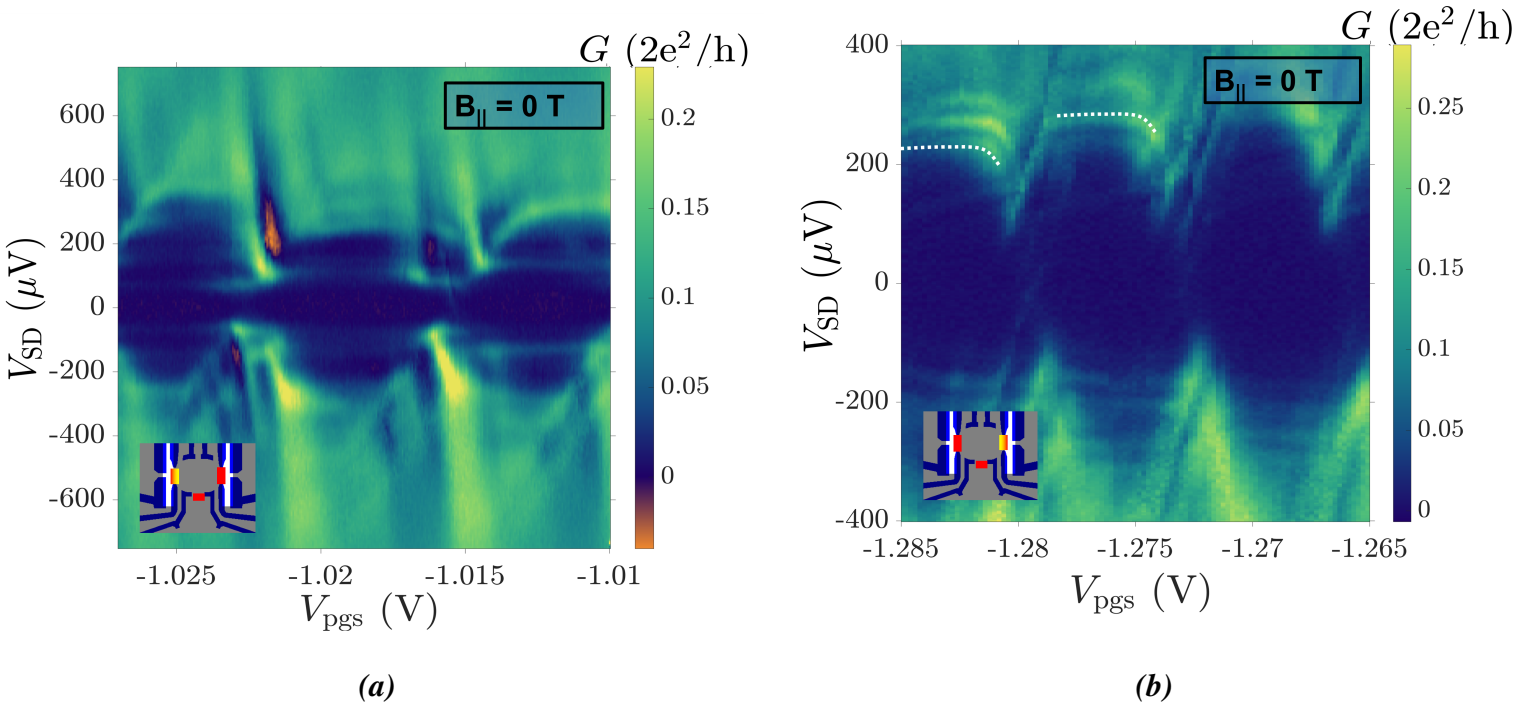

Figure 3.14: *ABS wire states in the cotunneling regime of the dot, where only one SC nanowire is open.* ***a)*** *States in the left wire.* ***b)*** *States in the right wire. Though the spectrum is gapped close to zero bias, the coupling is adequate to see that the wire states in the cotunneling regime, which hybridize with the dot levels: see the white doted lines.*

Finite parallel magnetic field: By applying a parallel field (parallel to the wire), we can move the ABS of the wire to zero via the Zeeman energy, while ensuring that the SC does not turn normal (Fig.3.6 shows that the SC is gapped for $B_{\parallel} < 3$T). Two measurements for high field in the right wire is shown in Fig. 3.15. We observe several crossings at zero energy in Fig. 3.15a, but comparing these crossings to

the zero bias map in 3.15b, we see that the crossing at ~ 1.7 T and ~ 2.7 T, are dot states that move in field. At ~ 0.5 T we see a state approaching zero. We can compensate the field scan, so that we stay within the same Coulomb diamond, as we sweep the parallel magnetic field, we can track ABS's field dependence in the cotunneling regime. This is shown in Fig. 3.16, where we can coalesce ABSs to zero at ~ 600 – 800 mT in the left wire and ~ 500 – 600 mT in the right wire.

In Fig. 3.15b, we also see an hexagonal pattern. This is very much alike to the patterns observed in experiments such as in [62] or would be measured in experiments where a Kondo peak appears at finite magnetic field. However, in this case, the zero energy crossing between the Coulomb resonances depends both on the chemical potential of the dot and the magnetic field applied (see orange and green arrows in Fig. 3.15b).

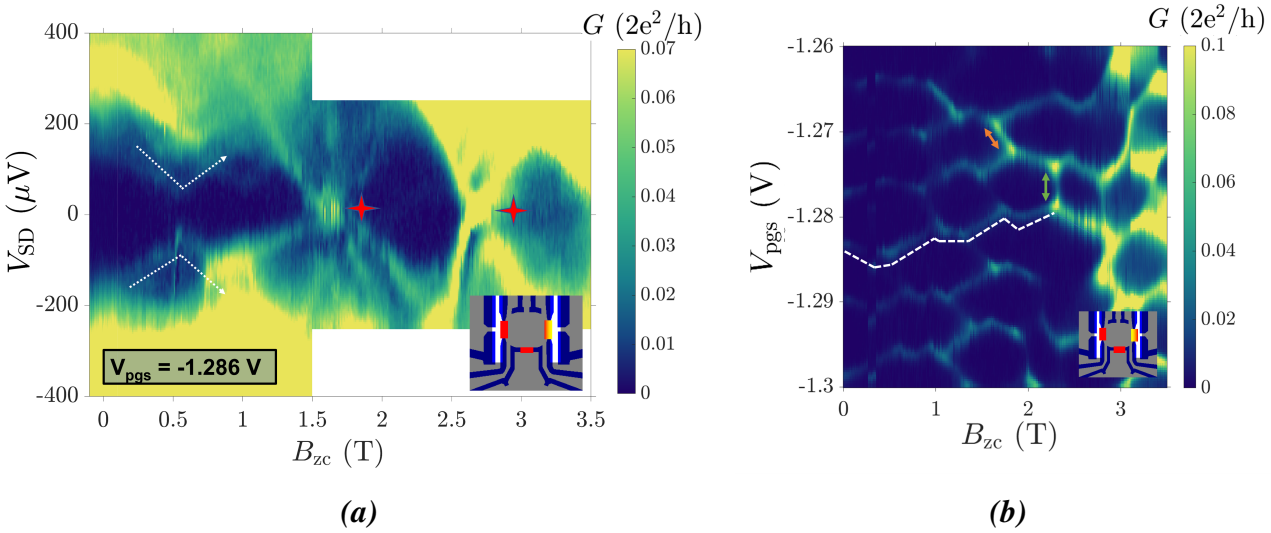

Figure 3.15: *Uncorrected field dependence in the right wire.* ***a)*** *We see both wire states (marked above and below by white dotted arrows) and dot states (marked with a red star to the left) come towards/cross zero energy as a function of $B_{||}$. We have positioned V_{pgs}= −1.286V.* ***b)*** *A zero bias $B_{||}$ vs V_{pgs} map. We see that the dot states strongly depend on magnetic field. We also observe zero bias crossings that connect the Coulomb resonances (orange and green arrow)*

Wire ABS dependence of the wire chemical potential: It is apparent in Fig. 3.16 that wire states coalesce to zero energy at different field values. This can be mitigated by using the wire plungers, as seen in Fig. 3.17. In this measurement staying within a Coulomb blockade and changing the chemical potential of the wire we can move wire states to zero energy.

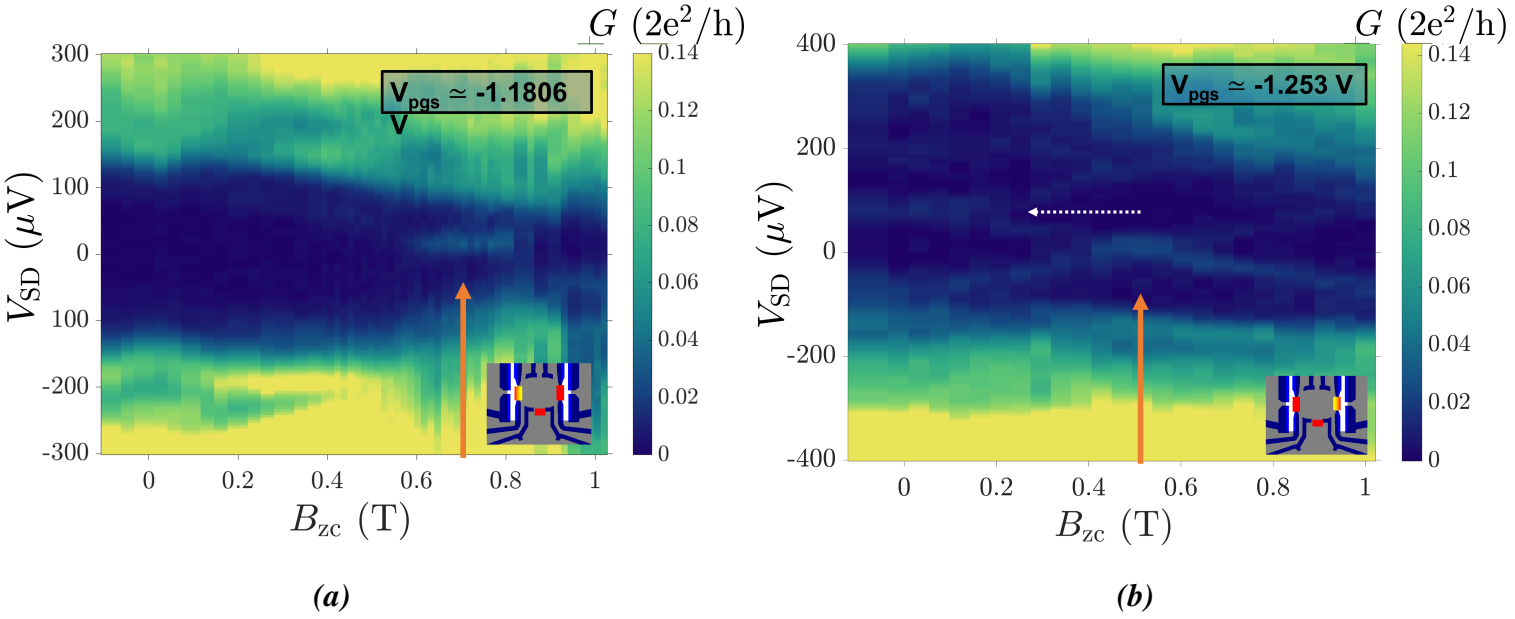

Figure 3.16: *ABS wire states in cotunneling regime parallel field dependence coalescing to zero energy marked by orange arrows.* ***a)*** *In the left wire we coalesce an ABS at* $B_{||} \simeq [600; 800]$ *mT.* ***b)*** *In the right wire we coalesce an ABS at* $B_{||} \simeq [500; 600]$ *mT. In the right wire, we are also able to see the ABS split into its two partner states at* ~ 180 *mT; this is marked with a dotted white arrow.*

Avoided zero energy: When wire states are at zero energy the hybridization with the QD splits the zero energy mode close to the Coulomb resonance. This is expected for local zero energy mode [63]. At this point when $\mu_{\mathrm{ABS,ZB}} \sim \mu_{\mathrm{dot}}(V_{\mathrm{pgs}}, V_{[\mathrm{SD}]} = 0)$, the ABS wave function hybridizes with the dot level, whereby the wave function leaks into the dot. This modifies $k_F L$, the fermi wavevector k_F, and the length of the ABS, L, which changes the energy of the zero mode, to finite energy. It is worth noting that a highly non-local MZM do not exhibit being repelled from zero energy, though short Majorana wires would [63]. A short (or overlapping) pair of MZMs, would however also repel the Coulomb diamond tips, from zero due to SOI (Sec. 1.2.1), which does not happen for local zero modes [63].

It should be noted that the technique of looking for ABS in individual wires, and having the other wire closed, has its drawbacks. Closing off conductance into the other SC nanowire, involves applying a large negative voltage on the gate controlling the tunnel barrier. In this case we need to apply $\lesssim -0.5V$ on the $V_{b,l(r),w,tunnel}$ to close of the left (right) wire. This in turn affects the electron density on the quantum dot, and influences i.e., the normal lead tunnels, $V_{tunnels}$, via crosstalk. The result is that

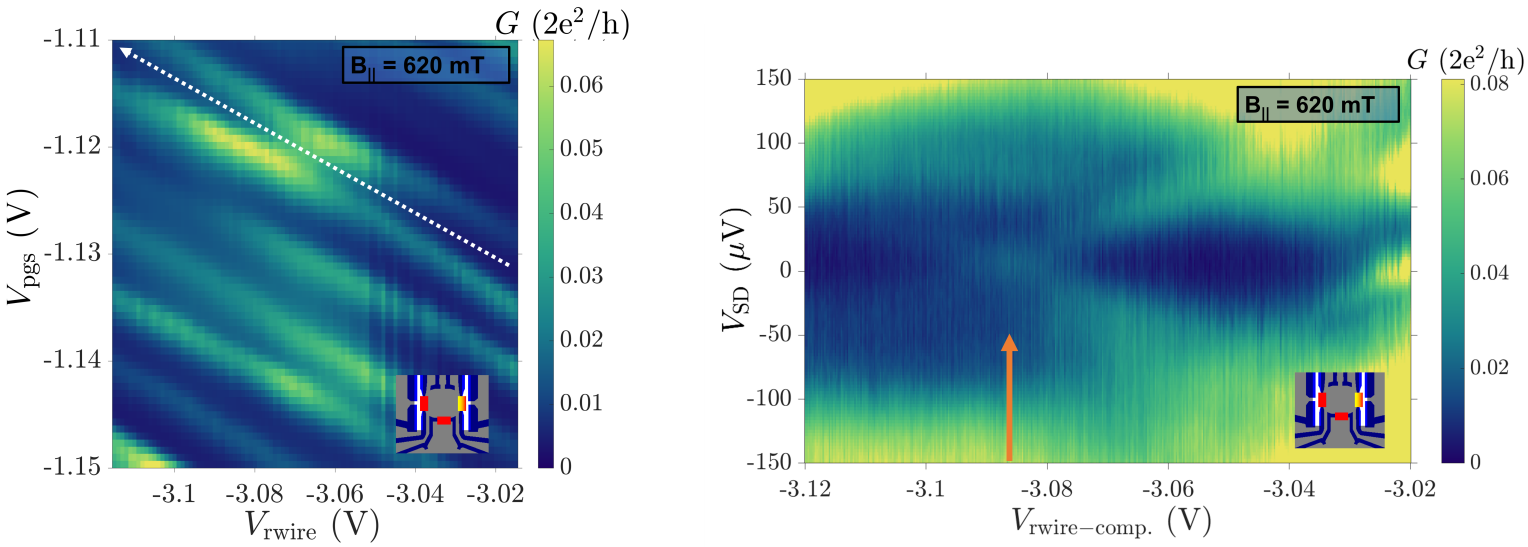

Figure 3.17: *ABS wire plunger dependence.* ***a)*** *By compensating $V_{r,wire}$ gate with the V_{pgs} gates we can probe how the ABS depend on the wire potential, without having dot states cross zero.* ***b)*** *Spectroscopy of the ABS as we change the chemical potential of the wire and stay within a Coulomb blockade, shown by the white dotted line in a), shows that the ABS can be driven to zero energy using the $V_{r,wire}$, strongly indicating that it is indeed a wire state. Similar measurements have been carried out on the left wire state. The compensation is listed in App. B*

finding wire states at zero energy in the left wire and in the right wire sequentially and then opening both at the same time, does not result in having two wire states at zero energy. Generally, we have found the opposite: We see no wire states at

3.3.2 Two Superconducting Wires with Andreev Bound States Coupled to a Quantum Dot

Both wires open: In this measurement scheme we rely on third harmonic measurements, and keep both tunnel barriers open simultaneously. We can change the potential of the wire and thereby the energy of the ABS of individual wires, by changing $V_{l(r),wire}$. We have already, via V_{SD}-$B_{||}$ maps found a suitable magnetic field to see that ABSs go to zero in the range 500 – 700mT. Third harmonic techniques are readily implemented in the LockIn system, SR830. The third harmonic of the signal is the second derivative of the LockIn signal. As we are in the tunnel regime, this means that we can identify peaks and dips at e.g. zero bias, where a peak - most of

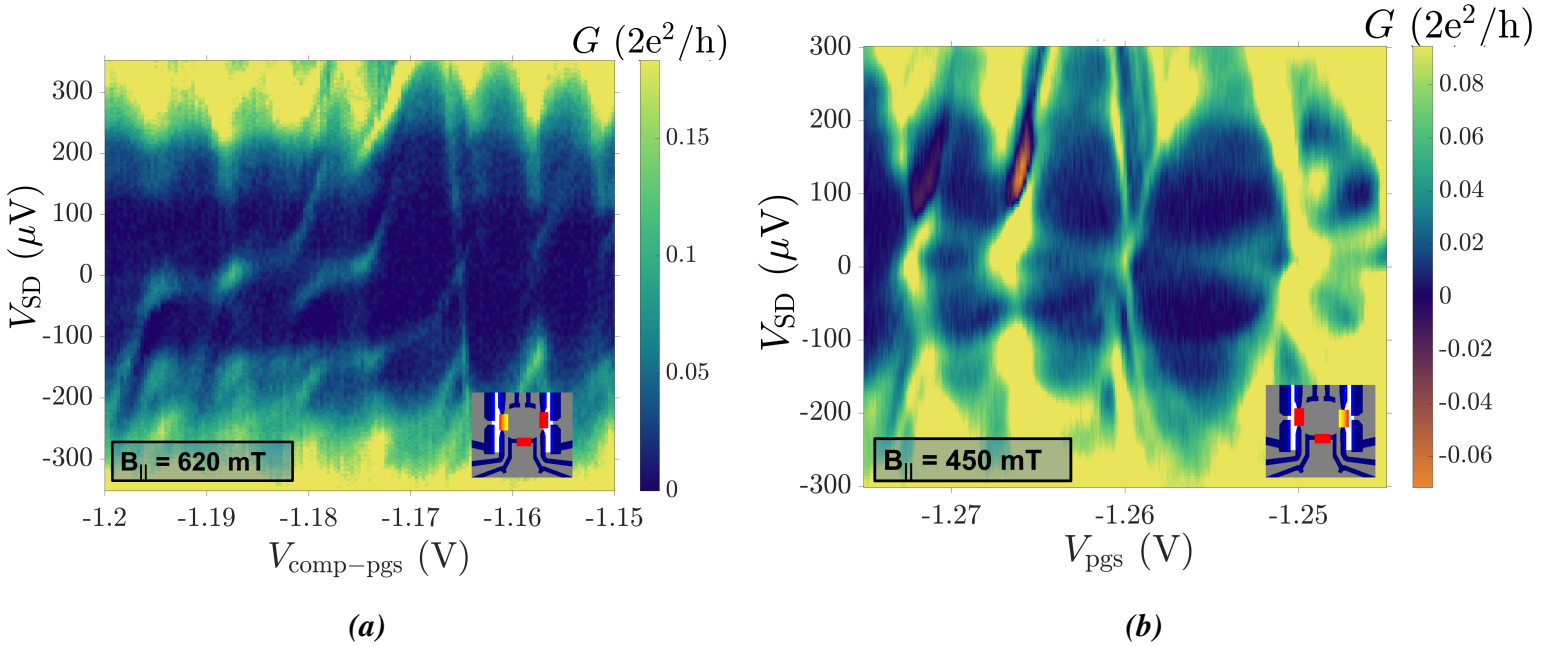

(a) *(b)*

Figure 3.18: *Zero field ABSs in either SC wire.* ***a)*** *We measure that the ABS hybridize with the dot level at the Coulomb resonance. The compensation is listed in App. B.* ***b)*** *A much stronger hybridization is measured in the right wire. We believe the reason that the right wire in general couples more strongly to the dot is due to a cutter dot located in the left side of the device. The cutter dot is an accidentally formed dot, that proved impossible to remove. Therefore, we found a regime where we knew that it was in a cotunneling regime. Having the dot in the cotunneling regime, we can view it as an additional tunnel barrier, which necessarily also impacts the coupling.*

the time - corresponds to discrete states, see Fig. 3.19.

Hybridizing Two Andreev Bound States Through a Quantum Dot

The theoretical investigation done on a more exotic system, a dot coupled to one or two MZMs, is a surprisingly well explored phenomena. For the theoretical rigour of ABSs hybridizing with a QD we lean on work done previously by E. Prada et al. [63], who treats semi-non-local MBS, and trivial local zero modes in a SC nanowire which is coupled to a QD. This is used to explain the experimental measurements by M. T. Deng et al. [43]. There are some parallels between ABSs and MBSs. The major difference here is that the ABS is one extended or localized states, where we cannot treat its Majorana operators as constituting individual wave functions, that may or may not have an overlap (as in the case of a topologically non-trivial MZM), but instead as one fermionic mode.

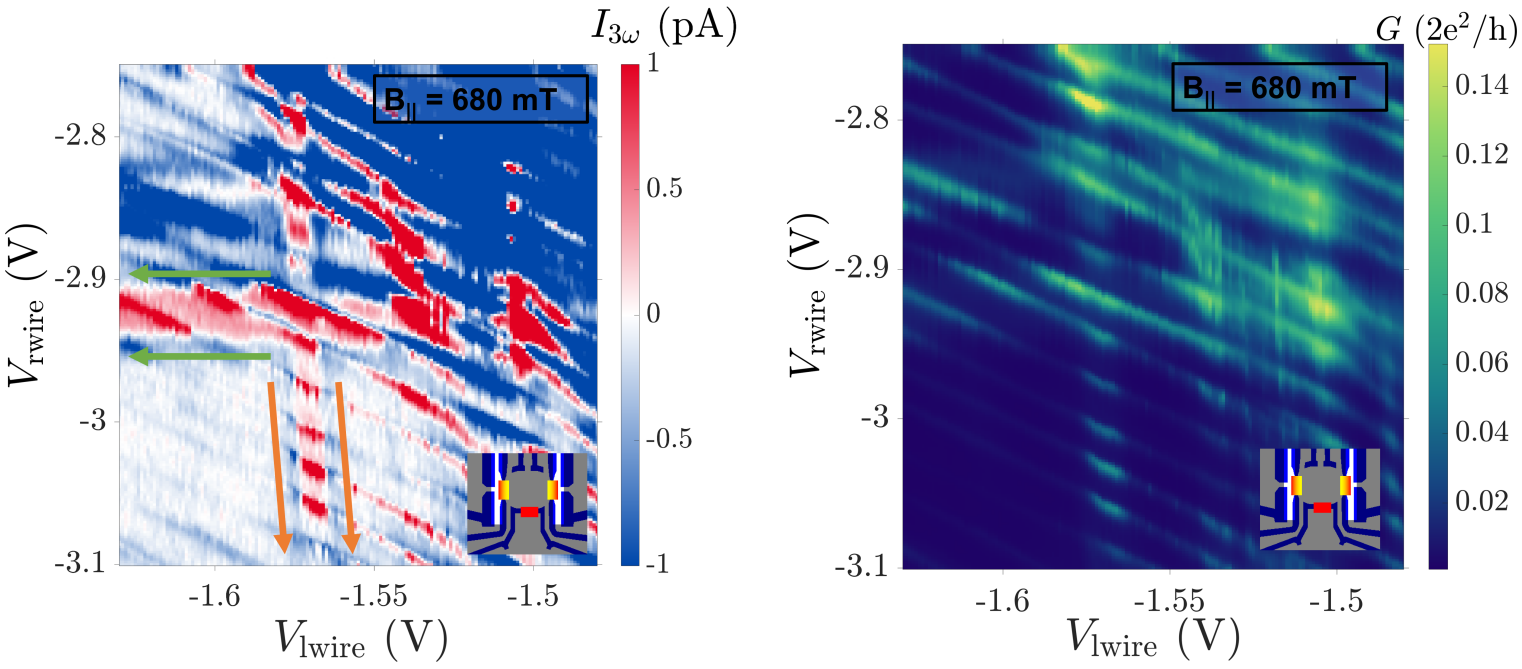

(a) ***(b)***

Figure 3.19: ***a)*** *Third harmonic signal, negative current corresponds to a dip in conductance around zero bias, while positive current corresponds to a peak around zero bias.* ***b)*** *The corresponding conductance is simultaneously measured. We can see that there are two features that independently couples to either wire, and are very weakly coupled to the other wire. The right (left) wire feature is marked within the green (orange) arrows.*

Only One ABS at Zero Energy - Two Superconducting Leads Connected to a Quantum Dot

We have also measured a regime where there are only ZB states in one wire, though conductance into the other SC lead is still possible. We observe in Fig. 3.22 that even with no corresponding ZB state in the left wire, the zero energy ABS of the right wire is still modulated as we apply a perpendicular magnetic field.

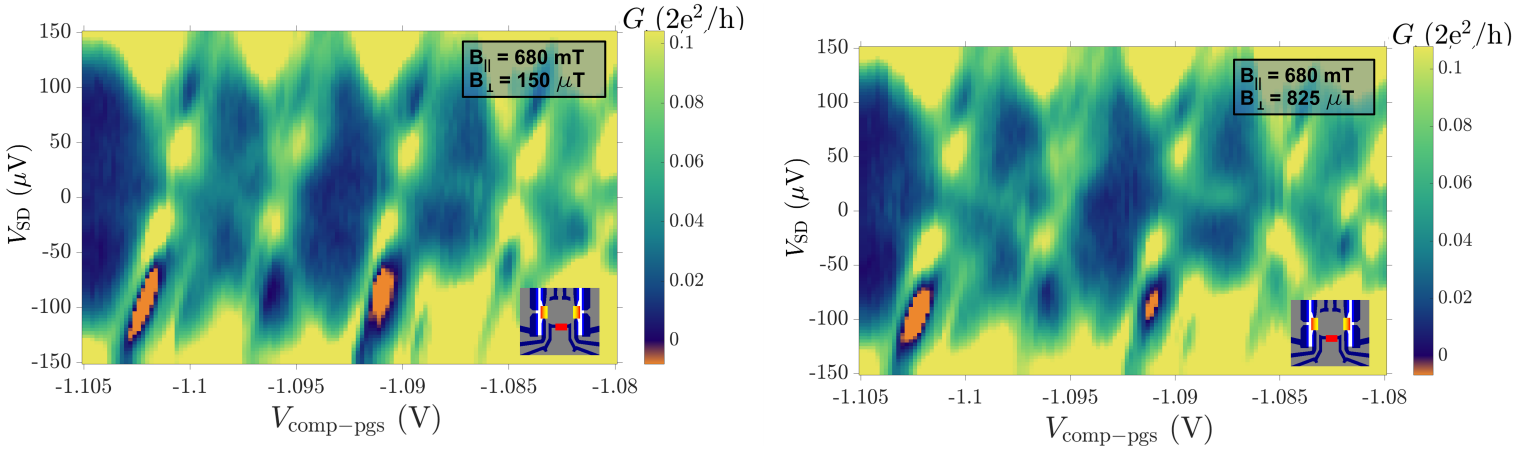

(a) *(b)*

Figure 3.20: *Two wire states in the cotunneling regime are brought to zero bias. The phase difference of the superconductors is: $\delta\phi \simeq \pi$. No apparent difference can be resolve in spectroscopy by changing the chemical potential of the dot. Compensations of dot plunger are listed in App. B*

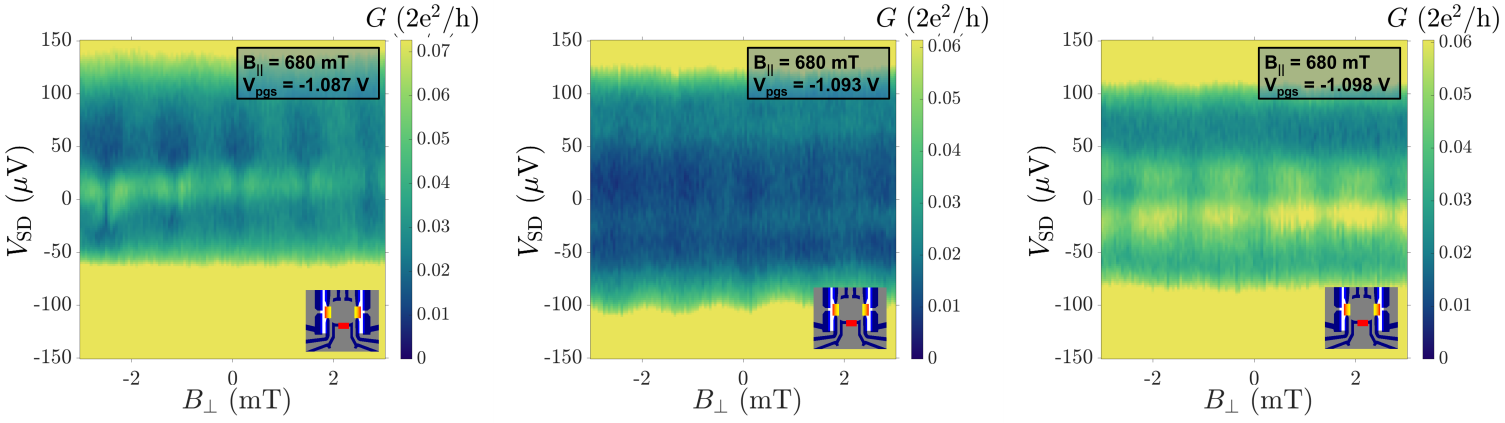

(a) *(b)* *(c)*

Figure 3.21: *The two wire states we believe to be at zero bias in Fig. 3.20, are in spec here we probe the phase dependence for different V_{pgs}: **a)** $V_{comp\text{-}pgs} = -1.087V$, **b)** $V_{comp\text{-}pgs} = -1.093V$, and **c)** $V_{comp\text{-}pgs} = -1.097V$. Though no phase dependence were visible in Fig. 3.20, the conductance and energy of the ABSs are clearly modulated by the phase difference of the two SC wires.*

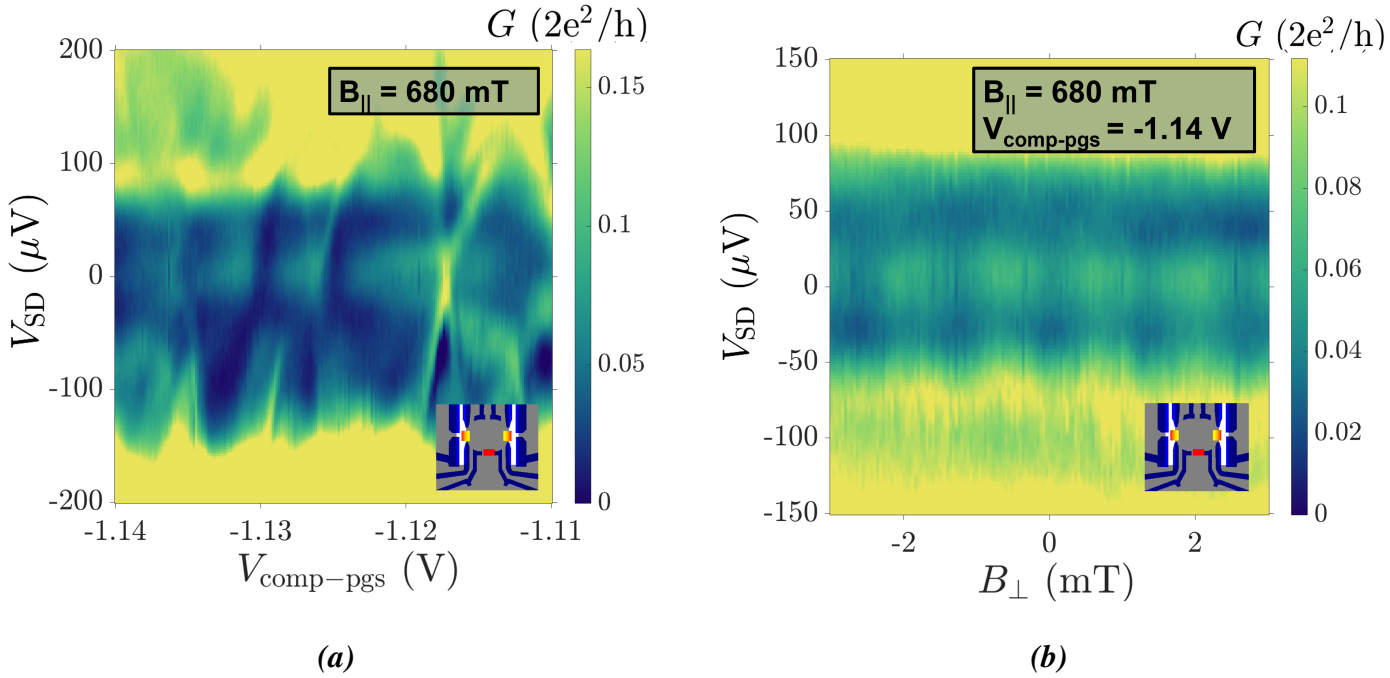

Figure 3.22: *One wire state in the right wire at ZB. We have applied a voltage to the $V_{l,wire}$ gate to that there are no left wire states.* ***a)*** *Spectroscopy shows hybridization with the QD.* ***b)*** *Phase dependence of the right wire state, taken at $V_{comp\text{-}pgs} = -1.114V$. Even with no states in the left wire we still observe that the peak is modulated as we apply phase difference between the two SC nanowires. Compensation listed in App. B*

3.4 The Zero Field Feature

A feature we have found in these devices, are what we have dubbed a *zero field feature*[4] (ZFF). At true zero perpendicular field, it can be seen in spectroscopy of i.e. Fig. 3.24, that several more discrete state are visible in cotunneling QD spectroscopy. We can also see in Fig. 3.23, that this is true both on and off the Coulomb resonance. The full width of this feature appears to be on the order of $\sim 400\mu$T. Based on the

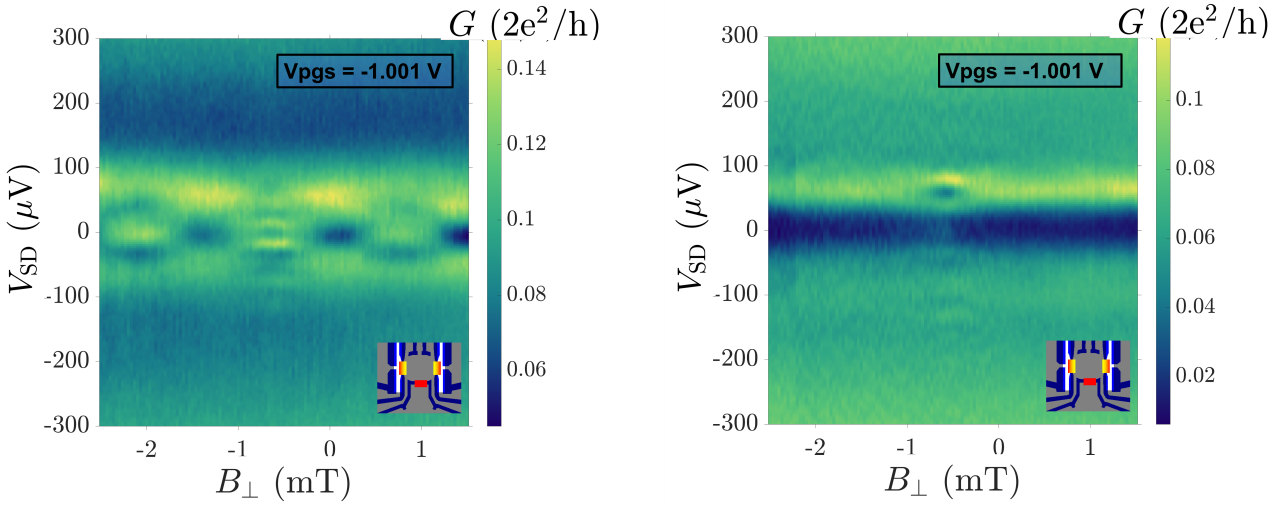

(a) *on resonance with CB* ***(b)*** *off resonance with CB*

Figure 3.23: *Spectroscopy in the cotunneling regime shows the wire states are broadened as we move away from true zero magnetic field, by applying a perpendicular field.* ***a)*** *Cotunneling spectroscopy at* $B_\perp = 80\ \mu T$. ***b)*** *Cotunneling spectroscopy as we apply* 2π *phase difference to the SCs, corresponding to* $B_\perp = 1.48\ mT$

measurement of Fig. 3.24 we postulate that it is not the emergence of more states, but we see that at a finite perpendicular field, the broadening of the states increases. Broadening of the states suggests that after applying 200μT, the lifetime, associated to these, would have decreased drastically to account for the broadening. We have found that this is not physics originating from the loop of the experiment, as closing one wire we still achieve the same feature. If the phenomenon is coupled to the threading a magnetic quantum flux, $\Phi_0 = h/(2e)$, for example as a feature that is connected to weak anti localization, the area would correspond to $\sim 10.3\mu m^2$. This should be compared to the area of $\sim 1.65\mu m^2$ which the loop of the experiment

[4]This feature has been measured in several generations of the design, measured on different wafers - though all in similar heterostructures.

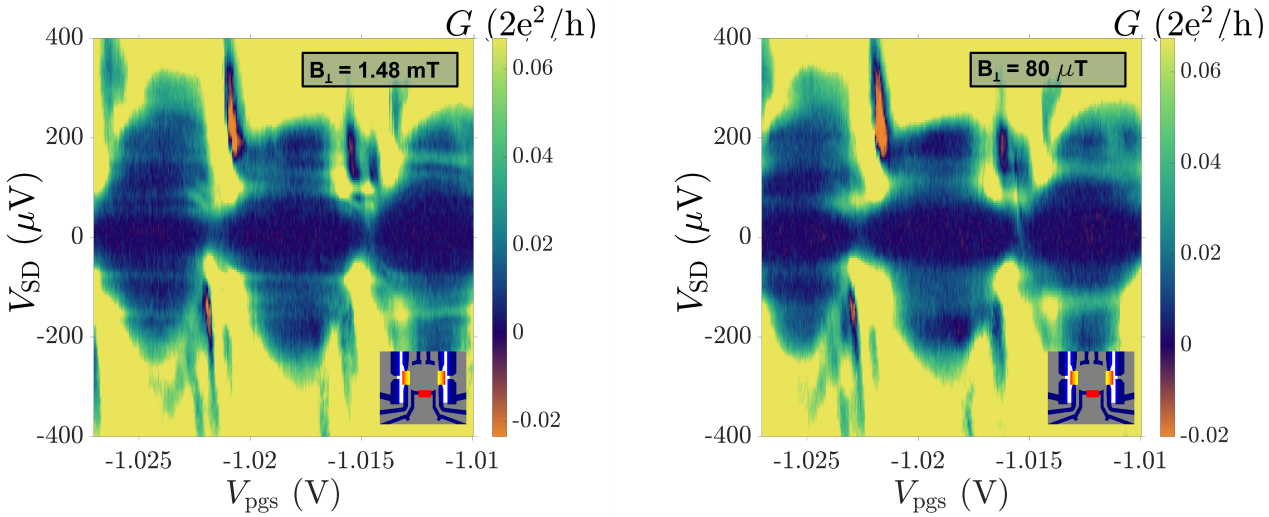

Figure 3.24: *A cotunneling experiment:* ***a)*** *Taken at the ZFF.* ***b)*** *Taken at phase* $\varphi = 2\pi$ *away from the ZFF.*

encompasses. What we see in Fig. 3.21, is that the feature does not appear in a phase map, as the parallel field for these measurements are at 680 mT. We have in previous devices seen that this feature in $B_{||}$ persists for $B_{||} \sim 60$mT.

CHAPTER 4

Wrapping up

4.1 Discussion and Conclusion

We have explored the different regimes, accessible to us, defined by the coupling between SC leads and a QD. The different regimes are illustrated in Fig. 4.1

The Andreev Dot

We detected a phase dependent AD state, though the AD phenomena in general have been difficult to observe in this device. However, we were unable to prove a 0-π JJ phase transition as we changed the chemical potential of the AD, thereby loading electrons onto the dot. What we might associate with an even occupational state had no spectroscopic phase dependence. Furthermore, we do not have any way of exploring the $\frac{E_C}{\Delta} < 1$ regime, which is discussed in [61]: the superconducting gap can only be decreased with parallel field, and we have observed in spectroscopy that the charging energy does not depend on the voltage applied to V_{pgs} gates, in the range we have explored. Only a few examples fine-tuned cases did we see signatures of a singlet to doublet transition as we change the occupation of the QD, see Fig. 3.11. As such we were unable in this device to show the different phase dependence that a doublet and a singlet ground state has. This might be a result of the mesoscopic size of the QD ($\sim 750 \times 350\,\mathrm{nm}^2$). Though we do see phase dependence, the separation between the SC leads could be so long that the phase dependence is slightly less than expected, meaning the doublet state does not close completely as it should. The size of the dot could also mean that the spin of the QD might be $\mathbf{S} > 1/2$: we can sequentially load

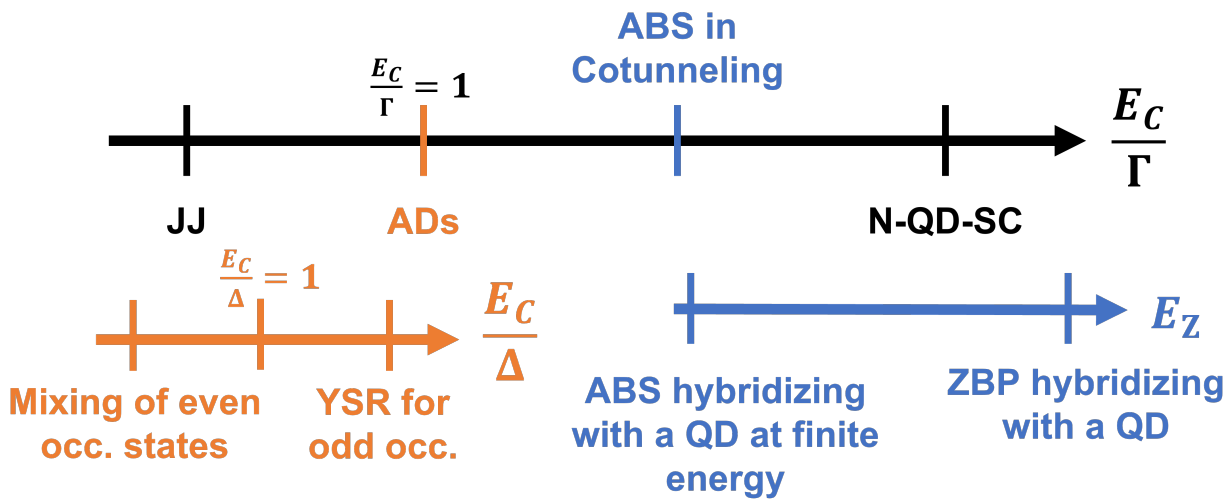

Figure 4.1: *Regimes of a SC-QD-SC system*

several electrons with the same spin. Due to the size of the QD, we are able to fill higher energy orbitals of the dot, instead of filling the orbitals sequentially, which would fix the total spin in configurations $S_{tot} = \{0, 1/2\}$; in these systems the ground state of many-electron QDs will follow Hund's rules [64], of filling the orbitals of the quantum dot. Asymmetry in the tunnel barriers can also lead to a drastically decreased phase dependence [57], which has highly likely happened in our device, due to resonances in the tunnel barrier. If a more controllable AD is formed, one could also consider turning on parallel magnetic field. This should in theory induce 0 to π JJ transitions and be able to form 0' or π' JJs, where there are two ground state minima as a function of the superconducting phase. Furthermore, it should be noted that for large coupling, we can experience difficulty in observing phase dependent 0- or π-JJs because $T_K > \Delta$; the Kondo effect dominates, the spin is screened creating a spin singlet state, and a doublet state is not formed. The signature is that a Kondo peak is formed within the Coulomb diamond at zero energy [65].

Hybridization Between a Quantum Dot and One or Two Fermionic Zero Energy States

By decoupling the QD sufficiently, we have been able to measure ABS formed in the SC wire in the cotunneling regime of the dot. We have had great success finding regimes where the energy level of a QD hybridizes with wire states from one wire at zero applied magnetic field. We have demonstrated that as the energy of the Andreev bound state align with the QD's energy level, the two levels can hybridize. We

have also been able to track an ABS in either wire as it coalesces to zero energy, in the cotunneling regime of the dot. We have seen that at zero energy, we can observe that the hybridization, as predicted [63], pushes the ABS to a finite energy as the wavefunction is able to inhabit the QD cavity. The spectroscopy of wire states with only one wire has generally produced better spectroscopic results, than when both SC nanowires was open. We hypothesize that the optimal gate regime for finding right, and left wire states differ too much. The optimal gate configuration for simultaneously seeing ABS wire states in both wires are drastically different from the optimal configuration of the isolated wires.

When we open both wires simultaneously, we have seen that we can independently move ABS to zero energy by changing the voltage on the wire plunger gates $V_{l/r,wire}$, in a third harmonic measurement. In spectroscopy it has proven to be difficult measure and we have seen that the wire states in the cotunneling are rather broad. In conjunction, we have also seen that going between the regimes (N-QD-SC (weakly coupled), wire ABSs visible in cotunneling spectroscopy from one wire, and two ABSs from two wires at zero energy visible in cotunneling spectroscopy) changes the measured charging energy of the QD dramatically: going from respectively $E_C \sim 600$ μeV $\rightarrow E_C \sim 400$ μeV $\rightarrow E_C \sim 150$ μeV. We believe that the change originates from the fact that the wave function of the electron density in QD becomes less laterally restricted, as we open the barriers between the cavity and into the SC wires. We have also shown that the wire states show phase dependence, both if an ABS is present at the same energy in the other wire or not. We attribute the fact that the ABSs are phase dependent in the latter case, because AR on the SC with no wire states, will experience the change in the phase of the superconducting gap, as we apply a perpendicular magnetic field. It can therefore be argued that coherent transport into both wires is possible, which would mean that the ABSs of the two wires also couple to each other. However, in this scheme we have no way of checking whether this is true. Because we always see both splitting of the zero-energy state and phase dependence the regime with ABSs it is in some respects more complex than the MZM scheme; only when two MZMs are present in either wire do we find a splitting at zero energy for these non-local bound states. Furthermore, in theory, this might prove a very good way of finding whether we have created long or short Majorana nanowire (defined by the topological coherence length), as there are few ways in these systems to measure the topological coherence length; only semi-non-local MZMs in a single

wire will exhibit a zero energy splitting.

The Zero Field Feature

We are very certain that the phenomena at true zero magnetic field is physics originating from the normal leads of the experiment. Weak anti localization leads to a resistance in the normal leads, which has an impact on the thermalization of the charge carriers. However, this should be checked thoroughly i.e., by measuring the electron temperature in a CB regime at and away from the ZFF.

4.2 Outlook

The Quantum Point Contact Gates

The control of the SC-QD tunnel barrier is an integral part of, not just the phenomena we have explored, but also in general the measurement-based TQC scheme [4]. An optimal control of the QPC gates are as such important. Therefore, it might be interesting to see what optimization we can do. It might be, that a multi-layer gate approach needs to be taken, to gain better control of the barriers. The tunnel barriers in this experiment is dubbed *side probes* as they allow for transport to enter from the side of the SC nanowire. The point is that MZM are $k = 0$ states. If we use electrons with a finite parallel (to the wire) momentum, $k_{\parallel}$, they couple stronger to modes in the nanowire with a finite $k_{\parallel}$. Here we might add that ABSs have a finite momentum on the order of the Fermi momentum of the SC, as their dispersion are alike to the SC dispersion in Fig. 1.1b, which at zero energy for $\Delta = 0$ is $k \sim k_F$.

Zero Bias Peaks at Higher Parallel Magnetic Field

The main goal of the experiment is the readout of parity of MBSs in the nanowires. In the experiments of this thesis the ZBP have been trivial, but by going to higher magnetic fields we could be able to induce a topological phase transition. If the MBSs in this topologically non-trivial phase are highly non-local, they should not split at zero energy as they hybridize with the dot level, though they should repel the dot energy level from zero as opposed to ABSs. Only when two MBSs from either end of two SC nanowires hybridize with each other should we see a splitting (due to the wave function overlap). In this way, the cotunneling experiment with MBS

are more conclusive, with respect to whether pairs of zero energy wire states can hybridize across quantum dot, than the corresponding zero energy ABS experiment. If we find what we believe to be MBSs in both wires and see hybridization, we would want to measure how electrons jump on and off the MZMs in both wire ends from and to the QD, using a sensor dot. Due to the very short time scales involved, this needs to be done with radio frequency (RF) measurement.

CHAPTER 5

The Andreev Billiard Experiment - Quantum Chaos Meets Particle-Hole Symmetry

The problem that we will cover in this section is the Andreev Billiard, which due to it being a standalone experiment, which is not connected to that of superconducting nanowires' ABSs. Though the project is still in a start-up phase, the physics are interesting and deserves a discussion, on the basis of the preliminary measurements we have done. As a remark to this: few experiments have been done on this crossroad between quantum chaos and superconductivity, especially in hybrid SC-SM materials where the chaotic cavity is laterally defined. The phenomena of quantum chaos is solved on the basis of random matrix theory (RMT), a mathematical theory introduced by J. Wishart in 1924 [66], treating covariance matrices in multivariate theory, and extended to physics in the 1950's by physicist Eugene Wigner [67], and developed more fully by Wigner, Mehta, Gaudin and Dyson in the 1960s.

5.1 Theory

The introduction of random matrix theory into physics, was first done by E. Wigner as a way to describe the scattering resonances observed in nuclear reactions of large/heavy atom's [67]. The levels in these atoms depend on the strong interactions between the particles within, which is not a difficult problem in heavy atoms. He proposed that even though the interactions are random the statistics follow from

the energy eigenvalues of the random matrices that describe the Hamiltonian of the nuclei. These in turn, should be drawn from an ensemble that depends on the symmetries of the system. In 2DEGs, the same thought process can be used to describe mesoscopic systems. Here quantum transport is a coherent process, but the systems are so large that a statistical treatment of transport is preferred in many cases [68]. Instead of nuclei potentials, the electrostatic potential $V(x)$ - and as such the Hamiltonian matrices or scattering matrices[1] - is a random parameter, that depend on the disorder within the system or disorder in the boundaries of the system[2], and is drawn from an ensemble [69], with a probability distribution given by,

$$P(V) = c \exp(\mathcal{B} \operatorname{Tr} V(x)), \tag{5.1.1}$$

where c is a normalization factor and $\mathcal{B}$ defines the symmetry of the system. For $V(x) \propto H^2$ they are denoted as Gaussian ensembles; these are the ones that describe most systems. The universality of this description of quantum transport is highly attractive. We treat the configuration within the system as a black box and simply approach the problem only knowing the symmetries that govern the physics of the system. Ten universality classes exist in the Gaussian case which each are defined by the presence or absence of anti-unitary matrices that commute with the Hamiltonian [69]; this is colloquially known as the *tenfold way*. They follow from unitary or anti-unitary matrices that either commute or anti-commute with the Hamiltonian, H (Fig. 5.1). The presence of the time reversal is given by $H\mathcal{T} = \mathcal{T}H$, while the introduction of superconductivity means that $HC = -CH$. The ensembles are defined by the presence of the commutation relations and whether $C^2 = \pm 1$ and $\mathcal{T}^2 = \pm 1$. Lastly, the system can also have a chiral symmetry defined by whether $C\mathcal{T}H = -HC\mathcal{T}$. These are the symmetries that the system can exhibit, and are summarized in Fig. 5.1. The probability distribution of energies for systems with particle-hole symmetry (not A, AI, and AII) and AIII, is given by [69],

$$P(\{E_n\}) \propto \prod_{i<j} |E_i^2 - E_j^2|^{2\beta_E} \times \prod_k |E_k|^{\alpha_E + \nu\beta_E} \exp\left(\frac{-\pi^2 \beta_E d_E E_k^2}{4\mathcal{N}\delta_0}\right) \tag{5.1.2}$$

[1]We will focus on the Hamiltonian - The statistics in this case, will allow us to probe the energy level ensembles. In our systems, this is readily done with a tunnel barrier, where we spectroscopically resolve the energy levels. However, transmission through chaotic systems follows the same statistics, and can in principle also allow us to probe the universality classes.

[2]Clean systems can however also be chaotic. However, here chaos is introduced because of the non-integrable boundary i.e. Sinai billiards

	D	BDI	DIII	C	CI	CII	A	AI	AII	AIII
$H\mathcal{C} = -\mathcal{C}H, \mathcal{C}^2 =$	$+1$	$+1$	$+1$	-1	-1	-1	$\times$	$\times$	$\times$	$\times$
$H\mathcal{T} = \mathcal{T}H, \mathcal{T}^2 =$	$\times$	$+1$	-1	$\times$	$+1$	-1	$\times$	$+1$	-1	$\times$
$H\mathcal{C}\mathcal{T} = -\mathcal{C}\mathcal{T}H$	$\times$	✓	✓	$\times$	✓	✓	$\times$	$\times$	$\times$	✓
ν	0,1	0,1,2,3,...	0,1	0	0	0,1,2,3,...	0	0	0	0,1,2,3,...
d_E	1	1	2	1	1	2	1	1	2	1
α_E	0	0	1	2	1	3	0	0	0	1
β_E	2	1	4	2	1	4	2	1	4	2

Figure 5.1: *The ten universality classes constituting the tenfold way [69]. $\mathcal{C}$ is the charge conjugation operator and $\mathcal{T}$ is the time-reversal operator. Crosses and checks marks whether the symmetry is present in the class or not. $+1(-1)$ marks whether the anti-unitary operators square to one. ν is the number of d_E-fold topological zero modes. α_E and β_E are the repulsion coefficients.*

Here β_E acts as a inverse temperature, that repels level E_i from $\pm E_j$ in the term $|E_i^2 - E_j^2|^{2\beta_E} = (E_i - E_j)|^{2\beta_E}(E_i + E_j)|^{2\beta_E}$, repels the states from the possible zero energy state in the term $|E_k|^{\nu\beta_E}$, and restricts levels to not increase towards infinity in the exponential term. The α_E parameter enters due to particle-symmetry (except in the case for AIII), and repels the particle states from their hole counterparts [68, 69]. The mathematics and theoretical physics of random matrix theory is comprehensive and has been explored extensively before. As such I will refer to more extensive details in more in-depth reports done by i.e. [68–70, 72, 73]

5.2 Preliminary Results

We can measure the density of states in the device architecture shown in Fig. 5.2. This device is based on the proposal by S. Plugge [42], which he names a Majorana Box Qubit (MBQ). In this device, we will let the mesoscopic quantum dot, at the end of the SC nanowires, play the role of the Andreev billiard [70]. Laterally gate defined cavities will be an extremely powerful tool to explore the statistics of universality classes. As discussed in Sec. 5.1, the statistics of the cavity is independent of its shape, only the symmetries of the systems are important. However, by changing the shape a different energy configuration can be reached. With the means of adding more measurements to the statistical data analysis, we can with a much greater accuracy determine the ensemble to which the system belongs. The Andreev billiard [70] is shown in the inset of Fig. 5.2

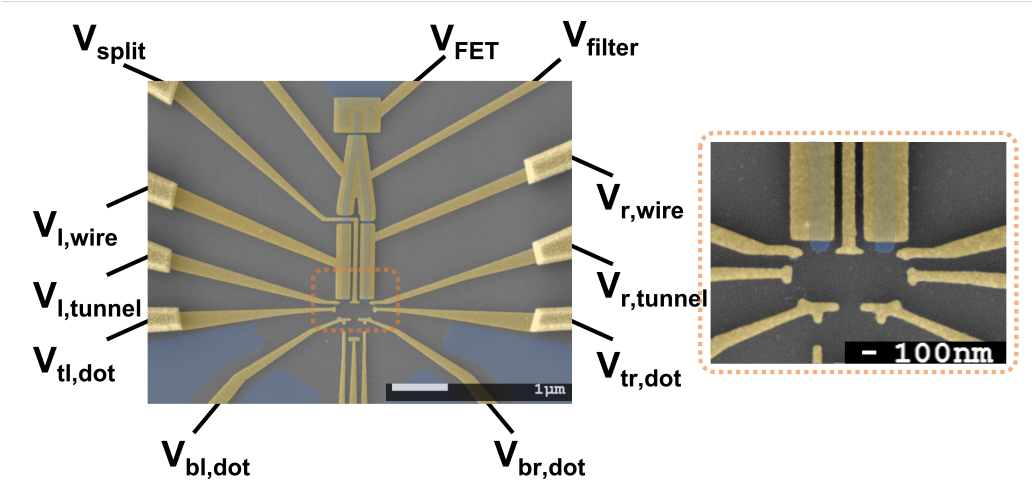

Figure 5.2: *False colour SEM of the MBQ design, with gate abbreviations. Gates are coloured yellow, the SM is grey, and the aluminium is coloured blue. Shown in the orange box is a zoom-in of the Andreev billiard, which has three QPCs between the normal leads and the billiard, and QPCs into the two superconducting nanowires.*

We define the superconducting wires and quantum dot by energizing the electrostatic gates of the device. When we observe a system that exhibits the phase dependence we expect from the loop (1.7 mT), we probe the system. This is done by resolving the LDOS of the system using spectroscopy. After measuring the phase dependence of the device we find the same ZFF described in Sec. 3.4. In Fig. 5.3 we show the spectroscopy of the Andreev billiard, at the ZFF, as we plunger the dot using the gate $V_{tr,dot}$ for four configuration of $V_{tl,dot} = [-1.5, -1.75, -2.0, -2.25]$ V. As we apply a voltage to these gates, we change the shape of the cavity; in theory, this means that we are probing different configurations within the same ensemble. We use a Matlab peak finder algorithm [71] to automatically find states in spectroscopy. The energies of these states are recorded, and the spacing between neighbouring energies are calculated. As the energy follows the RMT of the given ensemble, so will the level spacing. We are interested in the level spacing to more readily compare the result with theory [70, 72]. We compare the distribution of measured level spacings,

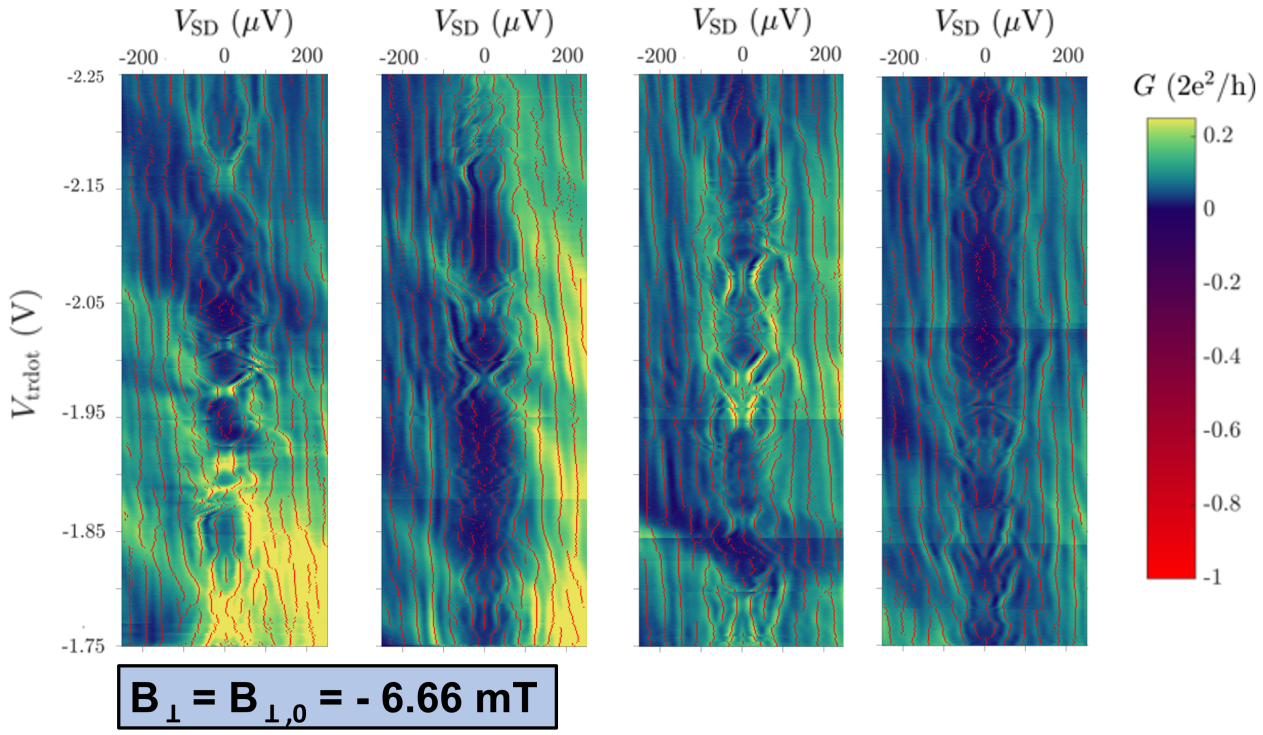

Figure 5.3: *In spectroscopy we observe discrete levels that change as the electrostatic configuration within the Andreev billiard is changed by the changing gate voltages. From left to right the $V_{tl,dot}$= $[-1.5, -1.75, -2.0, -2.25]$ V. The peak finding algorithm adapted from [71], finds discrete states given by the red marks, the conductance values of which, we manually set to $G = -G_0$ for clarity.*

with that of other ensembles [72] (here shown as integrated probability)

$$P_{\mathrm{GOE,int}}(\delta) = 1 - \exp\left(-\frac{\pi\delta^2}{4}\right) \tag{5.2.1}$$

$$P_{\mathrm{GUE,int}}(\delta) = -\frac{4\delta}{\pi}\exp\left(-\frac{4\delta}{\pi}\right) + \mathrm{erf}\left(\frac{2\delta}{\sqrt{\pi}}\right) \tag{5.2.2}$$

$$P_{\mathrm{GSE,int}}(\delta) = -\frac{16\delta(128\delta^2+27\pi)}{81\pi^2}\exp\left(-\frac{64\delta^2}{9\pi}\right) + \mathrm{erf}\left(\frac{8\delta}{3\sqrt{\pi}}\right) \tag{5.2.3}$$

$$P_{\mathrm{Poisson,int}}(\delta) = 1 - \cosh(\delta) + \sinh(\delta) \tag{5.2.4}$$

$$P_{\mathrm{WP,int}}(\delta) = \exp(-2\delta)(-1 + \exp(2\delta) - 2\delta) \tag{5.2.5}$$

We see that the level spacings, do not follow any of the ensembles described by the Wigner-Dyson theory or by the hybrid Wigner-Poisson distribution from [72] (Fig. 5.4). Furthermore, we also try to resolve spectroscopy using the $V_{tl,dot}$ gate (Fig. 5.5). We change the gate $V_{tl,dot}$ smoothly and $V_{tr,dot}$ in four steps of $V_{tr,dot}$ = $[-1.5, -1.75, -2.0, -2.25]$ V. The voltage configurations of the other gates are

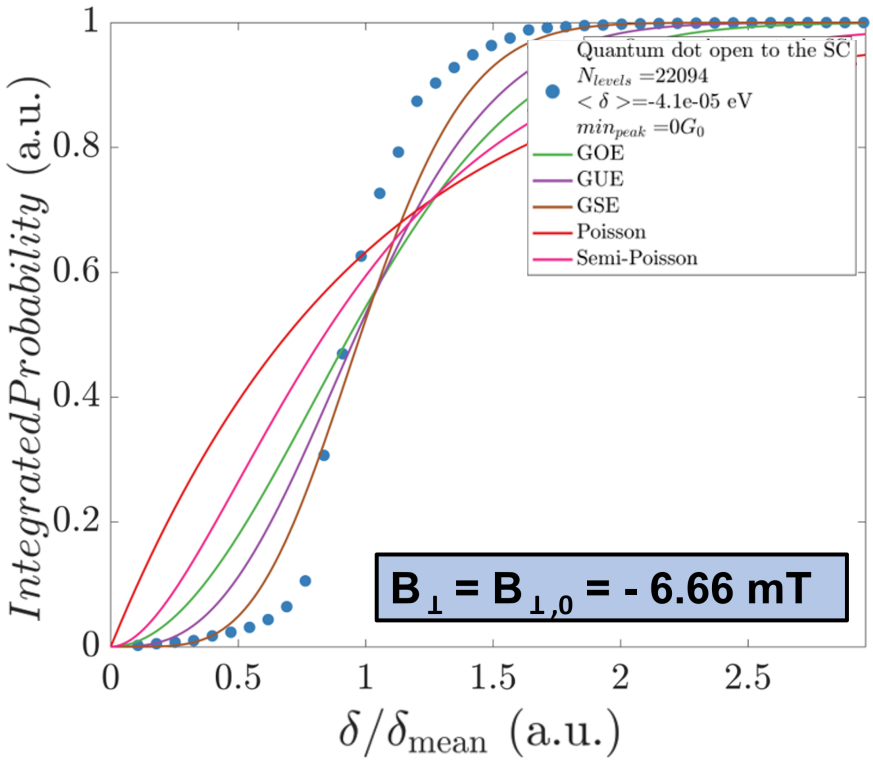

Figure 5.4: *Statistics of Fig. 5.3. We find the level spacing of all the positive energy states, below the superconducting gap Δ, and plot them in an integrated probability distribution function (PDF). This is compared to integrated PDF of the Wigner-Dyson ensembles (GOE, GUE, and GSE for respectively the orthogonal, unitary and symplectic ensembles), corresponding to A, AI, and AII in Fig. 5.1. Also we compare it to the Poisson and Wigner-Poisson distributions of [72]*

changed slightly to accommodate this change compared to Fig. 5.3 and Fig. 5.4. The result of the integrated probability density is shown in Fig. 5.5 and an excerpt of the spectroscopy using $V_{tl,dot}$ with $V_{tr,dot} = -1.5$ V. Here it seems as though the statistics resemble that of the GSE (or AII in Fig. 5.1)

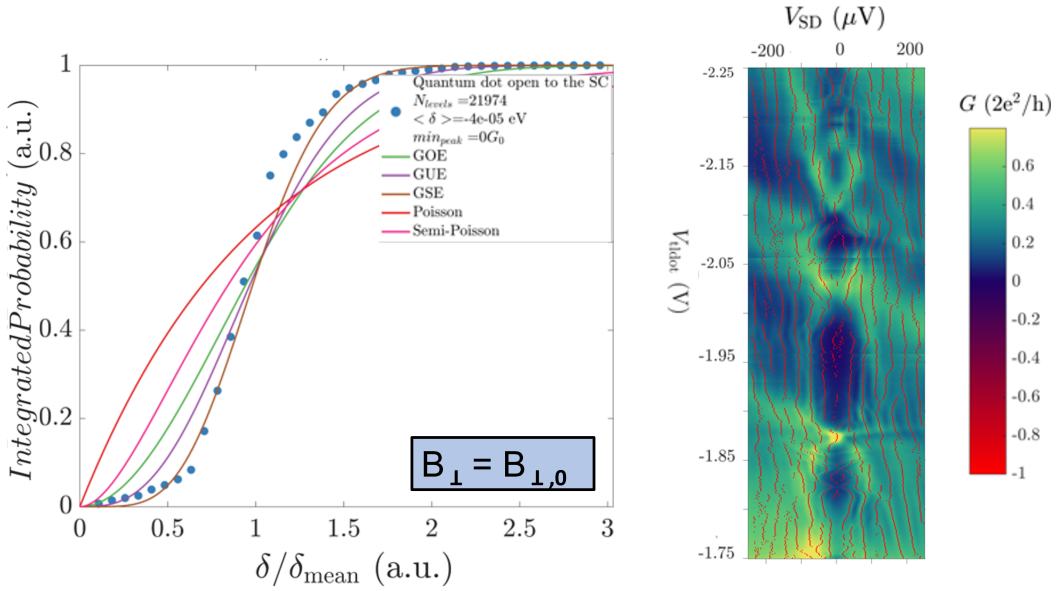

Figure 5.5: The left graph: *shows the integrated probability density of level spacings measured in spectroscopy. It seems to follow that of the GSE reasonably well.* ***The right graph:*** *Shows an excerpt of the spectroscopy done to measure the probabilities plotted in the left graph. Here we vary the gate $V_{tl,dot}$ while having $V_{tr,dot} = -1.5$ V fixed. Generally we found that the states in these measurements (using $V_{tl,dot}$) had less pronounced states than the spectroscopy of Fig. 5.3.*

5.3 Future experiments

Though we have seen signs of a non-Wigner-Dyson ensemble (the statistics of the level spacing does not follow that of the Gaussian orthogonal, unitary or symplectic ensembles) in the LoopQubit experiment, the design of the device is not optimized for an Andreev billiard experiment. However, we do see that we are able to resolve level statistics as we probe the DOS of the billiard. Especially the constricted QPC are somewhat detrimental to the transfer of superconductivity into the billiard. In this geometry normal scattering dominates the picture. Also, the size of the billiard leaves something to be desired. We will discuss these shortcomings in this section.

In future experiments we need to think about the energies which are relevant in the subject of Andreev Billiards [70].

- **Superconducting gap:** defined in Sec. 1.1.1, the gap Δ sets the upper energy scale. Within the energy window $E < \Delta$, we can for a large barrier guarantee that conducting modes are particle-hole symmetric, following Fig. 1.6, conductance in this window is dominated by AR.

- **The mean level spacing of the cavity:** The isolated cavity (in this case a mesoscopic quantum dot), has eigenenergies associated to the propagating modes that are stable within. From the number of modes in the cavity M (with energies $\{\epsilon_m\}$) the mean level spacing $\delta \simeq 2\pi/M$ [70]. This sets our minimum energy scale to resolve[3]

- **The ergodic energy:** The ergodic energy, E_{erg}, is commensurate to the ergodic time, $\tau_{\text{erg}} = A^{1/2}/v_F$, is the time scale after which the electrons have explored the phase space of the isolated cavity. It is defined by the area of the cavity, A, and the fermi velocity, v_F. It is an important time scale as for energies $E > \hbar/\tau_{\text{erg}}$, RMT for isolated billiards breaks down [70], as non-chaotic trajectories play a vital role in the dynamics of the problem (Fig. 5.6).

- **Thouless energy:** The Thouless energy E_T is the commensurate energy to that of dwell time $\tau_{\text{dwell}} = h/E_T$, which is the time between Andreev reflections

[3]We also have to consider that at finite temperature to resolve levels the level spacing should be less than the thermal broadening

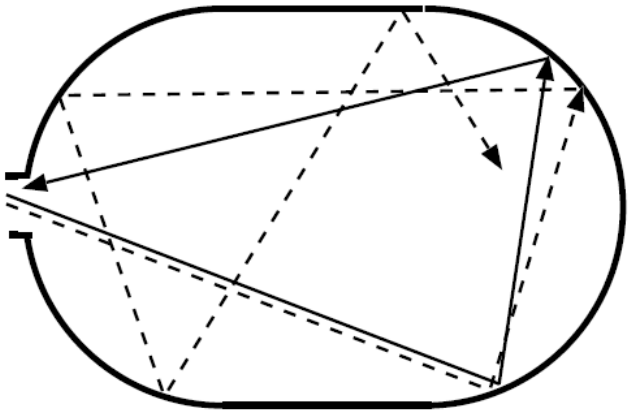

Figure 5.6: *As two electrons enter the billiard with a small microscopic separation, their trajectory at a short time scale might be indistinguishable. After τ_E the separation becomes macroscopic. Only at this point can we discern that the system is truly chaotic. Here $\tau_E = \alpha^{-1} \ln(L^*/\lambda_F)$, the chaos exponent α, the Lyapunov exponent, defines the rate of divergence, λ_F is the fermi wavelength, and L^* is a geometric constant which depends on the cavity geometry. [70]*

(Sec. 1.2.2). For a QPC this energy is $E_T = N\delta\Gamma/2\pi$, where N is the number of modes in the QPC and Γ is the transmission factor of the QPC [70].

- **The Ehrenfest energy:** The Ehrenfest energy E_E is commensurate to the time scale, τ_E which depends logarithmically on $\hbar$, at which we begin to resolve the quantum level spacing [70] (Fig. 5.6).

Decreasing $\tau_E/\tau_{\text{dwell}}$ leads us into the RMT regime [70]. This is also seen readily from Fig. 5.6, where the Lyapunov exponent of the system means that $\tau_{\text{dwell}} \gg \alpha^{-1}$, so that infinitesimally close trajectories can be seen to diverge before they Andreev retroreflect on the SC.

For future measurements the naive fitting procedure done in Fig. 5.3 and Fig. 5.5, can most probably be optimized. As mentioned, it is based on the peak finder algorithm of [71] where we first remove the background using a Savitszky-Golay filter. Sometimes it picks up peaks, which actually are not there. For future designs of the experiment, we immediately have two things we can modify: the level spacing and the coupling / number of modes between billiard and SC(s). The size of the billiard will change the number of modes supported by the isolated billiard, and as such we can make the mean level spacing smaller. As this should be the smallest energy in a spectroscopy measurement, this could most likely be optimized.

When we employ a QPC the phase space of electrons and holes are not mixed chaotically within an energy $E_T \propto N\delta$ [72]. Our system which has QPCs into separate SCs has been theoretically examined in [72]. Here it was found that such a system follows a circular unitary ensemble (CUE), and that the level spacing should have distribution that of a Wigner-Poisson hybrid PDF (pink line in Fig. 5.4). However, this is not what we found. A reasonable explanation is that our QPCs are not properly formed: this can be seen from the fact that we do not see well resolved Coulomb diamonds in spectroscopy. Future experiments to confirm this could therefore probe the system in a less coupled regime. However, as previously mentioned to guarantee particle-hole symmetry, the states we examine should be below the SC gap, Δ, and as such we should not probe the system in a regime as that of Sec. 3.2.1. Furthermore, adding charging energy to the problem also complicates the picture. The energy associated with adding a hole differs from that of an electron and will therefore interfere with the PH symmetry. This generically breaks the charge conjugation symmetry and prohibits the 2e transfer associated with AR (1.2.2) [70].

Though there are many exciting phenomena yet to be explored, and though the device we have measured until now, is not suited for this type of measurement, we have already seen that spectroscopy of laterally defined Andreev billiards, can prove a key tool to observe the universality classes of hybrid mesoscopic systems, and gain confidence in this observation due to the large number of configurations, which can be achieved within an ensemble.

CHAPTER 6

Appendix

A Dictionary

The meaning of abbreviations used for the gates in the device.

Gate Abbreviation	Gate meaning
V_{FET}	The field effect transistor
V_{filter}	The filter gate, which drives the SC backbone trivial
$V_{r(l),pg}$	The split QD plunger gates
V_{pgs}	QD plunger gates are symmetrically tuned
$V_{tl(r),w,tunnel}$	Top part of the wire tunnel barrier gate, also confines wire
$V_{bl(r),w,tunnel}$	Bottom part of the wire tunnel barrier gate, also confines bottom end of wire
$V_{l(r),wire}$	The plunger gate of the wire, which controls the potential of the SC wire
$V_{l(r),wire-end}$	The end gate of the wire, which drives the SC wire tip trivial
$V_{l(r),tunnel}$	Left and right normal lead / sensor dot tunnel gates.
$V_{l(r),sens}$	Confines the sensor dot and controls the coupling to normal lead
$V_{s,pg}$	Plunger gate of the sensor dot
$V_{[X]-comp}$	Gate [X] is compensated with other gates

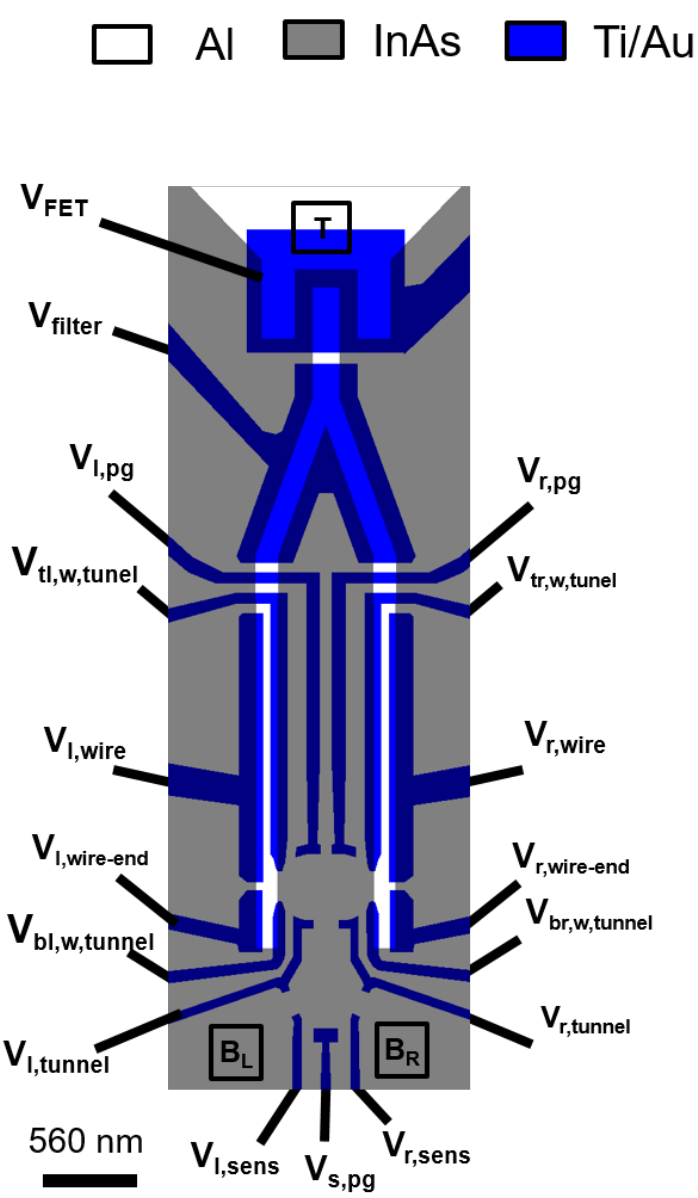

B Gate Voltages of Measurements

In this appendix we show what the compensation factor and all gate voltages of the gates are set to for each of the measurements.

Fig. 1.9a	Fig. 1.9b	Fig. 3.3a	Fig. 3.3b
$V_{\mathrm{bl,w,tunnel}} = -1.2$ V $V_{\mathrm{br,w,tunnel}} = -1.2$ V $V_{\mathrm{filter}} = -3$ V $V_{\mathrm{l,w,end}} = -1$ V $V_{\mathrm{lwire}} = -1$ V $V_{\mathrm{r,w,end}} = -2$ V $V_{\mathrm{rwire}} = -2$ V $V_{\mathrm{tl,w,tunnel}} = -1.5$ V $V_{\mathrm{tr,w,tunnel}} = -1.8$ V $B_{\perp} = 0$ $V_{\mathrm{r,l,tunnels}} = -630$ mV	$V_{\mathrm{bl,w,tunnel}} = -1.2$ V $V_{\mathrm{br,w,tunnel}} = -1.2$ V $V_{\mathrm{filter}} = -3$ V $V_{\mathrm{l,pg}} = -1$ V $V_{\mathrm{l,w,end}} = -1$ V $V_{\mathrm{lwire}} = -1$ V $V_{\mathrm{r,pg}} = -1$ V $V_{\mathrm{r,w,end}} = -2$ V $V_{\mathrm{rwire}} = -2$ V $V_{\mathrm{tl,w,tunnel}} = -1.5$ V $V_{\mathrm{tr,w,tunnel}} = -1.8$ V $B_{\mathrm{perp}} = 300$ mT $V_{\mathrm{r,l,tunnels}} = -630$ mV	$V_{\mathrm{filter}} = -3$ V $V_{\mathrm{l,pg}} = -1.03$ V $V_{\mathrm{l,w,end}} = -1$ V $V_{\mathrm{lwire}} = -1$ V $V_{\mathrm{r,pg}} = -1.03$ V $V_{\mathrm{r,w,end}} = -2$ V $V_{\mathrm{rwire}} = -2$ V $V_{\mathrm{tl,w,tunnel}} = -1.3$ V $V_{\mathrm{tr,w,tunnel}} = -1.8$ V	$V_{\mathrm{filter}} = -3$ V $V_{\mathrm{lwire}} = -1$ V $V_{\mathrm{rwire}} = -2.6$ V $B_{\mathrm{perp}} = -300$ mT $B_{\perp} = 0$ $V_{\mathrm{tl,w,tunnels}} = -2$ V $V_{\mathrm{w,ends}} = -3$ V $V_{\mathrm{pgs}} = -1$ V $V_{\mathrm{r,l,tunnels}} = -370$ mV
Fig. 3.4a	**Fig. 3.4b**	**Fig. 3.5**	**Fig. 3.6**
$V_{\mathrm{bl,w,tunnel}} = -239$ mV $V_{\mathrm{br,w,tunnel}} = -350$ mV $V_{\mathrm{filter}} = -3$ V $V_{\mathrm{l,w,end}} = -3.75$ V $V_{\mathrm{lwire}} = -2.5$ V $V_{\mathrm{r,w,end}} = -3$ V $V_{\mathrm{rwire}} = -4$ V $V_{\mathrm{tl,w,tunnel}} = -3$ V $V_{\mathrm{tr,w,tunnel}} = -3.75$ V $V_{\mathrm{pgs}} = -1$ V $V_{\mathrm{r,l,tunnels}} = -300$ mV	$V_{\mathrm{bl,w,tunnel}} = -239$ mV $V_{\mathrm{br,w,tunnel}} = -350$ mV $V_{\mathrm{filter}} = -3$ V $V_{\mathrm{l,w,end}} = -3.75$ V $V_{\mathrm{lwire}} = -2.5$ V $V_{\mathrm{r,w,end}} = -3$ V $V_{\mathrm{rwire}} = -4$ V $V_{\mathrm{tl,w,tunnel}} = -3$ V $V_{\mathrm{tr,w,tunnel}} = -3.75$ V $B_{\mathrm{perp}} = -2$ mT $V_{\mathrm{pgs}} = -1$ V $V_{\mathrm{r,l,tunnels}} = -300$ mV	$V_{\mathrm{bl,w,tunnel}} = -750$ mV $V_{\mathrm{filter}} = -3$ V $V_{\mathrm{l,w,end}} = -3.75$ V $V_{\mathrm{lwire}} = -2.5$ V $V_{\mathrm{r,w,end}} = -3$ V $V_{\mathrm{rwire}} = -3.15$ V $V_{\mathrm{tl,w,tunnel}} = -3$ V $V_{\mathrm{tr,w,tunnel}} = -3.5$ V $V_{\mathrm{pgs}} = -1.03$ V	$V_{\mathrm{bl,w,tunnel}} = -750$ mV $V_{\mathrm{br,w,tunnel}} = -485$ mV $V_{\mathrm{filter}} = -3$ V $V_{\mathrm{l,w,end}} = -3.75$ V $V_{\mathrm{lwire}} = -2.5$ V $V_{\mathrm{r,w,end}} = -3$ V $V_{\mathrm{rwire}} = -4$ V $V_{\mathrm{tl,w,tunnel}} = -3$ V $V_{\mathrm{tr,w,tunnel}} = -3.75$ V $B_{\mathrm{perp}} = -11$ mT $B_{\parallel} = 1$ T $V_{\mathrm{pgs}} = -1$ V
Fig. 3.8a	**Fig. 3.8b**	**Fig. 3.10**	**Fig. 3.11**
$V_{\mathrm{bl,w,tunnel}} = -1.2$ V $V_{\mathrm{br,w,tunnel}} = -1.2$ V $V_{\mathrm{filter}} = -3$ V $V_{\mathrm{l,pg}} = -1$ V $V_{\mathrm{l,w,end}} = -1$ V $V_{\mathrm{lwire}} = -1$ V $V_{\mathrm{r,pg}} = -1$ V $V_{\mathrm{r,w,end}} = -2$ V $V_{\mathrm{rwire}} = -2$ V $V_{\mathrm{tl,w,tunnel}} = -1.5$ V $V_{\mathrm{tr,w,tunnel}} = -1.8$ V $V_{\mathrm{r,l,tunnels}} = -630$ mV	$V_{\mathrm{bl,w,tunnel}} = -1.2$ V $V_{\mathrm{br,w,tunnel}} = -1.2$ V $V_{\mathrm{filter}} = -3$ V $V_{\mathrm{l,pg}} = -1$ V $V_{\mathrm{l,w,end}} = -1$ V $V_{\mathrm{lwire}} = -1$ V $V_{\mathrm{r,pg}} = -1$ V $V_{\mathrm{r,w,end}} = -2$ V $V_{\mathrm{rwire}} = -2$ V $V_{\mathrm{tl,w,tunnel}} = -1.5$ V $V_{\mathrm{tr,w,tunnel}} = -1.8$ V $B_{\mathrm{perp}} = 60$ mT $V_{\mathrm{r,l,tunnels}} = -630$ mV	$V_{\mathrm{bl,w,tunnel}} = -200$ mV $V_{\mathrm{br,w,tunnel}} = -200$ mV $V_{\mathrm{filter}} = -3$ V $V_{\mathrm{l,w,end}} = -1$ V $V_{\mathrm{lwire}} = -1$ V $V_{\mathrm{r,w,end}} = -2$ V $V_{\mathrm{rwire}} = -2$ V $V_{\mathrm{tl,w,tunnel}} = -1.3$ V $V_{\mathrm{tr,w,tunnel}} = -1.8$ V $V_{\mathrm{r,l,tunnels}} = -450$ mV	$V_{\mathrm{bl,w,tunnel}} = -275$ mV $V_{\mathrm{br,w,tunnel}} = -410$ mV $V_{\mathrm{filter}} = -3$ V $V_{\mathrm{lwire}} = -1$ V $V_{\mathrm{rwire}} = -2.6$ V $B_{\mathrm{perp}} = -10$ mT $B_{\perp} = -1.25$ mT $V_{\mathrm{r,l,tunnels}} = -376$ mV $V_{\mathrm{t,w,tunnels}} = -2$ V $V_{\mathrm{w,ends}} = -3$ V

Fig. 3.14a	Fig. 3.14b	Fig. 3.15a	Fig. 3.15b
$V_{\mathrm{bl,w,tunnel}} = -570$ mV $V_{\mathrm{br,w,tunnel}} = -950$ mV $V_{\mathrm{filter}} = -3$ V $V_{\mathrm{l,w,end}} = -1$ V $V_{\mathrm{lwire}} = -1$ V $V_{\mathrm{r,w,end}} = -2$ V $V_{\mathrm{rwire}} = -2$ V $V_{\mathrm{tl,w,tunnel}} = -1$ V $V_{\mathrm{tr,w,tunnel}} = -2.8$ V $B_{\perp} = 1.48$ mT $V_{\mathrm{r,l,tunnels}} = -440$ mV	$V_{\mathrm{bl,w,tunnel}} = -750$ mV $V_{\mathrm{br,w,tunnel}} = -388$ mV $V_{\mathrm{filter}} = -3$ V $V_{\mathrm{l,w,end}} = -3.75$ V $V_{\mathrm{lwire}} = -2.5$ V $V_{\mathrm{r,w,end}} = -3$ V $V_{\mathrm{rwire}} = -3.15$ V $V_{\mathrm{tl,w,tunnel}} = -3$ V $V_{\mathrm{tr,w,tunnel}} = -3.5$ V $B_{\perp} = -200$ μT $V_{\mathrm{r,l,tunnels}} = -310$ mV	$V_{\mathrm{bl,w,tunnel}} = -750$ mV $V_{\mathrm{br,w,tunnel}} = -391$ mV $V_{\mathrm{filter}} = -3$ V $V_{\mathrm{l,w,end}} = -3.75$ V $V_{\mathrm{lwire}} = -2.5$ V $V_{\mathrm{r,w,end}} = -3$ V $V_{\mathrm{rwire}} = -3.15$ V $V_{\mathrm{tl,w,tunnel}} = -3$ V $V_{\mathrm{tr,w,tunnel}} = -3.5$ V $B_{\perp} = 1.25$ mT $V_{\mathrm{r,l,tunnels}} = -310$ mV	$V_{\mathrm{bl,w,tunnel}} = -750$ mV $V_{\mathrm{br,w,tunnel}} = -391$ mV $V_{\mathrm{filter}} = -3$ V $V_{\mathrm{l,w,end}} = -3.75$ V $V_{\mathrm{lwire}} = -2.5$ V $V_{\mathrm{r,w,end}} = -3$ V $V_{\mathrm{rwire}} = -3.15$ V $V_{\mathrm{tl,w,tunnel}} = -3$ V $V_{\mathrm{tr,w,tunnel}} = -3.5$ V $V_{\mathrm{r,l,tunnels}} = -310$ mV
Fig. 3.16a	**Fig. 3.16b**	**Fig. 3.17a**	**Fig. 3.17b**
$V_{\mathrm{bl,w,tunnel}} = -269$ mV $V_{\mathrm{br,w,tunnel}} = -775$ mV $V_{\mathrm{filter}} = -3$ V $V_{\mathrm{l,w,end}} = -3.75$ V $V_{\mathrm{lwire}} = -1.835$ V $V_{\mathrm{r,w,end}} = -3$ V $V_{\mathrm{rwire}} = -2.955$ V $V_{\mathrm{tl,w,tunnel}} = -3$ V $V_{\mathrm{tr,w,tunnel}} = -3.5$ V $V_{\mathrm{AC}} = 3$ μV $f_{\mathrm{AC}} = 179$ Hz $t_{\mathrm{int}} = 100$ ms $V_{\mathrm{pgs}} = -1.155$ V $V_{\mathrm{r,l,tunnels}} = -310$ mV	$V_{\mathrm{bl,w,tunnel}} = -750$ mV $V_{\mathrm{br,w,tunnel}} = -411$ mV $V_{\mathrm{filter}} = -3$ V $V_{\mathrm{l,w,end}} = -3.75$ V $V_{\mathrm{lwire}} = -2.5$ V $V_{\mathrm{r,w,end}} = -3$ V $V_{\mathrm{rwire}} = -3.096$ V $V_{\mathrm{tl,w,tunnel}} = -3$ V $V_{\mathrm{tr,w,tunnel}} = -3.5$ V $V_{\mathrm{r,l,tunnels}} = -310$ mV	$V_{\mathrm{bl,w,tunnel}} = -270$ mV $V_{\mathrm{br,w,tunnel}} = -411$ mV $V_{\mathrm{filter}} = -3$ V $V_{\mathrm{l,w,end}} = -3.75$ V $V_{\mathrm{lwire}} = -1.837$ V $V_{\mathrm{r,w,end}} = -3$ V $V_{\mathrm{tl,w,tunnel}} = -3$ V $V_{\mathrm{tr,w,tunnel}} = -3.5$ V $B_{\mathrm{perp}} = -7$ mT $B_{\parallel} = 620$ mT $V_{\mathrm{AC}} = 15$ μV $f_{\mathrm{AC}} = 31$ Hz $t_{\mathrm{int}} = 100$ ms $V_{\mathrm{r,l,tunnels}} = -353$ mV	$V_{\mathrm{bl,w,tunnel}} = -270$ mV $V_{\mathrm{br,w,tunnel}} = -413$ mV $V_{\mathrm{filter}} = -3$ V $V_{\mathrm{l,w,end}} = -3.75$ V $V_{\mathrm{lwire}} = -1.837$ V $V_{\mathrm{r,w,end}} = -3$ V $V_{\mathrm{rwire}} = -3.128$ V $V_{\mathrm{tl,w,tunnel}} = -3$ V $V_{\mathrm{tr,w,tunnel}} = -3.5$ V $B_{\mathrm{perp}} = -7$ mT $B_{\parallel} = 620$ mT $V_{\mathrm{AC}} = 3$ μV $f_{\mathrm{AC}} = 179$ Hz $t_{\mathrm{int}} = 100$ ms $V_{\mathrm{pgs}} = -1.055$ V $V_{\mathrm{r,l,tunnels}} = -353$ mV
Fig. 3.18a	**Fig. 3.18b**	**Fig. 3.19**	**Fig. 3.20 & Fig. 3.21**
$V_{\mathrm{bl,w,tunnel}} = -275$ mV $V_{\mathrm{br,w,tunnel}} = -775$ mV $V_{\mathrm{filter}} = -3$ V $V_{\mathrm{l,w,end}} = -3.75$ V $V_{\mathrm{lwire}} = -2.47$ V $V_{\mathrm{r,w,end}} = -3$ V $V_{\mathrm{rwire}} = -2.955$ V $V_{\mathrm{tl,w,tunnel}} = -3$ V $V_{\mathrm{tr,w,tunnel}} = -3.5$ V $B_{\mathrm{perp}} = -7$ mT $B_{\parallel} = 620$ mT $B_{\perp} = 1.25$ mT $V_{\mathrm{pgs}} = -1.1$ V $V_{\mathrm{r,l,tunnels}} = -310$ mV	$V_{\mathrm{bl,w,tunnel}} = -750$ mV $V_{\mathrm{br,w,tunnel}} = -415$ mV $V_{\mathrm{filter}} = -3$ V $V_{\mathrm{l,w,end}} = -3.75$ V $V_{\mathrm{lwire}} = -2.5$ V $V_{\mathrm{r,w,end}} = -3$ V $V_{\mathrm{rwire}} = -3.073$ V $V_{\mathrm{tl,w,tunnel}} = -3$ V $V_{\mathrm{tr,w,tunnel}} = -3.5$ V $B_{\mathrm{perp}} = -5$ mT $B_{\parallel} = 450$ mT $V_{\mathrm{r,l,tunnels}} = -301$ mV	$V_{\mathrm{bl,w,tunnel}} = -275$ mV $V_{\mathrm{br,w,tunnel}} = -411$ mV $V_{\mathrm{filter}} = -3$ V $V_{\mathrm{l,w,end}} = -3.75$ V $V_{\mathrm{r,w,end}} = -3$ V $V_{\mathrm{tl,w,tunnel}} = -2.61$ V $V_{\mathrm{tr,w,tunnel}} = -3.5$ V $B_{\mathrm{perp}} = -7$ mT $B_{\parallel} = 680$ mT $V_{\mathrm{AC}} = 15$ μV $f_{\mathrm{AC}} = 31$ Hz $t_{\mathrm{int}} = 100$ ms $V_{\mathrm{pgs}} = -1.167$ V $V_{\mathrm{r,l,tunnels}} = -347$ mV	$V_{\mathrm{bl,w,tunnel}} = -267$ mV $V_{\mathrm{br,w,tunnel}} = -412$ mV $V_{\mathrm{filter}} = -3$ V $V_{\mathrm{l,w,end}} = -3.75$ V $V_{\mathrm{lwire}} = -1.469$ V $V_{\mathrm{r,w,end}} = -3$ V $V_{\mathrm{rwire}} = -2.945$ V $V_{\mathrm{tl,w,tunnel}} = -2.604$ V $V_{\mathrm{tr,w,tunnel}} = -3.5$ V $B_{\mathrm{perp}} = -7$ mT $B_{\parallel} = 680$ mT $V_{\mathrm{AC}} = 3$ μV $f_{\mathrm{AC}} = 167$ Hz $t_{\mathrm{int}} = 100$ ms $V_{\mathrm{pgs}} = -1.111$ V $V_{\mathrm{r,l,tunnels}} = -347$ mV

Fig. 3.22	Fig. 5.3 and Fig. 5.4	Fig. 5.5	
$V_{\mathrm{bl,w,tunnel}} = -267$ mV $V_{\mathrm{br,w,tunnel}} = -412$ mV $V_{\mathrm{filter}} = -3$ V $V_{\mathrm{l,w,end}} = -3.75$ V $V_{\mathrm{lwire}} = -1.49$ V $V_{\mathrm{r,w,end}} = -3$ V $V_{\mathrm{rwire}} = -2.916$ V $V_{\mathrm{tl,w,tunnel}} = -2.604$ V $V_{\mathrm{tr,w,tunnel}} = -3.5$ V $B_{\mathrm{perp}} = -7$ mT $B_{\parallel} = 680$ mT $B_{\perp} = 0$ $V_{\mathrm{AC}} = 3\ \mu$V $f_{\mathrm{AC}} = 167$ Hz $t_{\mathrm{int}} = 100$ ms $V_{\mathrm{pgs}} = -1.11$ V $V_{\mathrm{r,l,tunnels}} = -347$ mV	$V_{\mathrm{filter}} = -4$ V $V_{\mathrm{ltunnel}} = -1$ V $V_{\mathrm{rtunnel}} = -930$ mV $V_{\mathrm{split}} = -1.85$ V $V_{\mathrm{bot,dots}} = -2.76$ V $V_{\mathrm{r,l,wires}} = -1.5$ V	$V_{\mathrm{filter}} = -4$ V $V_{\mathrm{ltunnel}} = -1$ V $V_{\mathrm{rtunnel}} = -930$ mV $V_{\mathrm{split}} = -1.85$ V $V_{\mathrm{bot,dots}} = -2.724$ V $V_{\mathrm{r,l,wires}} = -1.5$ V	

Compensations

- Fig. 3.17b: $V_{pgs}(V_{r,wire}) = -0.2121 \cdot (V_{r,wire} + 3.0932V) - 1.129V$
- Fig. 3.18a: $V_{l,wire}(V_{pgs}) = -0.28(V_{pgs} + 1.100V) - 2.470V$ and $V_{bl,w,tunnel}(V_{pgs}) = -0.00266(V_{pgs} + 1.100V) - 0.2749V$
- Fig. 3.20 $V_{\mathrm{l,wire}}(V_{\mathrm{pgs}})$ = -0.14(V_{pgs} + 1.100V) - 1.47033V and $V_{\mathrm{r,wire}}(V_{\mathrm{pgs}})$ = -0.37(V_{pgs} + 1.100V) - 2.94883V

APPENDIX A

Bibliography

[1] P Benioff. The computer as a physical system: A microscopic quantum mechanical hamiltonian model of computers as represented by turing machines. J Stat Phys, 22:563–591, May 1980.

[2] W. Wootters and W. Zurek. A single quantum cannot be cloned. Nature, 299:802–803, Oct 1982. doi: 10.1038/299802a0. URL https://doi.org/10.1038/299802a0.

[3] D. Dieks. Communication by epr devices. Physics Letters A, 92(6):271–272, 1982. ISSN 0375-9601. doi: https://doi.org/10.1016/0375-9601(82)90084-6. URL https://www.sciencedirect.com/science/article/pii/0375960182900846.

[4] Torsten Karzig, Christina Knapp, Roman M. Lutchyn, Parsa Bonderson, Matthew B. Hastings, Chetan Nayak, Jason Alicea, Karsten Flensberg, Stephan Plugge, Yuval Oreg, and et al. Scalable designs for quasiparticle-poisoning-protected topological quantum computation with majorana zero modes. Physical Review B, 95(23), Jun 2017. ISSN 2469-9969. doi: 10.1103/physrevb.95.235305. URL http://dx.doi.org/10.1103/PhysRevB.95.235305.

[5] H. K. Onnes. Further experiments with liquid helium. c. on the change of electric resistance of pure metals at very low temperatures etc. iv. the resistance of pure mercury at helium temperatures. Proc. K. Ned. Akad. Wet, 13:1274–1276, 1911.

[6] F. London and H. London. The electromagnetic equations of the supraconductor. Proc. R. Soc. Lond. A, 159:71–88, 1935.

[7] On the theory of superconductivity. In Collected Papers of L.D. Landau, pages 546–568. Pergamon, 1965. ISBN 978-0-08-010586-4. doi: https://doi.org/10.1016/B978-0-08-010586-4.50078-X. URL https://www.sciencedirect.com/science/article/pii/B978008010586450078X.

[8] LP Gor'kov. Mikroskopicheskoe proiskhozhdenie uravnenii ginzburg-landau v teorii sverkhprovodimosti. Zh. Eksp. Teor. Fiz, 36:1918, 1959.

[9] Leon N. Cooper. Bound electron pairs in a degenerate fermi gas. Phys. Rev., 104:1189–1190, Nov 1956. doi: 10.1103/PhysRev.104.1189. URL https://link.aps.org/doi/10.1103/

PhysRev.104.1189.

[10] J. Bardeen, L. N. Cooper, and J. R. Schrieffer. Microscopic theory of superconductivity. Phys. Rev., 106:162–164, Apr 1957. doi: 10.1103/PhysRev.106.162. URL https://link.aps.org/doi/10.1103/PhysRev.106.162.

[11] J. Bardeen, L. N. Cooper, and J. R. Schrieffer. Theory of superconductivity. Phys. Rev., 108: 1175–1204, Dec 1957. doi: 10.1103/PhysRev.108.1175. URL https://link.aps.org/doi/10.1103/PhysRev.108.1175.

[12] Alexander Altland and Ben Simons. Condensed Matter Field Theory. Cambridge, 2 edition, 2006. ISBN 9780521769754.

[13] Liang Fu and C. L. Kane. Superconducting proximity effect and majorana fermions at the surface of a topological insulator. Phys. Rev. Lett., 100:096407, Mar 2008. doi: 10.1103/PhysRevLett.100.096407. URL https://link.aps.org/doi/10.1103/PhysRevLett.100.096407.

[14] S. Li et al J. Wang, K. Ran. Evidence for singular-phonon-induced nematic superconductivity in a topological superconductor candidate sr0.1bi2se3. Nat Commun, 10, Dec 2019. doi: 10.1038/s41467-019-10942-2.

[15] V.P. Mineev, K. Samokhin, L.D. Landau, and L.D. Landau. Introduction to Unconventional Superconductivity. Taylor and Francis, 1999. ISBN 9789056992095. URL https://books.google.dk/books?id=2BXYWT8m068C.

[16] A Yu Kitaev. Unpaired majorana fermions in quantum wires. Physics-Uspekhi, 44(10S): 131–136, oct 2001. doi: 10.1070/1063-7869/44/10s/s29. URL https://doi.org/10.1070/1063-7869/44/10s/s29.

[17] Alexei Kitaev and Chris Laumann. Topological phases and quantum computation, 2009. Lectures given by Alexei Kitaev at the 2008 Les Houches Summer School "Exact methods in low-dimensional physics and quantum computing".

[18] S. Simon. Topological quantum: Lecture notes, September 2016.

[19] Chetan Nayak, Steven H. Simon, Ady Stern, Michael Freedman, and Sankar Das Sarma. Non-abelian anyons and topological quantum computation. Rev. Mod. Phys., 80:1083–1159, Sep 2008. doi: 10.1103/RevModPhys.80.1083. URL https://link.aps.org/doi/10.1103/RevModPhys.80.1083.

[20] Parsa Bonderson, Michael Freedman, and Chetan Nayak. Measurement-only topological quantum computation. Phys. Rev. Lett., 101:010501, Jun 2008. doi: 10.1103/PhysRevLett.101.010501. URL https://link.aps.org/doi/10.1103/PhysRevLett.101.010501.

[21] Roman M. Lutchyn, Jay D. Sau, and S. Das Sarma. Majorana fermions and a topological phase transition in semiconductor-superconductor heterostructures. Physical Review Letters, 105(7), Aug 2010. ISSN 1079-7114. doi: 10.1103/physrevlett.105.077001. URL http://dx.doi.org/10.1103/PhysRevLett.105.077001.

[22] Yuval Oreg, Gil Refael, and Felix von Oppen. Helical liquids and majorana bound states in quantum wires. Phys. Rev. Lett., 105:177002, Oct 2010. doi: 10.1103/PhysRevLett.105.177002.

URL https://link.aps.org/doi/10.1103/PhysRevLett.105.177002.

[23] Thomas Ihn. Semiconductor Nanostructures - Quantum States and Electronic Transport. Oxford University Press, 2 edition, 2010. ISBN 9780199534425.

[24] A. Manchon, H. C. Koo, J. Nitta, S. M. Frolov, and R. A. Duine. New perspectives for rashba spin–orbit coupling. Nature Materials, 14(9):871–882, Aug 2015. ISSN 1476-4660. doi: 10.1038/nmat4360. URL http://dx.doi.org/10.1038/nmat4360.

[25] W. Meissner, H. Franz, and H. Westerhoff. Messungen mit hilfe von flüssigem helium. xv widerstand von barium, indium, thallium, graphit und titan in tiefen temperaturen. Annalen der Physik, 405:555–563, 1932.

[26] G. E. Blonder, M. Tinkham, and T. M. Klapwijk. Transition from metallic to tunneling regimes in superconducting microconstrictions: Excess current, charge imbalance, and supercurrent conversion. Phys. Rev. B, 25:4515–4532, Apr 1982. doi: 10.1103/PhysRevB.25.4515. URL https://link.aps.org/doi/10.1103/PhysRevB.25.4515.

[27] T. Klapwijk. Proximity effect from an andreev perspective. Journal of Superconductivity, 17: 593–611, 2004.

[28] Hans Lüth. Collective Phenomena at Interfaces: Superconductivity and Ferromagnetism, pages 449–526. Springer International Publishing, Cham, 2015. ISBN 978-3-319-10756-1. doi: 10.1007/978-3-319-10756-1_9. URL https://doi.org/10.1007/978-3-319-10756-1_9.

[29] C. W. J. Beenakker. Specular andreev reflection in graphene. Physical Review Letters, 97(6), Aug 2006. ISSN 1079-7114. doi: 10.1103/physrevlett.97.067007. URL http://dx.doi.org/10.1103/PhysRevLett.97.067007.

[30] Chunxu Bai and Yanling Yang. Specular andreev reflection in graphene-based superconducting junction with substate-induced spin orbit interaction. Physics Letters A, 380(37):2947–2952, 2016. ISSN 0375-9601. doi: https://doi.org/10.1016/j.physleta.2016.07.004. URL https://www.sciencedirect.com/science/article/pii/S0375960116303991.

[31] Thomas Schäpers. Superconductor/Semiconductor Junctions. Springer, Berlin, Heidelberg, 1 edition, 2001. ISBN 978-3-540-42220-4.

[32] Elsa Prada, Pablo San-Jose, Michiel W. A. de Moor, Attila Geresdi, Eduardo J. H. Lee, Jelena Klinovaja, Daniel Loss, Jesper Nygård, Ramón Aguado, and Leo P. Kouwenhoven. From andreev to majorana bound states in hybrid superconductor–semiconductor nanowires. Nature Reviews Physics, 2(10):575–594, Sep 2020. ISSN 2522-5820. doi: 10.1038/s42254-020-0228-y. URL http://dx.doi.org/10.1038/s42254-020-0228-y.

[33] Sankar Das Sarma and Haining Pan. Disorder-induced zero-bias peaks in majorana nanowires. Physical Review B, 103(19), May 2021. ISSN 2469-9969. doi: 10.1103/physrevb.103.195158. URL http://dx.doi.org/10.1103/PhysRevB.103.195158.

[34] İ. Adagideli, M. Wimmer, and A. Teker. Effects of electron scattering on the topological properties of nanowires: Majorana fermions from disorder and superlattices. Physical Review B, 89(14), Apr 2014. ISSN 1550-235X. doi: 10.1103/physrevb.89.144506. URL http:

//dx.doi.org/10.1103/PhysRevB.89.144506.

[35] David Aasen, Michael Hell, Ryan V. Mishmash, Andrew Higginbotham, Jeroen Danon, Martin Leijnse, Thomas S. Jespersen, Joshua A. Folk, Charles M. Marcus, Karsten Flensberg, and et al. Milestones toward majorana-based quantum computing. Physical Review X, 6(3). ISSN 2160-3308. doi: 10.1103/physrevx.6.031016. URL http://dx.doi.org/10.1103/PhysRevX.6.031016.

[36] Liang Fu. Electron teleportation via majorana bound states in a mesoscopic superconductor. Physical Review Letters, 104(5), Feb 2010. ISSN 1079-7114. doi: 10.1103/physrevlett.104.056402. URL http://dx.doi.org/10.1103/PhysRevLett.104.056402.

[37] Adriaan Vuik, Bas Nijholt, Anton Akhmerov, and Michael Wimmer. Reproducing topological properties with quasi-majorana states. SciPost Physics, 7(5), Nov 2019. ISSN 2542-4653. doi: 10.21468/scipostphys.7.5.061. URL http://dx.doi.org/10.21468/SciPostPhys.7.5.061.

[38] A. M. Whiticar. Flux Dependence of Topological Superconductivity in Two-Dimensional Heterostructures. PhD thesis, University of Copenhagen, 1 2020.

[39] Jie Shen, Sebastian Heedt, Francesco Borsoi, Bernard van Heck, Sasa Gazibegovic, Roy L. M. Op het Veld, Diana Car, John A. Logan, Mihir Pendharkar, Senja J. J. Ramakers, and et al. Parity transitions in the superconducting ground state of hybrid insb–al coulomb islands. Nature Communications, 9(1), Nov 2018. ISSN 2041-1723. doi: 10.1038/s41467-018-07279-7. URL http://dx.doi.org/10.1038/s41467-018-07279-7.

[40] Karsten Flensberg. Non-abelian operations on majorana fermions via single-charge control. Physical Review Letters, 106(9), Mar 2011. ISSN 1079-7114. doi: 10.1103/physrevlett.106.090503. URL http://dx.doi.org/10.1103/PhysRevLett.106.090503.

[41] Xanthe Grace Croot. The Environment and Interactions of Electrons in GaAs Quantum Dots. PhD thesis, University of Sydney, The address of the publisher, 7 2017.

[42] Stephan Plugge, Asbjørn Rasmussen, Reinhold Egger, and Karsten Flensberg. Majorana box qubits. New Journal of Physics, 19(1), Jan 2017. ISSN 1367-2630. doi: 10.1088/1367-2630/aa54e1. URL http://dx.doi.org/10.1088/1367-2630/aa54e1.

[43] M. T. Deng, S. Vaitiekenas, E. B. Hansen, J. Danon, M. Leijnse, K. Flensberg, J. Nygard, P. Krogstrup, and C. M. Marcus. Majorana bound state in a coupled quantum-dot hybrid-nanowire system. Science, 354(6319):1557–1562, Dec 2016. ISSN 1095-9203. doi: 10.1126/science.aaf3961. URL http://dx.doi.org/10.1126/science.aaf3961.

[44] H. J. Suominen, M. Kjaergaard, A. R. Hamilton, J. Shabani, C. J. Palmstrom, C. M. Marcus, and F. Nichele. Zero-energy modes from coalescing andreev states in a two-dimensional semiconductor-superconductor hybrid platform. Phys. Rev. Lett., 119:176805, Oct 2017. doi: 10.1103/PhysRevLett.119.176805. URL https://link.aps.org/doi/10.1103/PhysRevLett.119.176805.

[45] Stephen A. Campbell. Fabrication engineering at the micro- and nanoscale. Oxford series

in electrical engineering. Oxford University Press, New York, 4th ed. edition, 2013. ISBN 9780199861224.

[46] Wafer stack picture included with permission from Tyler Lindemann from the Manfra Group at Purdue University.

[47] S.W. Hieke, B. Breitbach, G. Dehm, and C. Scheu. Microstructural evolution and solid state dewetting of epitaxial al thin films on sapphire (al2o3). Acta Materialia, 133:356–366, 2017. ISSN 1359-6454. doi: https://doi.org/10.1016/j.actamat.2017.05.026. URL https://www.sciencedirect.com/science/article/pii/S1359645417304032.

[48] Lucas Casparis, Malcolm R. Connolly, Morten Kjaergaard, Natalie J. Pearson, Anders Kringhoj, Thorvald W. Larsen, Ferdinand Kuemmeth, Tiantian Wang, Candice Thomas, Sergei Gronin, and et al. Superconducting gatemon qubit based on a proximitized two-dimensional electron gas. Nature Nanotechnology, 13(10):915–919, Jul 2018. ISSN 1748-3395. doi: 10.1038/s41565-018-0207-y. URL http://dx.doi.org/10.1038/s41565-018-0207-y.

[49] Kaushini S. Wickramasinghe, William Mayer, Joseph Yuan, Tri Nguyen, Lucy Jiao, Vladimir Manucharyan, and Javad Shabani. Transport properties of near surface inas two-dimensional heterostructures. Applied Physics Letters, 113(26):262104, Dec 2018. ISSN 1077-3118. doi: 10.1063/1.5050413. URL http://dx.doi.org/10.1063/1.5050413.

[50] August E. G. Mikkelsen, Panagiotis Kotetes, Peter Krogstrup, and Karsten Flensberg. Hybridization at superconductor-semiconductor interfaces. Phys. Rev. X, 8:031040, Aug 2018. doi: 10.1103/PhysRevX.8.031040. URL https://link.aps.org/doi/10.1103/PhysRevX.8.031040.

[51] K. Oura, M. Katayama, A.V. Zotov, V.G. Lifshits, and A.A Saranin. Surface Science, chapter 8, pages 171–194213. Advanced Texts in Physics. Springer, Berlin, Heidelberg, 1 edition, 2003. Chapter: Atomic Structure of Clean Surfaces.

[52] Frank Pobell. Matter and Methods at Low Temperatures. Springer, Berlin, Heidelberg, 3 edition, 2007. ISBN 978-3-540-46356-6.

[53] About lock-in amplifiers. https://www.thinksrs.com/downloads/pdfs/applicationnotes/AboutLIAs.pdf. Accessed: 2021-10-16.

[54] Ivar Giaever. Energy gap in superconductors measured by electron tunneling. Phys. Rev. Lett., 5:147–148, Aug 1960. doi: 10.1103/PhysRevLett.5.147. URL https://link.aps.org/doi/10.1103/PhysRevLett.5.147.

[55] Christian Jünger, Andreas Baumgartner, Raphaëlle Delagrange, Denis Chevallier, Sebastian Lehmann, Malin Nilsson, Kimberly A. Dick, Claes Thelander, and Christian Schönenberger. Spectroscopy of the superconducting proximity effect in nanowires using integrated quantum dots. Communications Physics, 2(1), Jul 2019. ISSN 2399-3650. doi: 10.1038/s42005-019-0162-4. URL http://dx.doi.org/10.1038/s42005-019-0162-4.

[56] Silvano De Franceschi, Leo Kouwenhoven, and Christian et al Schönenberger. Hybrid superconductor–quantum dot devices. Nature Nanotechnology, 5:703–711, Sep 2010. doi:

10.1038/nnano.2010.173. URL https://doi.org/10.1038/nnano.2010.173.

[57] A. M. Whiticar, A. Fornieri, A. Banerjee, A. C. C. Drachmann, S. Gronin, G. C. Gardner, T. Lindemann, M. J. Manfra, and C. M. Marcus. Zeeman-driven parity transitions in an andreev quantum dot. Physical Review B, 103(24), Jun 2021. ISSN 2469-9969. doi: 10.1103/physrevb.103.245308. URL http://dx.doi.org/10.1103/PhysRevB.103.245308.

[58] Gediminas Kirsanskas, Moshe Goldstein, Karsten Flensberg, Leonid I. Glazman, and Jens Paaske. Yu-shiba-rusinov states in phase-biased superconductor–quantum dot–superconductor junctions. Phys. Rev. B, 92:235422, Dec 2015. doi: 10.1103/PhysRevB.92.235422. URL https://link.aps.org/doi/10.1103/PhysRevB.92.235422.

[59] P. W. Anderson. Localized magnetic states in metals. Phys. Rev., 124:41–53, Oct 1961. doi: 10.1103/PhysRev.124.41. URL https://link.aps.org/doi/10.1103/PhysRev.124.41.

[60] P.W. Anderson. Theory of dirty superconductors. Journal of Physics and Chemistry of Solids, 11 (1):26–30, 1959. ISSN 0022-3697. doi: https://doi.org/10.1016/0022-3697(59)90036-8. URL https://www.sciencedirect.com/science/article/pii/0022369759900368.

[61] Tobias Meng, Pascal Simon, and Serge Florens. Self-consistent description of andreev bound states in josephson quantum dot devices. Physical Review B, 79, 02 2009. doi: 10.1103/PhysRevB.79.224521.

[62] E. C. T. O'Farrell, A. C. C. Drachmann, M. Hell, A. Fornieri, A. M. Whiticar, E. B. Hansen, S. Gronin, G. C. Gardner, C. Thomas, M. J. Manfra, K. Flensberg, C. M. Marcus, and F. Nichele. Hybridization of subgap states in one-dimensional superconductor-semiconductor coulomb islands. Phys. Rev. Lett., 121:256803, Dec 2018. doi: 10.1103/PhysRevLett.121.256803. URL https://link.aps.org/doi/10.1103/PhysRevLett.121.256803.

[63] Elsa Prada, Ramon Aguado, and Pablo San-Jose. Measuring majorana nonlocality and spin structure with a quantum dot. Physical Review B, 96(8), Aug 2017. ISSN 2469-9969. doi: 10.1103/physrevb.96.085418. URL http://dx.doi.org/10.1103/PhysRevB.96.085418.

[64] Leo P. Kouwenhoven, Charles M. Marcus, Paul L. McEuen, Seigo Tarucha, Robert M. Westervelt, and Ned S. Wingreen. Electron Transport in Quantum Dots, pages 105–214. Springer Netherlands, Dordrecht, 1997. ISBN 978-94-015-8839-3. doi: 10.1007/978-94-015-8839-3_4. URL https://doi.org/10.1007/978-94-015-8839-3_4.

[65] W. Chang, V. E. Manucharyan, T. S. Jespersen, J. Nygard, and C. M. Marcus. Tunneling spectroscopy of quasiparticle bound states in a spinful josephson junction. Physical Review Letters, 110(21), May 2013. ISSN 1079-7114. doi: 10.1103/physrevlett.110.217005. URL http://dx.doi.org/10.1103/PhysRevLett.110.217005.

[66] John Wishart. The generalised product moment distribution in samples from a normal multivariate population. Biometrika, 20A(1/2):32–52, 1928. ISSN 00063444. URL http://www.jstor.org/stable/2331939.

[67] Eugene P. Wigner. Characteristic vectors of bordered matrices with infinite dimensions. Annals of Mathematics, 62(3):548–564, 1955. ISSN 0003486X. URL http://www.jstor.org/

stable/1970079.

[68] C. W. J. Beenakker. Random-matrix theory of quantum transport. Reviews of Modern Physics, 69(3):731–808, Jul 1997. ISSN 1539-0756. doi: 10.1103/revmodphys.69.731. URL http://dx.doi.org/10.1103/RevModPhys.69.731.

[69] C. W. J. Beenakker. Random-matrix theory of majorana fermions and topological superconductors. Rev. Mod. Phys., 87:1037–1066, Sep 2015. doi: 10.1103/RevModPhys.87.1037.

[70] C. W. J. Beenakker. Andreev billiards. Lecture Notes in Physics, page 131–174, Mar 2005. ISSN 1616-6361. doi: 10.1007/11358817_4. URL http://dx.doi.org/10.1007/11358817_4.

[71] Nathanael Yoder. peakfinder(x0, sel, thresh, extrema, includeendpoints, interpolate) (https://www.mathworks.com/matlabcentral/fileexchange/25500-peakfinder-x0-sel-thresh-extrema-includeendpoints-interpolate). MATLAB Central File Exchange, 2021. Retrieved November 1, 2021.

[72] C. W. J. Beenakker, J. M. Edge, J. P. Dahlhaus, D. I. Pikulin, Shuo Mi, and M. Wimmer. Wigner-poisson statistics of topological transitions in a josephson junction. Physical Review Letters, 111(3), Jul 2013. ISSN 1079-7114. doi: 10.1103/physrevlett.111.037001. URL http://dx.doi.org/10.1103/PhysRevLett.111.037001.

[73] Alexander Altland and Martin R. Zirnbauer. Nonstandard symmetry classes in mesoscopic normal-superconducting hybrid structures. Physical Review B, 55(2):1142–1161, Jan 1997. ISSN 1095-3795. doi: 10.1103/physrevb.55.1142. URL http://dx.doi.org/10.1103/PhysRevB.55.1142.

[74] A.Yu. Kitaev. Fault-tolerant quantum computation by anyons. Annals of Physics, 303(1):2–30, Jan 2003. ISSN 0003-4916. doi: 10.1016/s0003-4916(02)00018-0. URL http://dx.doi.org/10.1016/S0003-4916(02)00018-0.